Insulation Resistance Monitoring for HVDC systems in automotive applications

Bachelor thesis in electrical engineering

Asbjørn Rohde, Robert Kandel

DEPARTMENT OF ELECTRICAL ENGINEERING
CHALMERS UNIVERSITY OF TECHNOLOGY
Gothenburg, Sweden 2025
www.chalmers.se

BACHELOR THESIS 2025

Insulation Resistance Monitoring for HVDC systems in automotive applications

Asbjørn Rohde, Robert Kandel

Department of Electrical Engineering
CHALMERS UNIVERSITY OF TECHNOLOGY
Gothenburg, Sweden 2025

Insulation Resistance Monitoring for HVDC systems in automotive applications
A comparison of IRMUs by theory and experiment
Asbjørn Rohde, Robert Kandel

Supervisor: Josip Vukusic, Department of Microtechnology and Nanoscience
Co.Supervisor: Diego Gil Rubio, Volvo GTT
Examiner: Thomas Hammarström, Department of Electrical Engineering

Bachelor Thesis 2025
Department of Electrical Engineering
Electric Power Engineering
Chalmers University of Technology
SE-412 96 Gothenburg
Telephone +46 31 772 1000

Cover: An illustration of two insulation monitoring methods, made with the help from ChatGPT 2025-05-15.

Typeset in LaTeX
Printed by Chalmers Reproservice
Gothenburg, Sweden 2025

ABSTRACT

As electric vehicle and renewable-energy systems push toward ever-higher voltages, reliable insulation resistance monitoring (IRM) becomes critical to ensure safety, prevent insulation degradation, and maintain system availability. Key IRM performance parameters include common-mode and delta-voltage excursions (which drive dielectric stress, insulation aging, and electromagnetic compatibility risk), measurement time (set by resistance–capacitance time constants, crucial for real-time fault detection), and measurement accuracy (to avoid false positives/negatives).

Results show that under balanced conditions the resistor-switching Volvo TVPDCU exhibits Δ-voltage excursions up to 263 V with floating-bus bias under 15% of pack voltage, whereas the pulse-based Bender iso175 confines ΔV to 11.3 V and holds bias within 7%. In single-pole fault tests, TVPDCU drives the healthy pole up to $\approx$ 16.9% of pack voltage (simulated hand-to-hand currents peaking at $\approx$ 1.57 A), while Bender limits it to $\approx$ 10% (currents $\approx$ 1.01 A). Both methods generate discharge energies exceeding the ISO 0.2 J safety threshold for voltages above 600 V. The balanced condition discharge energies span $\approx$ 0.20˘0.464 J (TVPDCU $\approx$ 0.02 J higher), and healthy-pole energies in fault tests range $\approx$ 0.32˘0.89 J, with faulty pole.

Despite manual data extraction and component tolerances, rigorous recalibration and transparent procedures ensure reproducibility and validity of the results. These findings inform IRM selection trade-offs voltage headroom, real-time responsiveness, accuracy, electromagnetic compliance and insulation longevity, and point to future work on active balancing, novel algorithms, and material effects under high Δ-voltage stress.

Keywords: Insulation Resistance Monitoring (IRM), High-Voltage Automotive Systems, Electric Vehicle Safety, Resistor-Switching Method, Pulse-Based Measurement, Delta Voltage Excursions, Resistance-Capacitance Time Constant, Measurement Accuracy & Sensitivity.

ACKNOWLEDGEMENTS

This Bachelor's thesis (15 credits), within the field of electrical engineering, was conducted in collaboration with Volvo Trucks, to whom we extend our heartfelt gratitude. A special thanks goes to our incredible mentors, Diego Gil Rubio and Amir Parastar, who guided us tirelessly through the intricate field of insulation resistance monitoring. Your support was unwavering, and you truly were our rocks to lean on during every step of this journey.

We would also like to give a huge thanks to Lars Malm, our lab guru, whose expertise and assistance made our tests precise and reliable. Without his invaluable help, our work would not have achieved the same level of quality.

Additionally, we would like to express our sincere appreciation to our supportive team at Volvo, our manager Maryam Javaheri, our examiner Thomas Hammarström, and our Chalmers supervisor, Josip Vukusic.

Together, we have achieved significant improvements and valuable insights into insulation resistance monitoring, potentially leading to future patents and advancements that will enhance safety within the automotive industry.

Asbjørn Rohde & Robert Kandel
Gothenburg, June 2025

List of Acronyms

Below is the list of acronyms that have been used throughout this thesis listed in alphabetical order:

AC	Alternating Current
ADC	Analog to Digital Conversion
BES	Battery Energy Storage
BMS	Battery Management System
DAQ	Data Acquisition
EKF	Extended Kalman Filtering
EMC	Electromagnetic Compatibility
EOL	End of Line
ESS	Energy Storage System
HV	High Voltage
HVDC	High-Voltage Direct Current
IEEE	Institute of Electrical and Electronics Engineers
IEC	International Electrotechnical Commission
IRM	Insulation Resistance Monitoring
IRMD	Insulation Resistance Monitoring Device
IRMU	Insulation Resistance Monitoring Unit
ISO	International Organization for Standardization
KCL	Kirchhoff’s Current Law
KVL	Kirchhoff’s Voltage Law
MCU	Micro Controller Unit
RC	Resistor–Capacitor
SR	Switching Resistor
TRL	Technology Readiness Level
TVM	Traction Voltage Monitoring
TVPDCU	Traction Voltage Power Distribution Control Unit
TVS	Traction Voltage System

Nomenclature

Below is the nomenclature of parameters that have been used throughout this thesis.

Parameters

C_1	Y capacitance in IRM circuit, positive pole to chassis
C_2	Y capacitance in IRM circuit, negative pole to chassis
C_{eq}	Equivalent Y capacitance in IRM circuit
C_n	Y capacitance in IRM circuit, negative pole to chassis
C_p	Y capacitance in IRM circuit, positive pole to chassis
Δt	Time discretization step (time interval)
ΔV	Voltage span, $V^{\max} - V^{\min}$
f_s	Sampling frequency of measurements
I_b	Simulated body current under fault condition
R_b	Body impedance (hand-to-hand), 575 Ω
R_{C1}	Current-limiting resistor in pulse method IRM circuit positive branch
R_{C2}	Current-limiting resistor in pulse method IRM circuit negative branch
R_{eq}	Equivalent pole-to-chassis resistance
R_f	Sampling resistor in pulse method IRM circuit
R_{ISO}	Equivalent resistance determined in pulse method off-line mode
R_n	Equivalent negative pole-to-chassis resistance
R_p	Equivalent positive pole-to-chassis resistance
R_{ref}	Reference resistor in switching method
R_m	Reference resistor in switching method

t	Time variable in transients
U	Nominal battery voltage
U_{ESS}	Nominal energy storage system voltage
U_{dc}	Switching method measured battery voltage
U_f^+	Pulse method measured voltage in positive half-cycle
U_f^-	Pulse method measured voltage in negative half-cycle
U_{IMD}	Pulse method voltage source contribution to pole-to-chassis voltage
U_{nc}	Switching method measured voltage in negative half-cycle
U_{pc}	Switching method measured voltage in positive half-cycle
U_s^+	Pulse voltage in positive half-cycle
%bias	Common-mode bias, $100\,\lvert\bar{V}\rvert/V_{\mathrm{pack}}$
$V^{\max}$	Maximum pole-to-chassis voltage recorded
$V^{\min}$	Minimum pole-to-chassis voltage recorded
V_N	Negative pole-to-chassis voltage
$V_{N'}$	New negative pole-to-chassis voltage measured in switching method
V_P	Positive pole-to-chassis voltage
$V_{P'}$	New positive pole-to-chassis voltage measured in switching method
τ	Time constant

Contents

List of Figures

List of Tables

STATEMENT BY THE AUTHORS

We confirm that this submission is our own work and does not include uncredited material from others or previously awarded work.

Asbjørn Rohde Signature: ____________________

Student Date: ____________________

Robert Kandel Signature: ____________________

Student Date: ____________________

Approved by:

Prof. Josip Vukusic, Ph.D. Signature: ____________________

Thesis Advisor Date: ____________________

Diego Gil Rubio, M.Sc. Signature: ____________________

External Supervisor, Volvo GTT Date: ____________________

Prof. Thomas Hammarström, Ph.D. Signature: ____________________

Examiner Date: ____________________

1

Introduction

1.1 Background Information: What is a IRMU in automotive applications

Maintaining a safe level of insulation resistance is essential to all HVDC technology safety and paramount to avoid electrical shock, personal injury and fire. In automotive applications, IRM is required by standards and regulations such as IEC 61851-23-2023 ISO 6469-1:2019 and GB 18384-2020. It is achieved through a device called an IRMU. The IRMU ensures electrical safety regarding the insulation in electrical vehicles by monitoring the insulation resistance levels between the battery poles and the chassis of the vehicle in real time, enabling the vehicle systems to react to a potential fault.

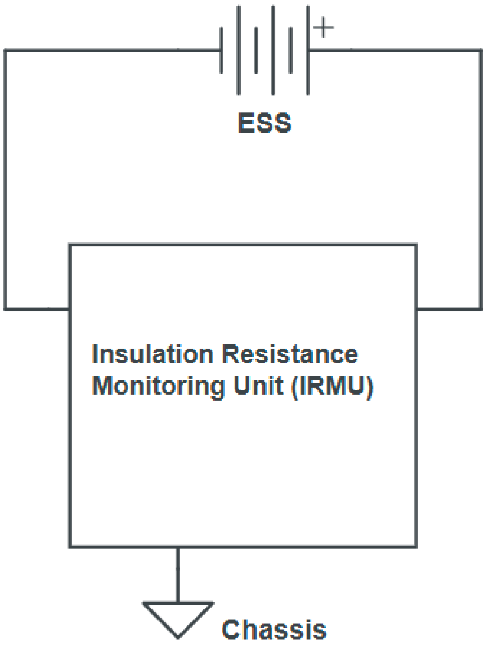

Figure 1.1: ESS (Energy storage system) connected to IRMU

Two state-of-the-art methods are predominantly utilized in IRMUs, namely switching resistors and pulse methods. Switching resistors method operates on the basis of switching between two known resistors in parallel to the equivalent resistances between the HVDC poles and the chassis respectively. Voltage and current measurements at the switched on reference resistor allow for computation of the equivalent resistance values using standard circuit analysis. The pulse method operates on the basis of AC voltage injection and measuring the systems response to the pulse through measurements of reflected voltage at a known sampling resistor. Through signal filtering, A/D conversion and mathematical analysis, the DC and AC components of the signal can be computed, and values for ohmic and capacitive impedance can be obtained.

1.2 Problem Statement

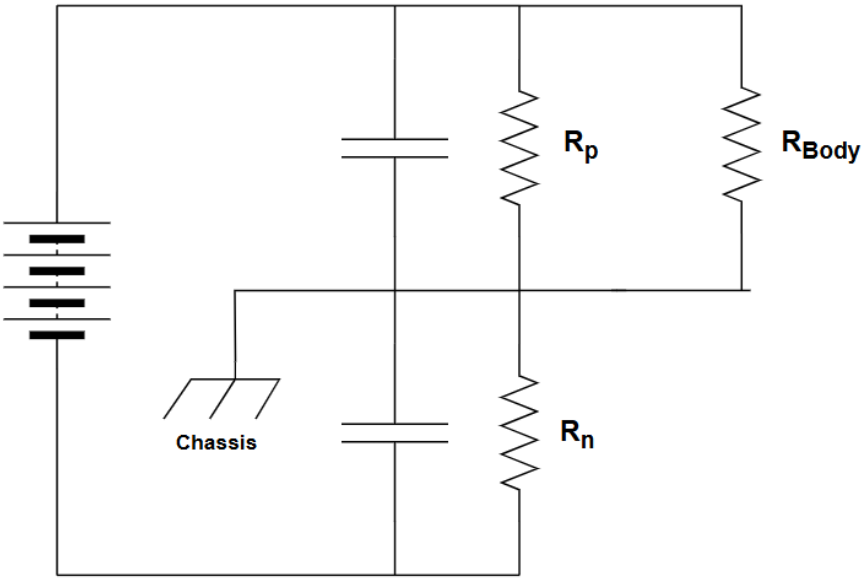

Figure 1.2: Circuit representing body impedance (R_{Body}), when touching positive pole and chassis ground in fault condition.

- This project aims to compare and evaluate the performance parameters of two IRM methods (pulse and switching) relevant to electric automotive applications, in order to bridge the current gap in knowledge.
- As voltage levels in electric vehicles continue to rise, insulation resistance monitoring (IRM) becomes increasingly critical for detecting changes in insulation within HVDC systems.
- Key performance factors for automotive applications include:
  - **Response time**: A shorter delay between fault occurrence and signal generation enhances overall vehicle safety.
  - **Voltage levels and fault current magnitude**: These influence component stress and compliance with safety standards.
  - **Accuracy:** Ensures that the vehicle reaction is not over or under dimensioned under fault scenario.

1.3 Research Objectives

The primary objective of this research is to evaluate and compare insulation resistance monitoring techniques used in HV automotive systems.

Specific objectives include: To theoretically analyze state of the art IRM methods currently utilized in commercial automotive applications. To empirically test and validate the systems through laboratory tests and simulations. Test how different parameters influence IRM accuracy, reliability, time to measure, and voltage levels and safety, thus providing a knowledge base for further research and informed decisions.

1.4 Research Questions

Based on the comparative analysis of the Bender iso175 (pulse method) and the Volvo TVPDC board (switching method) under balanced and unbalanced conditions at 600 V, 800 V, and 1000 V, this study seeks to answer the following research questions:

1. How do the experimentally measured time constants for charging and discharging (determining system time to measure) compare to the theoretical values for each method and how do the methods compare?
2. What are the maximum pole-to-chassis voltage levels and the implications for touch-current magnitudes and electric energy discharge predicted by each method under insulation-fault conditions, and how do they compare to the limits specified in IEC 61851-23, ISO 17409:2020 and ISO 64693:2018?
3. How does the IRM methods compare with respect to variations in pole-to-chassis (ΔV) voltages and what are the implications for system stability, component stress, and electromagnetic compatibility?
4. How robust is each method to measurement error when estimating equivalent pole-to-chassis resistance, and what are the and worst-case relative errors?

1.5 Significance of the Study

The significance in this study lies in bridging the gap between theoretical IRM methods and their practical implementation in safety-critical HV automotive systems. Through systematic evaluation of state-of-the-art IRM methods, theoretically and experimentally, the study contributes to both academia and industry understanding, by enabling informed decisions for IRM system selection and future optimization. Stakeholders can leverage these insights to enhance safety, reliability, and efficiency in automotive HVDC system applications.

1.6 Scope and Limitations

The scope of this study is limited to theoretical and empirical evaluation of two commercially available IRMUs and automotive HV applications.

1.7 Thesis Structure

The thesis is structured into the following main chapters:
Chapter 1: Introduction
This chapter introduces the research background, outlines objectives, defines research questions, and establishes the significance and limitations of the study.
Chapter 2: Theory
Provides an overview of relevant theory and prior research on IRM technologies, focusing on methodologies, standards, and applications.
Chapter 3: Methods
Describes the theoretical analysis methods, experimental setup, and validation procedures used to evaluate IRM system performance.
Chapter 4: Results
Presents detailed experimental data, analysis of IRM performance, comparative evaluations, and discussions on the implications of findings.
Chapter 5: Conclusion
Summarizes key findings, discusses practical implications, acknowledges limitations, validity, reliability, and suggests directions for future research.
Appendices
Include detailed mathematical derivations, additional complete data sets, and supplementary material to support the main text.

2

Theory

2.1 Important factors for IRM

2.1.1 Capacitance levels

Capacitance impacts the system mainly in two ways. First, standards in the automotive industry, such as ISO 17409:2020 regulate allowed levels of Y-capacitance as a safety measure, since capacitance determines how much energy is stored and potentially discharged in the case of an insulation fault. Secondly, the impact of capacitance on the RC time constant directly affects the time to reach steady state, and thus, time to measure. In real-time IRM, a short time to measure is desirable as faults are detected as early as possible, improving performance.

2.1.2 Maximum voltage and fault-current

Electric vehicles are subject to regular maintenance and operation in many environments. In the event of an insulation fault, the HVDC bus voltage that appears across the parasitic capacitance between the component(s) and the chassis. This creates a pathway for fault or body currents to flow to the chassis, which can then be contacted inadvertently by personnel. Thus, considering the maximum voltage magnitude from pole-to-chassis in the system is important, since any potential fault or body current magnitude depends on it. Body current is regulated as 10 mA DC in IEC61851-23 and ISO17409:2020.

2.1.3 Measurement error analysis

Measurement accuracy of the insulation resistance in HVDC systems is critical, especially in automotive applications where both safety and performance are paramount. [1,2].

Resistor tolerances have an impact on the accuracy, since in the systems there are often known resistors (R_{ref}), in a voltage divider or injection network, that is used for calculating the pole-to-chassis insulation resistances R_p and R_n. Since these directly stands in relation to R_{ref}, even smaller tolerances can result in proportional errors. For instance a 1% error in R_{ref} often leads to a similar error in the measured insulation resistance. [3].

The ADC used to sample have a direct impact on the measure ability since the quantization error due to its finite resolution.
For example, a 10-bit ADC provides $2^{10} = 1023$ discrete steps. So, for an 800V system:

$$\textbf{Step Size} = \frac{800\,\mathrm{V}}{1023} \approx 0.78\,\mathrm{V}. \tag{2.1}$$

This means that each ADC step corresponds to an approximate 0.78V increment in the measured voltage. Any further error that can be in the ADC process will have further offset accuracy and gain errors of the calculated resistances. Thus, it is important to consider the resolution when choosing the ADC. [1].

Measurement errors in real world measurements can come from noise generated from factors such as ADC input noise, electromagnetic interference, or voltage ripple from power electronics. These fluctuations may lead to both random errors and systematic offsets in the measured voltage. Filtering techniques such as EKF have been shown to substantially reduce error. One study showed that filtering reduced measurement error from around 20% down to below 5%. [4].

On overall impact, a sensitivity analysis shows that the fractional error in insulation resistances is roughly the sum of the fractional errors in R_{ref} and the measured voltage ratio. An example is Texas instruments which reference designs have achieved measurement errors below 0.598% for measurements up to 500V by employing precision, low-tolerance resistors and high resolution, stable ADCs. [1].
So, minimizing measurement errors can be achieved by using high precision components along with robust filtering and calibration techniques to reduce noise and compensate for systematic offsets. As an example, the TVPDCU does an EOL calibration that substantially reduces the error from 1.33% to 0.3% in voltage measurement.

2.2 State of the art measurement methods

A thorough understanding of the electrical circuits is paramount to establish the knowledge for evaluation of state-of-the-art IRM methods and further development withing the subject. There are two predominant methods in state-of-the-art IRM. These are of the switching resistor bridge method and the low-frequency AC pulse injection method.

2.2.1 Switching resistor method

In the switching resistor method, IRM is achieved through using switches to connect and disconnect two known resistors in parallel to the equivalent positive and negative HVDC pole-to-chassis resistance. This enables calculation of the equivalent pole-to-chassis resistances through standard circuit analysis [5].

2.2.1.1 Circuit Derivation

The circuit shown in figure 2.2 shows that the equivalent positive pole-to-chassis resistance R_P and one of the two reference resistors R_{Ref} are connected in parallel for the positive side. Similarly, the equivalent negative pole-to-chassis resistance, R_N and second reference resistor R_{Ref} are connected in parallel for the negative side of the HVDC system. By controlling the switches S_1 and S_2 in sequence, such that a single reference resistor is connected at a time, two different circuits are created as a basis for circuit analysis. For ease of analysis the circuit can be redrawn as a voltage divider (see figure 2.1 and 2.2).

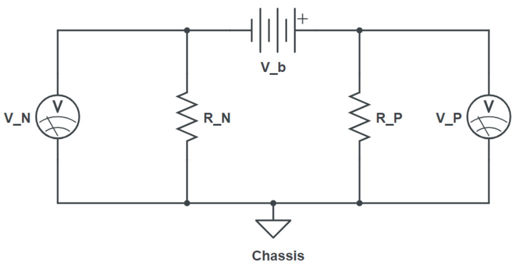

Figure 2.1: Equivalent resistances between battery poles and chassis.

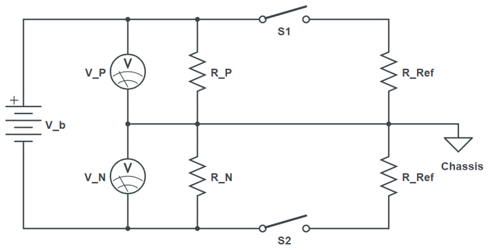

Figure 2.2: Figure 2.1 redrawn as voltage divider with added switches and parallel reference resistors.

The circuit analysis is performed by applying KCL, KVL and Ohm's Law. A system of equations will be obtained and used to calculate the equivalent resistances. To see the entire derivation, see appendix C.

The circuit analysis yields equations for R_p and R_n:

$$R_P = \frac{R_{Ref}}{V_N'}\left(1 + \frac{V_P}{V_N}\right)(V_N - V_N') \tag{2.2}$$

$$R_N = \frac{R_{Ref}}{V_P'}\left(1 + \frac{V_N}{V_P}\right)(V_P - V_P') \tag{2.3}$$

Where:

- V'_N is the measured voltage across the reference resistor between the positive pole and chassis, used to determine R_N (negative pole-to-chassis resistance).
- V'_P is the measured voltage across the reference resistor between the negative pole and chassis, used to determine R_P (positive pole-to-chassis resistance).
- V_N is the measured voltage across the negative pole-to-chassis.
- V_P is the measured voltage across the positive pole-to-chassis.

2.2.1.2 Determine stray capacitance and time constant

Consider the node of interest (the middle node) connected to three resistors and two capacitors according to figure 2.3. Each resistor leads from the node to a fixed potential (e.g. reference, chassis, or battery rail). Each capacitor leads from the same node to a low-impedance rail or chassis (assumed AC ground).

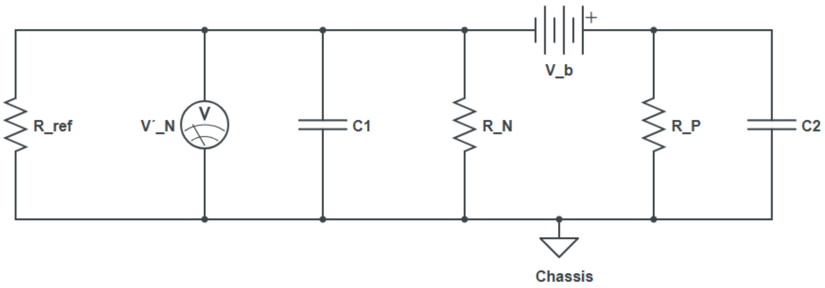

Figure 2.3: Circuit for determining equivalent capacitance and resistance of RC circuit.

For small-signal or AC analysis, the external nodes are treated as ground, Hence, from the node's perspective, all three resistors appear in parallel:

$$R_{\mathrm{eq}} = \left(\frac{1}{R_{\mathrm{ref}}} + \frac{1}{R_{\mathrm{N}}} + \frac{1}{R_{\mathrm{P}}}\right)^{-1} \tag{2.4}$$

Since each capacitor also goes from the node to AC ground, the capacitors simply add:

$$C_{\mathrm{eq}} = C_1 + C_2. \tag{2.5}$$

The time constant of the resulting single-pole RC network is the product of the equivalent resistance and capacitance:

$$\tau = R_{\mathrm{eq}}\,C_{\mathrm{eq}} = \left(\left(\tfrac{1}{R_{\mathrm{ref}}} + \tfrac{1}{R_{\mathrm{N}}} + \tfrac{1}{R_{\mathrm{P}}}\right)^{-1}\right)(C_1 + C_2). \tag{2.6}$$

By measuring the RC time constant of the signal and the insulation resistance, we are thus able to determine the Stray capacitance.

2.2.1.3 Maximum voltage difference

The maximum voltage difference is important, since it directly affects potential fault body-current magnitude. It can be obtained through voltage division. This approach results in expressions 2.7 and 2.8.

$$V_p^{max} = U_{ESS} \frac{R_p}{\frac{R_n R_{ref}}{R_n + R_{ref}} + R_p} \tag{2.7}$$

$$V_p^{min} = U_{ESS} \frac{\frac{R_p R_{ref}}{R_p + R_{ref}}}{\frac{R_p R_{ref}}{R_p + R_{ref}} + R_n} \tag{2.8}$$

2.2.1.3.1 Impact of balanced vs unbalanced circuit on pole-to-chassis voltage In a balanced system the pole-to-chassis voltages should reach equal magnitudes, thus we have the safest voltage levels possible for this method (see figure 2.4).

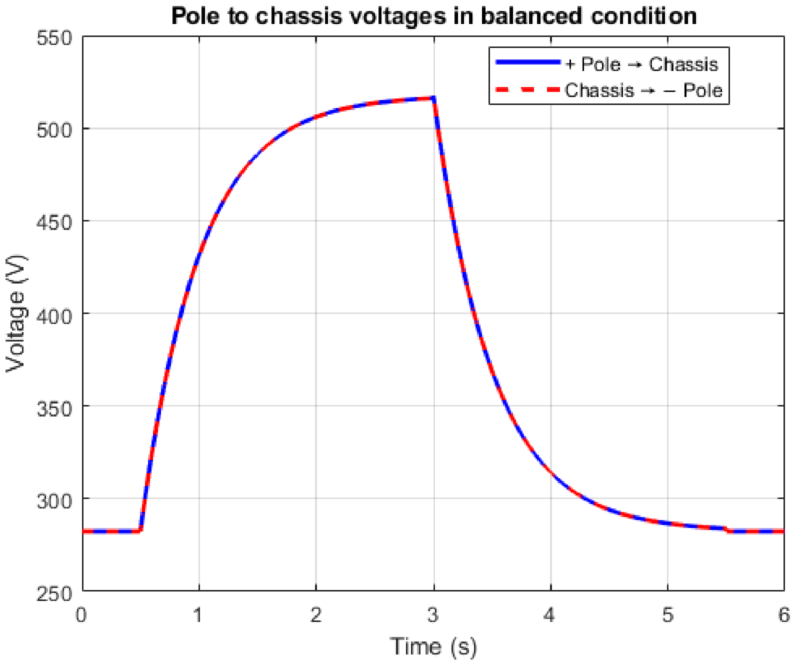

Figure 2.4: Positive pole-to-chassis voltage and chassis to negative pole in balanced conditions ($Rp = Rn = 1M\Omega$).

In an unbalanced system the maximum voltage will depend on the resistance ratio, where the largest voltage will be seen across the largest equivalent resistance as seen in figure 2.5. An unbalanced circuit is thus detrimental to safety aspects of IRM.

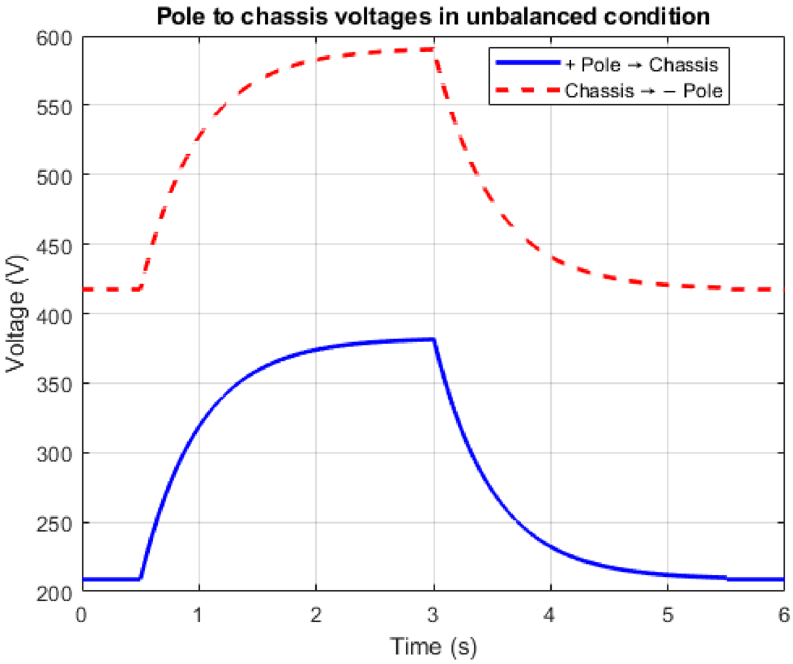

Figure 2.5: Positive pole-to-chassis voltage and chassis to negative pole in balanced conditions ($Rp = 0.5M\Omega, Rn = 1M\Omega$).

2.2.1.4 Off-line operation

In off-line operation, that is, when the battery system is physically disconnected, a DC voltage source will be needed to enable measurement in off-line mode. The operating measurement principle of the method remains unchanged.

2.2.2 Pulse method

A pulse generator injects a frequency square wave voltage signal into the system, which is analyzed by measuring its response over time. Two half-periods corresponds to the time to measure, as the response of a high and low pulse needs to be recorded for determining insulation resistances between positive and negative pole-to-chassis respectively. The signal propagates and interacts with both the insulation resistance and the Y-capacitance, which represents the parasitic capacitance between the HVDC system and the chassis. The transient and steady-state behavior of the reflected voltage waveform provides information on the insulation characteristics. The analysis of the step response is performed in two ways, using either transient or steady-state response. The transient phase is the initial response of the system and is characterized by rapid changes in voltage and current levels. The transient state is taken over by the steady-state in which voltage and current levels are stable in comparison [6].

The circuit response measurement is performed by measuring the reflected voltage waveform at a sampling resistor in series with the pulse voltage source and ground. After signal filtering and analogue to digital conversion (ADC), algorithms on a micro controller unit (MCU) analyze the step response data to compute and evaluate the impedance levels.

When the pulse is injected it travels from the pulse voltage source and splits into the positive and negative equivalent pole-to-chassis insulation resistances. These are represented as R_p and R_n. It then propagates into the two known current-limiting resistances R_{c1} and R_{c2} (see figure 2.6). The square wave signal propagates differently depending on sign and allows for equations relevant for the respective half-cycle. Combining these equations allows for mathematical computation of R_p and R_n.

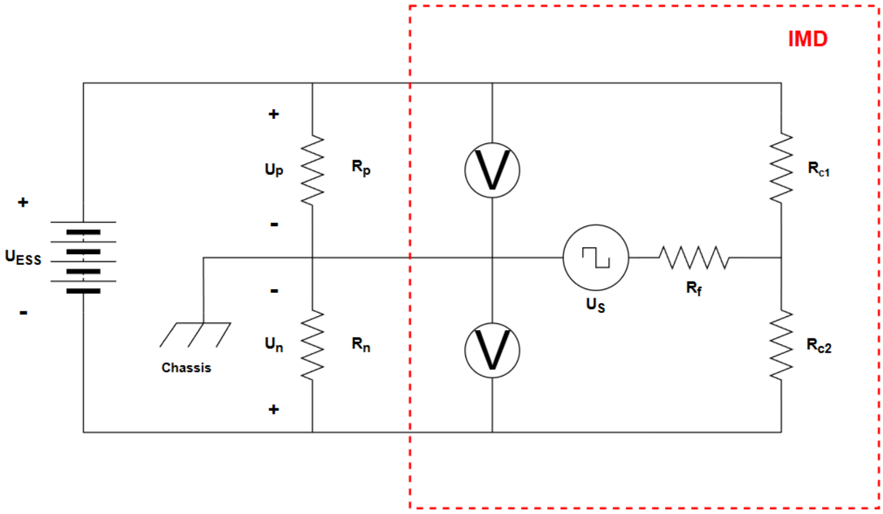

Figure 2.6: Pulse injection IMD circuit

2.2.2.1 Circuit analysis

The circuit shown in figure 2.6 is built such that the capacitors C_p and C_n are connected in parallel with R_p and R_n to account for the parasitic capacitance. A sampling-resistor, R_f, and a pulse-generator, U_s, are added in between the node of connection of the two known current-limiting resistors, R_{c1} and R_{c2}. KCL and KVL are applied through basic circuit theory to determine the equivalent resistances of the poles to chassis (see appendix A.0.1 for full derivation).

The resulting expressions are obtained as:

$$R_p = \frac{U\left[\dfrac{R_f\left(U_s^+ - U_s^-\right)}{U_f^+ - U_f^-} - \left(R_f + \frac{R}{2}\right)\right]}{\left(U_s^+ + \frac{U}{2}\right) - \dfrac{U_f^+\left(U_s^+ - U_s^-\right)}{U_f^+ - U_f^-}}. \tag{2.9}$$

$$R_n = \frac{U\left[\dfrac{R_f\left(U_s^+ - U_s^-\right)}{U_f^+ - U_f^-} - \left(R_f + \frac{R}{2}\right)\right]}{\dfrac{U_f^+\left(U_s^+ - U_s^-\right)}{U_f^+ - U_f^-} - \left(U_s^+ - \frac{U}{2}\right)}. \tag{2.10}$$

Where:

- U is the battery system voltage.
- $R = R_{c1} = R_{c2}$ (current-limiting resistors).
- U_f^+ and U_f^- are measured voltage in positive and negative half-cycle respectively.
- U_s^+ and U_s^- are square wave voltage source values during positive and negative half-cycle respectively.

2.2.2.2 Off-line operation

Off-line operation means that the battery system is disconnected from the HVDC bus. Without DC battery voltage bias, the analysis will show that we may not determine the equivalent insulation resistances R_n and R_p, between the poles and the chassis individually. According to equations A.17 and A.16 for sample voltage U_f^- and U_f^+, the battery voltage U creates an asymmetry that provides two independent equations that can be used to solve for R_n and R_p. With battery disconnected the off-line circuit is as seen in figure 2.7.

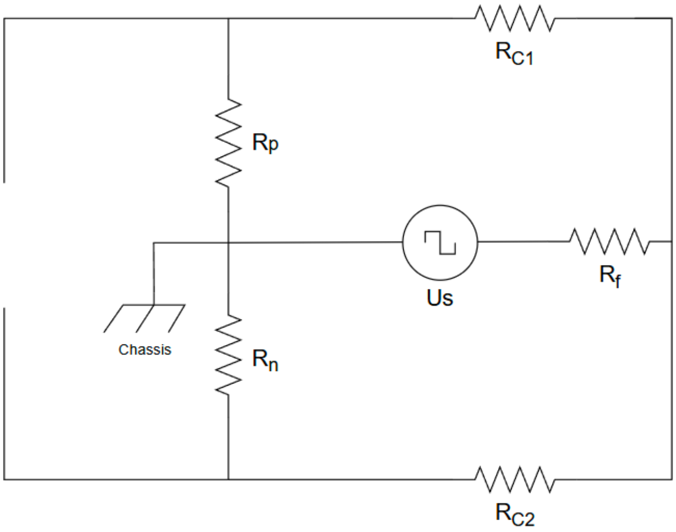

Figure 2.7: Pulse IMD circuit, offline mode

The circuit is now two parallel branches with equivalent pole-to-chassis resistances R_p and R_n in series with an internal current-limiting resistor R_{c1} and R_{c2}. These parallel branches then connect in series with the measuring resistor R_f.
Thus, if we establish

$$R = R_{C1} = R_{C2}, \tag{2.11}$$

and the equivalent resistance for the parallel resistor combinations:

$$R_{ISO} = \frac{(R_p + R)(R_n + R)}{R_p + R_n + 2R}, \tag{2.12}$$

then the measured voltage U_f through voltage division is

$$U_f = U_s \frac{R_f}{R_{ISO} + R_f}, \tag{2.13}$$

which yields

$$R_{ISO} = \frac{U_s R_f}{U_f} - R_f \tag{2.14}$$

Hence, we are limited to computing a total insulation resistance value R_{ISO} of the parallel branches including the pole-to-chassis resistances.

2.2.2.3 Derivation of Equivalent Y-capacitance, Resistance, and RC Time Constant

In analyzing the transient behavior of high-voltage DC systems, particularly when performing insulation resistance monitoring, it is crucial to accurately identify the equivalent circuit parameters. Among these parameters, the equivalent Y-capacitance, the resistance, and the resulting RC time constant significantly influence the system's voltage response to diagnostic pulses. This can be accomplished by employing the Laplace transform and superposition principle.

2.2.2.3.1 Explanation of the System The transient response observed in diagnostic methods arises fundamentally due to the system's equivalent capacitance and resistance network. Physically, these parameters represent the inherent stray capacitances between the system poles and chassis, as well as the resistive paths formed by the insulation. When a diagnostic voltage pulse is applied, the voltage across the sample resistor reflects the charging and discharging behavior dictated by these parameters. The equivalent Y-capacitance, denoted as C_{eqv}, is the parallel combination of the stray capacitances from both positive and negative poles to the chassis. The equivalent resistance, R_{eqv}, similarly combines resistive paths in the circuit into one representative value. Together, they determine the system's characteristic RC time constant, τ, which quantifies how quickly the voltage stabilizes after a transient event.

2.2.2.3.2 Key Formulas The key formulas are provided below (for full derivation see appendix B). The equivalent Y-capacitance and resistance can be calculated using:

$$\begin{aligned} C_{eqv} &= C_p + C_n, && (2.15)\\ R_{eqv} &= \frac{R_p R_n (R + 2R_f)}{(R_p + R_n)(R + 2R_f) + 2R_p R_n}. && (2.16) \end{aligned}$$

From these parameters, the system's RC time constant is directly given by:

$$\tau = R_{eqv} C_{eqv} = \frac{R_p R_n (R + 2R_f)}{(R_p + R_n)(R + 2R_f) + 2R_p R_n}(C_p + C_n). \tag{2.17}$$

The voltage response of the system can thus be simply expressed by the standard exponential behavior as:

$$\begin{aligned} \text{Charging:} \quad & U(t) = U_p^{max} + \left(U(0) - U_p^{max}\right) e^{-\frac{t}{\tau}}, && (2.18)\\ \text{Discharging:} \quad & U(t) = U(0) e^{-\frac{t}{\tau}}. && (2.19) \end{aligned}$$

where $U(0)$ is the initial voltage and U_p^{max} is the final steady state voltage. After one time constant, that is when $t = \tau$, the voltage will have changed by 63.2% of the difference between initial and final value, and thus dictates how fast the voltage can change and consequently the time to measure of the system. When discharging the capacitance, at $t = \tau$ the voltage will have dropped to about 36.8% of the initial value.

2.2.2.4 Maximum voltage

The maximum pole-to-chassis voltage can be obtained through voltage division. This approach results in expressions 2.20 and 2.21 when considering the square wave half-cycle sign change and that $R_f \to 0$ since it is much smaller than other resistors.

$$U_p^{max} = U_{IMD}\frac{\frac{R_pR_n}{R_p+R_n}}{\frac{R_pR_n}{R_p+R_n}+\frac{R}{2}} + U_{ESS}\frac{\frac{R_pR}{R_p+R}}{\frac{R_pR}{R_p+R}+\frac{R_nR}{R_n+R}}. \tag{2.20}$$

$$U_p^{min} = -U_{IMD}\frac{\frac{R_pR_n}{R_p+R_n}}{\frac{R_pR_n}{R_p+R_n}+\frac{R}{2}} + U_{ESS}\frac{\frac{R_pR}{R_p+R}}{\frac{R_pR}{R_p+R}+\frac{R_nR}{R_n+R}}. \tag{2.21}$$

2.2.2.4.1 Impact of balanced vs unbalanced circuit on pole-to-chassis voltage In a balanced system the pole-to-chassis voltages should reach equal magnitudes, thus we have the safest voltage levels possible for this method (see figure 2.8).

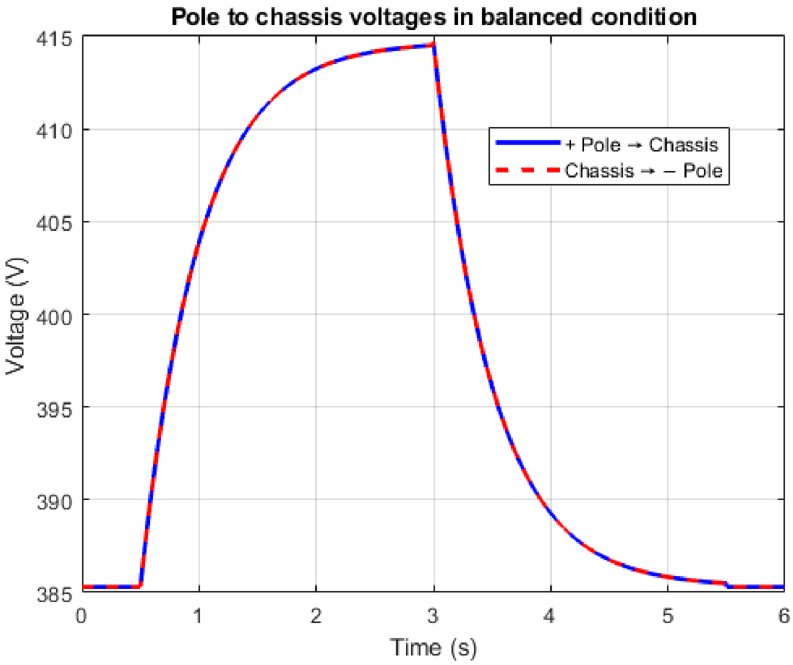

Figure 2.8: Positive pole-to-chassis voltage and chassis to negative pole in balanced conditions ($Rp = Rn = 1M\Omega$).

For unbalanced condition the average voltage is moved to a different level increasing the magnitude of one pole-to-chassis voltage depending on unbalance ratio (see figure 2.9.

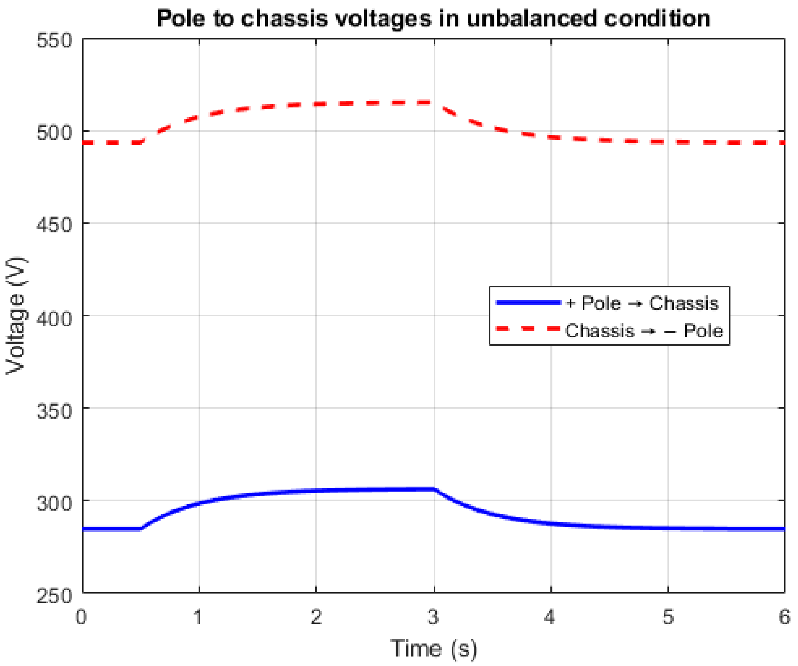

Figure 2.9: Positive pole-to-chassis voltage and chassis to negative pole in balanced conditions ($Rp = 0.5M\Omega$, $Rn = 1M\Omega$).

3

Methods

3.1 Literature review

Data was initially collected through literature review of IEEE papers, internal Volvo documentation, industry standards and patents. The literature was selected based on relevance, impact of the citation / peer reviewed, and alignment with the project objectives. Through the team at Volvo, a continuous discussion was held to collect relevant data and information from different individuals and groups. The search was kept limited to automotive applications and thus maritime and power systems applications and research were not included.

3.2 Circuit analysis

The conceptual circuits for the different IRM methods were analyzed using standard circuit theory such as Kirchov's Laws, Ohm's law, Superposition principles and the Laplace transform. By applying linear algebra to the derived expressions for the measured voltages, we arrived at the expressions for the equivalent pole-to-chassis resistances needed for computation.

3.3 Simulation and theoretical verification and comparison

A first step in verifying the mathematical expressions and the circuit theory was to simulate the circuits in a software environment.

3.3.1 LTspice

LTspice software was used to construct circuits to verify and compare the behavior of the circuits. This allowed us to obtain theoretically precise values for comparison with computed values based on derived mathematical expressions.

3.3.2 MATLAB

MATLAB is a versatile engineering software that allows, for example, mathematical computations, simulations, graph plotting, and optimization. It was utilized to verify the algebraic expressions derived from the circuit analysis. A forward and inverse approach was implemented in several scripts for various verifications and comparisons. That means we first calculated, for example, measured voltages based on actual equivalent resistance values in a forward step and then in an inverse step using these calculated measured values to calculate equivalent resistances. This approach both verifies the validity of derived algebraic expressions and produces values to compare to simulated circuit values. In addition, MATLAB was utilized to read and perform data analysis of the files with measured values from the lab.

3.3.3 Mathcad

Mathcad software is used to symbolically or numerically solve mathematical problems. It was utilized to rework mathematical expressions for measured voltages in circuits by solving for resistances of interest.

3.4 Measurement error sensitivity comparison

To make a simplified comparison without considering exact circuit components and configurations, a generalized approach was implemented. By assuming a standard error for all the measured quantities, the computation of equivalent resistances and their relative error can be compared for all methods. This will show how measurement error impacts each method, respectively. The chosen approach was to assume a measurement error of plus or minus 1 % for all measured quantities to show how a negative and positive measurement bias affects each method. The ±1 % measurement error represents a typical instrumentation tolerance level, commonly accepted within industry standards, providing a realistic baseline for comparative analysis.
Using MATLAB, the worst case relative error combination was determined. The relative error was computed as a function of a sweep of resistor values, since the relative error varies on the basis of resistor ratios. First a 8×8 dataset was produced with a custom range of resistance values. This was done to get a table with numerical values for direct comparison. In addition higher resolution datasets were plotted as heat diagrams and 3D plots (see figures 4.17, 4.18, 4.19, and 4.20) to illustrate how the error varies. Both positive and negative equivalent pole-to-chassis resistances were swept from 100kΩ to 4MΩ in 5kΩ increments.

3.4.1 Switching method error sensitivity analysis

In order to characterize the effect of measurement errors on our extraction of the resistor values R_p and R_n, a worst case analysis can be performed by applying an error scaling factor to the measured voltages. Since U_{pc} and U_{nc} are measured on the same physical resistor (in the “positive-branch” and “negative-branch” circuit configurations, respectively), we apply the same fractional error ΔU_u to both of

these voltages. Meanwhile U_{dc} has its own independent fractional error ΔU_{dc}. This yields a total number of error combinations of $2^2 = 4$.
Let the perturbed voltages be given by

$$U'_{dc} = \Big(1 + \Delta U_{dc}\Big)\, U_{dc,\mathrm{nom}}, \quad U'_{pc} = U'_{nc} = \Big(1 + \Delta U_u\Big)\, U_{u,\mathrm{nom}}. \tag{3.1}$$

The inverse formulas used to recover R_p and R_n from these measurements are

$$R_{p,\mathrm{calc}} = \frac{R_m^2\, U'_{dc}\Big(U'_{pc} - U'_{nc}\Big)}{R_m\, U'_{dc}\, U'_{nc}} = R_m\, \frac{U'_{pc} - U'_{nc}}{U'_{nc}}, \tag{3.2}$$

$$R_{n,\mathrm{calc}} = \frac{-\, R_m^2\, U'_{dc}\, U'_{pc} + R_m^2\, U'_{dc}\, U'_{nc}}{R_m\, U'_{dc}\, U'_{pc} - R_m\, (U'_{dc})^2} = R_m\, \frac{U'_{nc} - U'_{pc}}{U'_{pc} - U'_{dc}}. \tag{3.3}$$

Equations 3.2 and 3.3 are derived from voltage division expressions from the switching resistor IRM circuit (where R_m is the reference resistors switched in parallel) and by using Mathcad the explicit expressions for R_p and R_n were found.

3.4.2 Pulse method error sensitivity analysis

To assess the impact of measurement error on the pulse-method extraction of R_p and R_n, a worst case error sweep can be performed by applying an error scaling factor to the pulse voltages and the battery voltage. Since the positive- and negative-half-cycle sample voltages are measured across the same sampling resistor R_f, a common fractional error ΔU_f is applied to both $U_{f,+}$ and $U_{f,-}$, while the battery voltage U_{ESS} is assigned its own independent fractional error ΔU_{ESS}. This yields $2^2 = 4$ total error combinations.

Let the perturbed quantities be

$$U'_{ESS} = \Big(1 + \Delta U_{ESS}\Big)\, U_{ESS,\mathrm{nom}}, \quad U'_{f,\pm} = \Big(1 + \Delta U_f\Big)\, U_{f,\pm,\mathrm{nom}}. \tag{3.4}$$

The extracted resistances then follow directly from the pulse-method inversion:

$$R_{p,\mathrm{calc}} = \frac{U'_{ESS}\left(\dfrac{R_f\,(U_{s,+} - U_{s,-})}{U'_{f,+} - U'_{f,-}} \;-\; (R_f + \frac{R}{2})\right)}{\Big(U_{s,+} + \frac{1}{2}\, U'_{ESS}\Big) \;-\; U'_{f,+}\, \dfrac{U_{s,+} - U_{s,-}}{U'_{f,+} - U'_{f,-}}}, \tag{3.5}$$

$$R_{n,\mathrm{calc}} = \frac{U'_{ESS}\left(\dfrac{R_f\,(U_{s,+} - U_{s,-})}{U'_{f,+} - U'_{f,-}} \;-\; (R_f + \frac{R}{2})\right)}{U'_{f,+}\, \dfrac{U_{s,+} - U_{s,-}}{U'_{f,+} - U'_{f,-}} \;-\; \Big(U_{s,+} - \frac{1}{2}\, U'_{ESS}\Big)}, \tag{3.6}$$

3.5 Experimental comparison

The objective of the experimental comparison of the two IRM methods was to evaluate response and performance under controlled laboratory conditions. The experiments were conducted under consistent environmental conditions and each IRM board was tested individually in identical setups to ensure comparability. The test-parameters were varied within specific values to produce consistent test-scenarios. The lab-setup and all its components contribute with parasitic impedance which we have not quantified and accounted for in our test parameters. This effect was intentionally left out to reduce complexity and was deemed to affect both methods equally, thus still allowing comparison between methods.

3.5.1 Modification of circuit boards subject to testing

The circuit boards subject to testing were provided by Volvo and consisted of their own IRM switching resistor method board (see figure 3.1 and Bender's iso175$^{\text{TM}}$(see figure 3.3) pulse method board. Since the boards do not have the same internal resistances, modifications were necessary to make a relevant comparison between the IRM-systems. Thus, the replacement of resistors on the Volvo board was performed by removing existing resistors and soldering on six new 1% precision 200kΩ resistors, in series, to achieve equal internal resistance values of 1.2MΩ in each branch (see figure 3.2).

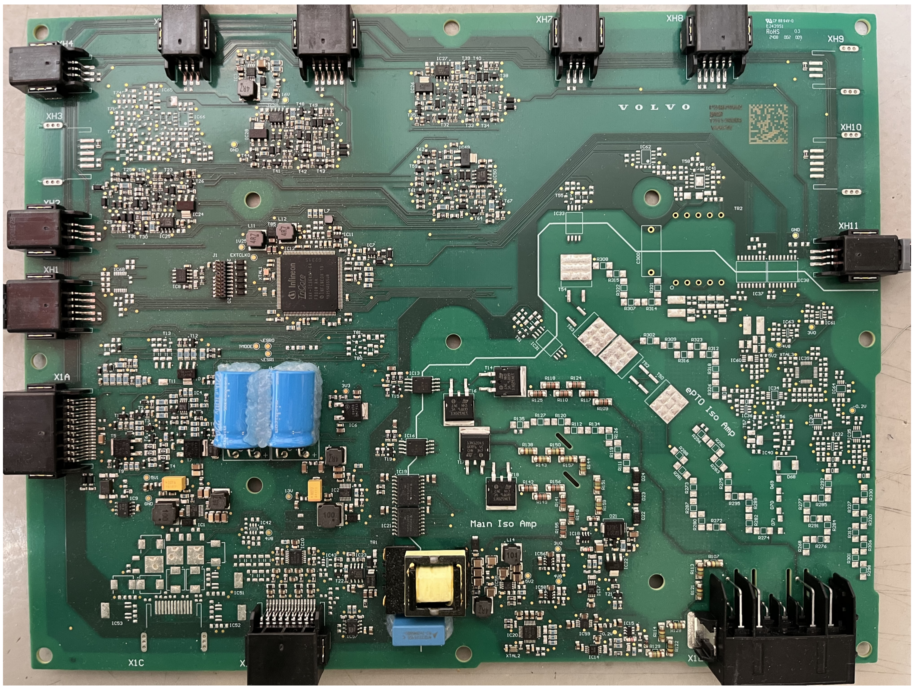

Figure 3.1: Volvo IRM board

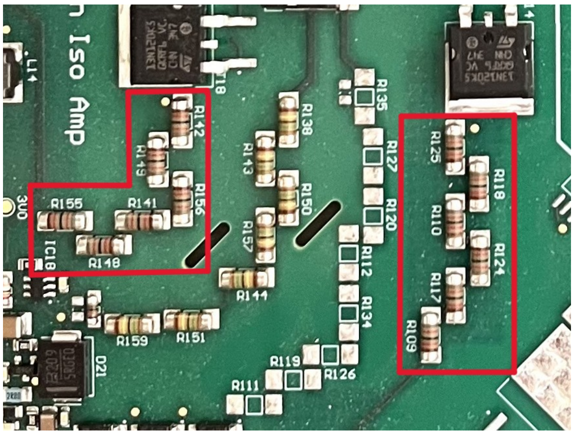

Figure 3.2: Re-soldered resistors

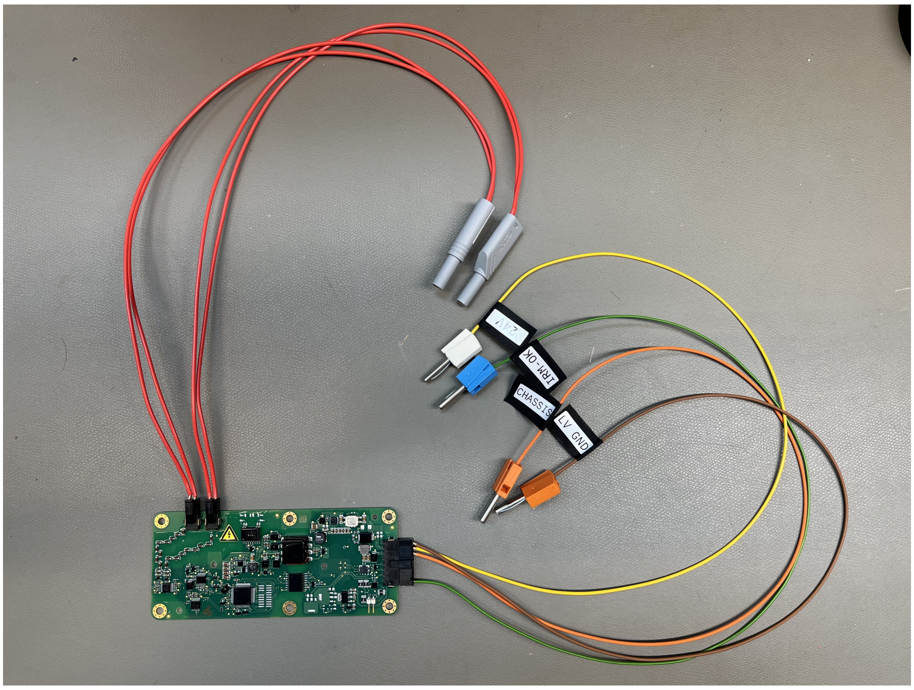

Figure 3.3: Benders iso175 IRM board

3.5.2 Lab and data acquisition

IRM units were individually tested using dedicated Volvo laboratory equipment (see figure 3.5). The read out module (HV AD ECAT Measurement Module) [7] were used to read out the data. Volvo's internal diagnostic software was used for interfacing with the IRM boards, recording test cycles, and exporting data for analysis. The collected data files were subsequently converted into MATLAB-compatible formats.

3.5.2.1 Lab-rack

An existing custom lab rack (figure 3.4) was used to simulate fault conditions and measurement scenarios relevant for IRM unit performance evaluation. The rack facilitated control and measurement of pole-to-pole and pole-to-chassis voltages (figure 3.6) [8], built in power supply (figure 3.5) [9],resistance values, and capacitor settings.

To verify the Y-capacitances and the resoldered resistances on the board, a FLUKE 1587 FC multimeter (figure 3.7) was used. The resistance from pole-to-chassis used in the testing was manually adjusted within the laboratory setup. Ceramic capacitors are measured to ensure precise test-conditions and connected separately (see 3.8).

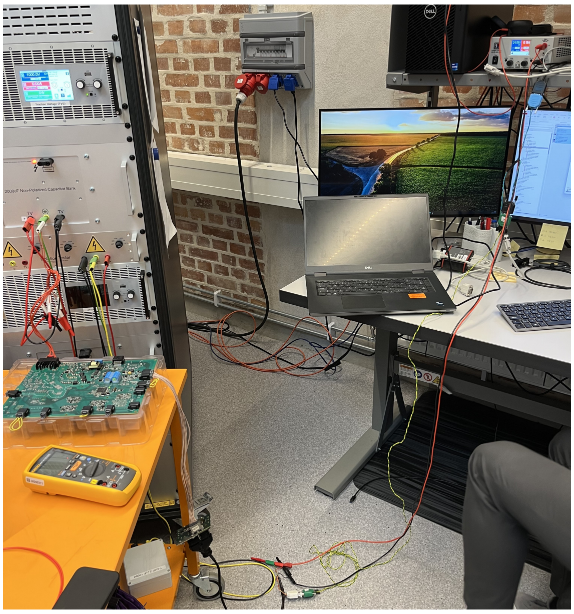

Figure 3.4: The setup in the lab with the lab-rack-insulation-module to the left, the power source for the boards up to the right and the computer for measuring/-analyzing.

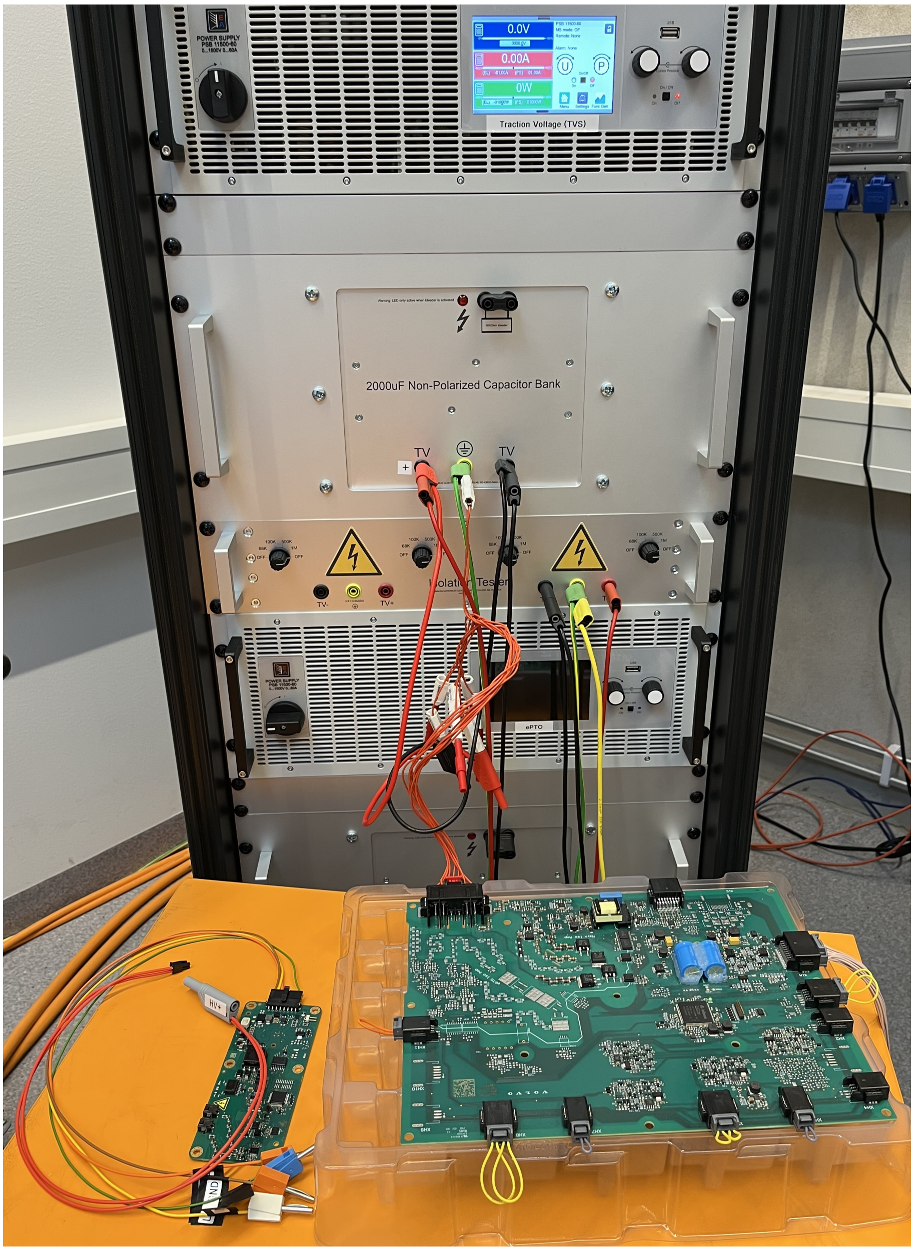

Figure 3.5: Benders iso175 IRM board to the left and Volvo board to the right. Power supply (EA-PS 11500-60 4U 30000W) in top of picture.

Figure 3.6: HV Breakout Modules 1.2 to handle pole-to-pole voltage.

Figure 3.7: FLUKE Model: 1587 FC

Figure 3.8: Ceramic capacitor 2.2 μF

3.5.2.2 Test parameters

A total of 12 tests were performed. The cases were unbalanced and balanced conditions for both methods and for three different voltage levels.

Parameter	**Volvo Method**	**Benders Method**
f_{sampling}	1 kHz	1 kHz
R_{Ref} & R_c	1.2 MΩ	2.4 MΩ
R_f	N/A	27 kΩ
Voltages	600, 800, 1000 V	600, 800, 1000 V
Y-capacitance	2.18 μF	2.18 μF

Table 3.1: Common test parameters for Volvo and Benders methods tested.

3.5.2.2.1 Equivalent pole-to-chassis resistance values and resistance correction methodology The lab rack provided the ability to adjust pole-to-chassis resistance values in steps. Resistance values were set according to table 3.2

Condition	R_p	R_n
Balanced	1 MΩ	1 MΩ
Unbalanced	100 kΩ	1 MΩ

Table 3.2: Resistance values for balanced and unbalanced configurations chosen on the lab rack.

The equivalent pole-to-chassis resistances were measured using a non-modified volvo IRM board installed into a TVPDCU connected to the data acquisition system in the lab. The TVPDCU is a unit installed in Volvo's electric trucks, but explaining this in further detail lies outside the scope of this project. In this Volvo IRMU the measured values are scaled down by 10 %. In addition two parallel measuring resistors are present in the circuit and must be corrected for.
The correction is based on the formula for parallel resistors (see equation 3.7):

$$\frac{1}{R_{\text{measured}}} = \frac{1}{R_{\text{actual}}} + \frac{1}{R_{\text{known}}} \tag{3.7}$$

Rearranging the equation allows us to isolate the actual resistance (see equation 3.8):

$$\frac{1}{R_{\text{actual}}} = \frac{1}{R_{\text{measured}}} - \frac{1}{R_{\text{known}}} \tag{3.8}$$

In the TVPDCU IRM circuit, a 20 MΩ resistor is connected in parallel with R_p, and a 10 MΩ resistor with R_n. Because of that, we applied the scaling factor of 10% on the values, then the correct resistance values were calculated. This correction enables us to obtain accurate values for both R_p and R_n, which are essential for subsequent analysis, such as examining time constants and voltage levels.

3.5.2.3 Pole-to-chassis resistance values measured with TVPDCU

Condition	**Measured R_p**	**Measured R_n**
Balanced	878 kΩ	810 kΩ
Unbalanced	80 kΩ	810 kΩ

Table 3.3: Measured resistance values from TVPDCU prior to correction. Values include the effect of known internal IRMD parallel resistors and are scaled down by 10%.

Condition	**Corrected R_p (+10%)**	**Corrected R_n (+10%)**
Balanced	1014.8 kΩ	978.15 kΩ
Unbalanced	88.38 kΩ	978.15 kΩ

Table 3.4: Corrected measured resistance values for balanced and unbalanced configurations.

3.5.2.3.1 Capacitance level and type We choose an available capacitance in the lab labeled 2.2 μF as it is close to a realistic Y-cap limit for a vehicle with maximum working voltage U above 500 V according to equation 3.9 from ISO 17409:2020 and resulting example values in table 3.5.

$$C_y = \frac{1.6mV}{U}\ [F] \tag{3.9}$$

Table 3.5: Calculated C_y from Eq. (3.9) for various pack voltages

U [V]	C_y [μF]
600	2.67
800	2.00
1000	1.60

The capacitors are ceramic, which introduces some uncertainty due to voltage dependence. We measured the capacitance to 2.18 μF when disconnected from the DC source, using the Fluke multimeter.

3.6 Ethical Considerations

When working in a laboratory setting, it was a priority to follow safety guidelines to protect all the individuals present. No personal data was handled and we adhered to the Volvo Code of Conduct. Care was taken not to disclose or spread internal or classified Volvo proprietary information, and no photographs were taken without permission.

4

Results

4.1 Presentation of Findings

4.1.1 Measured waveforms

The positive and negative pole-to-chassis voltages measured in the different test parameter scenarios with the two different IRMUs. For all the waveforms: See D.1 to D.12 in appendix. From these measured waveforms, maximum, minimum and delta voltages were extracted. Similarly the RC time constants are calculated based on the measured waveforms.

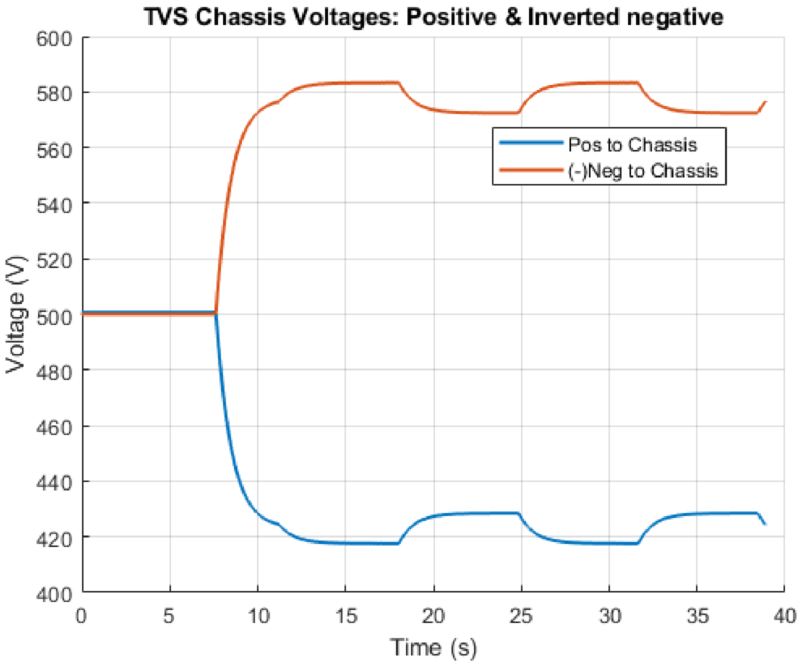

Figure 4.1: Pole-to-chassis voltages when Bender's IRMU is used at 1000V in a balanced system

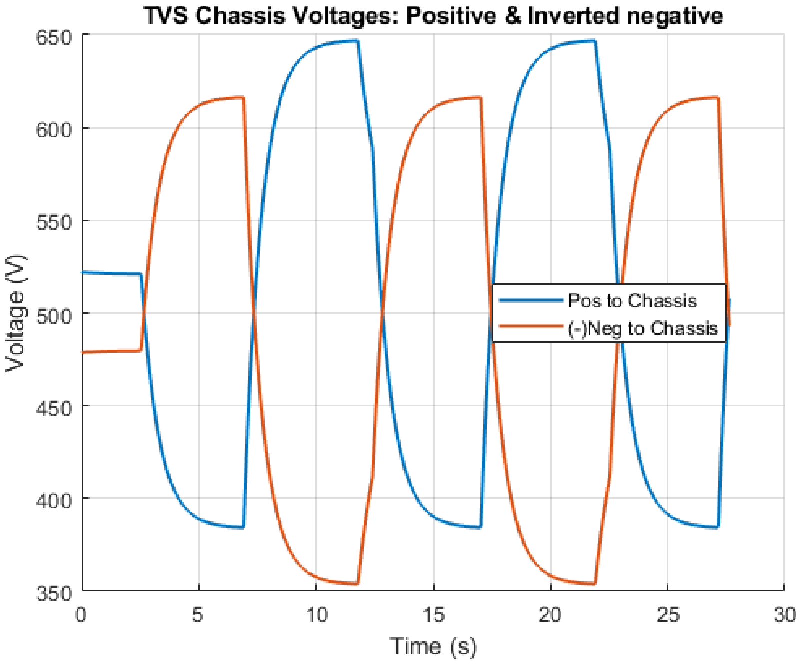

Figure 4.2: Pole-to-chassis voltages when TVPDCU's IRMU is used at 1000V in a balanced system

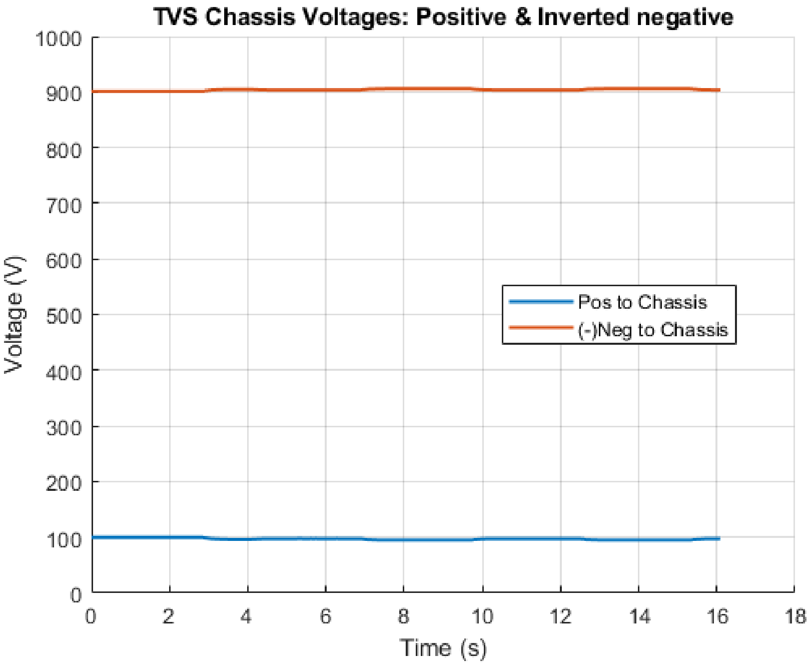

Figure 4.3: Pole-to-chassis voltages when Bender's IRMU is used at 1000V in a unbalanced system

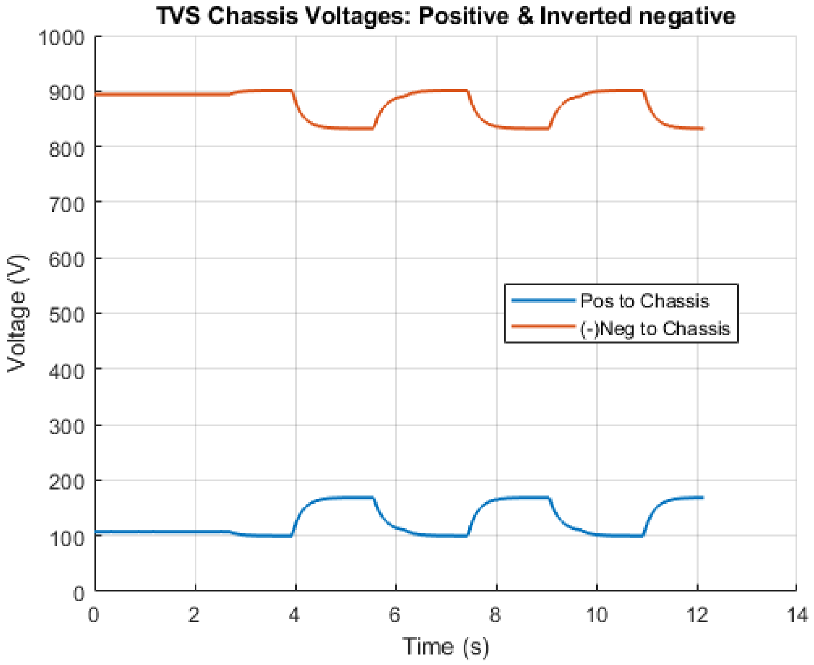

Figure 4.4: Pole-to-chassis voltages when TVPDCU's IRMU is used at 1000V in a unbalanced system

4.1.2 Maximum, minimum and delta voltage

Table 4.1: Comparison of Bender and TVPDCU measured pole-to-chassis voltages. Table shows the global maximum and minimum voltages recorded and the respective delta voltage.

Condition	System	Chassis	Max [V]	Min [V]	Δ [V]
Balanced 600 V	Bender	Positive	259.371	248.077	11.294
		Negative	-341.087	-352.381	11.294
	TVPDCU	Positive	358.187	230.525	127.662
		Negative	-212.241	-369.933	157.692
Balanced 800 V	Bender	Positive	344.017	332.753	11.264
		Negative	-456.624	-467.918	11.294
	TVPDCU	Positive	517.582	307.326	210.256
		Negative	-282.998	-493.284	210.286
Balanced 1000 V	Bender	Positive	428.694	417.399	11.295
		Negative	-572.192	-583.455	11.263
	TVPDCU	Positive	647.100	384.219	262.881
		Negative	-353.694	-616.606	262.912
Unbalanced 600 V	Bender	Positive	59.066	56.227	2.839
		Negative	-541.422	-544.261	2.839
	TVPDCU	Positive	101.221	59.707	41.514
		Negative	-499.267	-540.751	41.484
Unbalanced 800 V	Bender	Positive	78.358	75.488	2.870
		Negative	-722.344	-725.214	2.870
	TVPDCU	Positive	134.951	79.762	55.189
		Negative	-665.720	-720.940	55.220
Unbalanced 1000 V	Bender	Positive	97.650	94.811	2.839
		Negative	-903.236	-906.105	2.869
	TVPDCU	Positive	168.712	99.786	68.926
		Negative	-832.173	-901.099	68.926

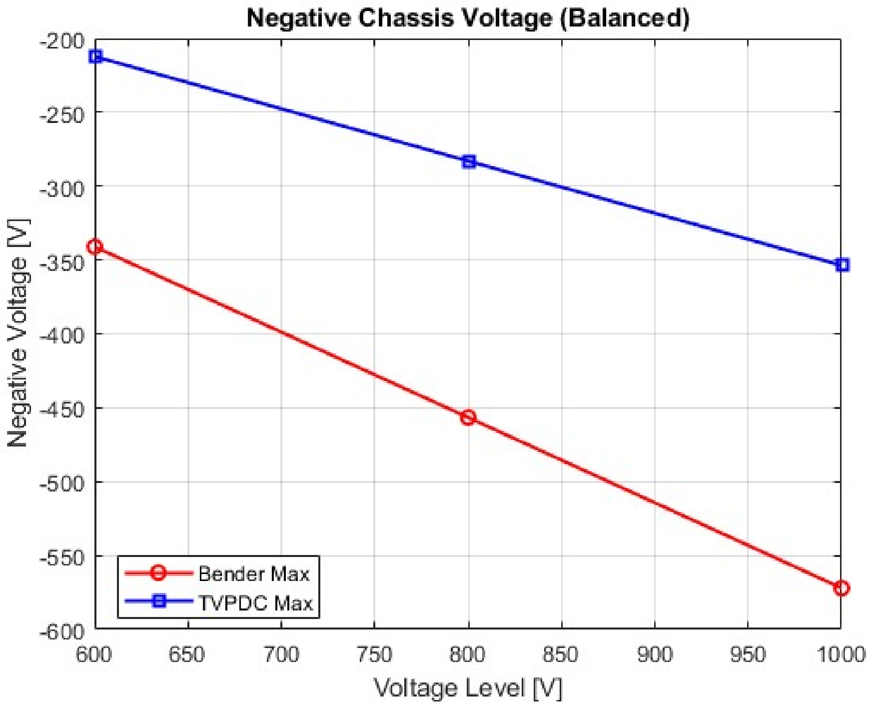

Figure 4.5: Maximum Negative Pole-to-Chassis Voltage Magnitude (as a function of applied test voltage, balanced).

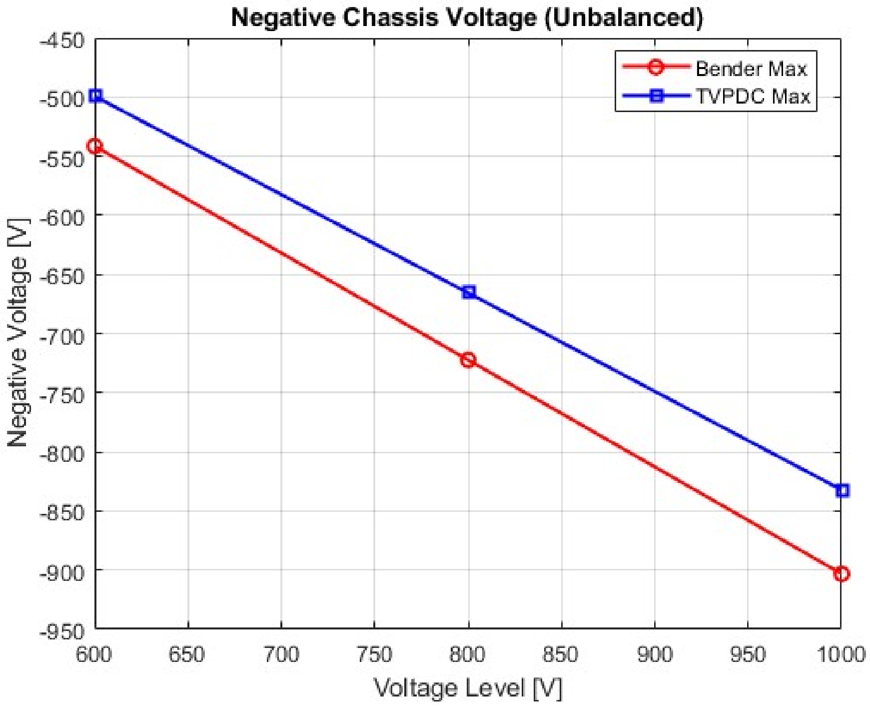

Figure 4.6: Maximum Negative Pole-to-Chassis Voltage Magnitude (as a function of applied test voltage, unbalanced).

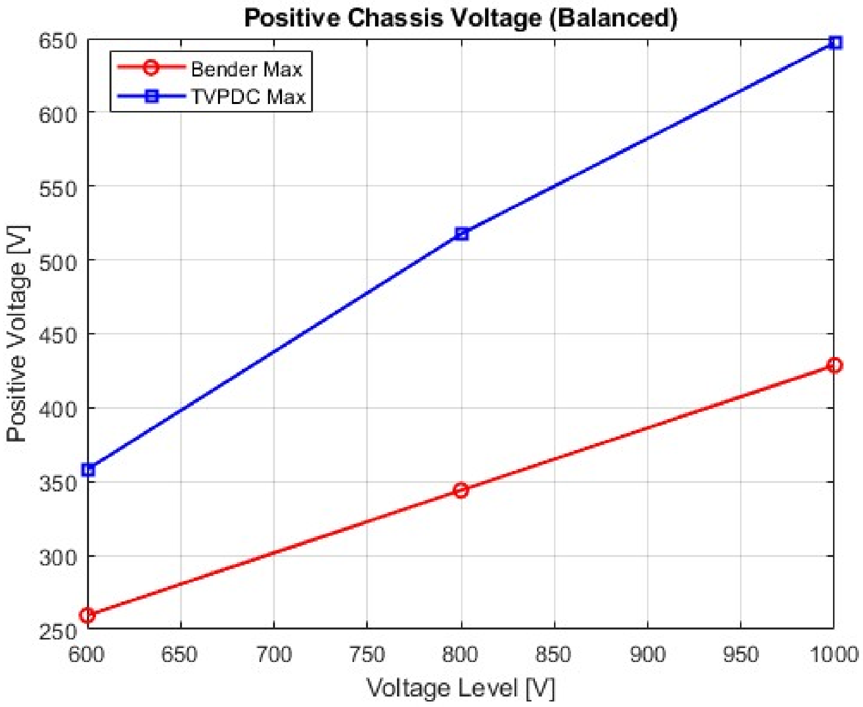

Figure 4.7: Maximum Positive Pole-to-Chassis Voltage (as a function of applied test voltage, balanced).

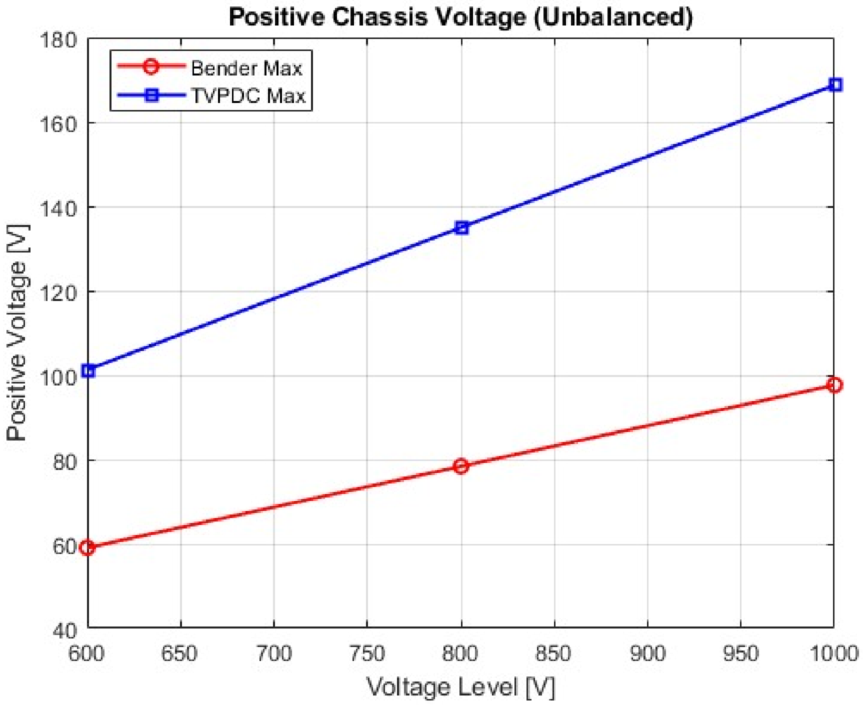

Figure 4.8: Maximum Positive Pole-to-Chassis Voltage (as a function of applied test voltage, unbalanced).

4.1.3 RC time constants by simulation

The simulations show the following theoretical time constants as a function of a sweep of equivalent pole-to-chassis resistances.

4.1.3.1 Balanced case with fixed internal IMD resistances and a sweep of pole-to-chassis resistances

Parameter	**Value**	**Description**
R_n	Sweep$\big(400\,\mathrm{k\Omega}$ to $6\,\mathrm{M\Omega}\big)$	Positive pole-to-chassis resistance
R_p	Sweep$\big(400\,\mathrm{k\Omega}$ to $6\,\mathrm{M\Omega}\big)$	Negative pole-to-chassis resistance
R_C	$2.4\,\mathrm{M\Omega}$	Current-limiting resistor in Bender's pulse method
R_{ref}	$1.2\,\mathrm{M\Omega}$	Reference resistor on the TVPDCU board
R_f	$27\,\mathrm{k\Omega}$	Measuring resistor in Bender's pulse method
C_{eq}	$2.18\,\mu\mathrm{F}$	Equivalent Y-capacitance

Table 4.2: Simulation parameters for balanced case time-constant analysis

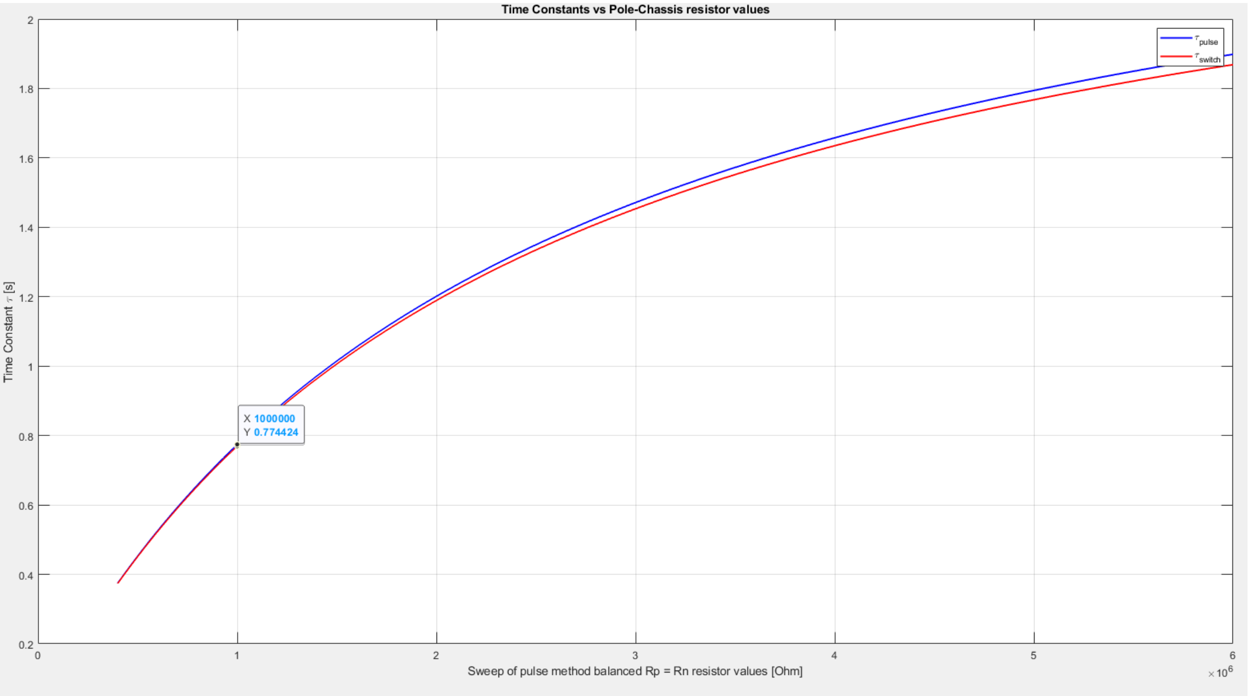

Figure 4.9: RC time constants as a function of a sweep of equivalent resistances. Balanced by $R_p = R_n$. Blue line = pulse method, red line = Switching resistor method.

4.1.3.2 Unbalanced case with fixed internal IMD resistances and a sweep of unbalanced pole-to-chassis resistances

Parameter	Value	Description
R_n	Sweep$\left(400\,\mathrm{k\Omega}\text{ to }6\,\mathrm{M\Omega}\right)$	Positive pole-to-chassis resistance
R_p	Sweep$(0.1R_n)$	Negative pole-to-chassis resistance
R_C	$2.4\,\mathrm{M\Omega}$	Current-limiting resistor in Bender's pulse method
R_{ref}	$1.2\,\mathrm{M\Omega}$	Reference resistor on the TVPDCU board
R_f	$27\,\mathrm{k\Omega}$	Measuring resistor in Bender's pulse method
C_{eq}	$2.18\,\mu\mathrm{F}$	Equivalent Y-capacitance

Table 4.3: Simulation parameters for unbalanced case time-constant analysis

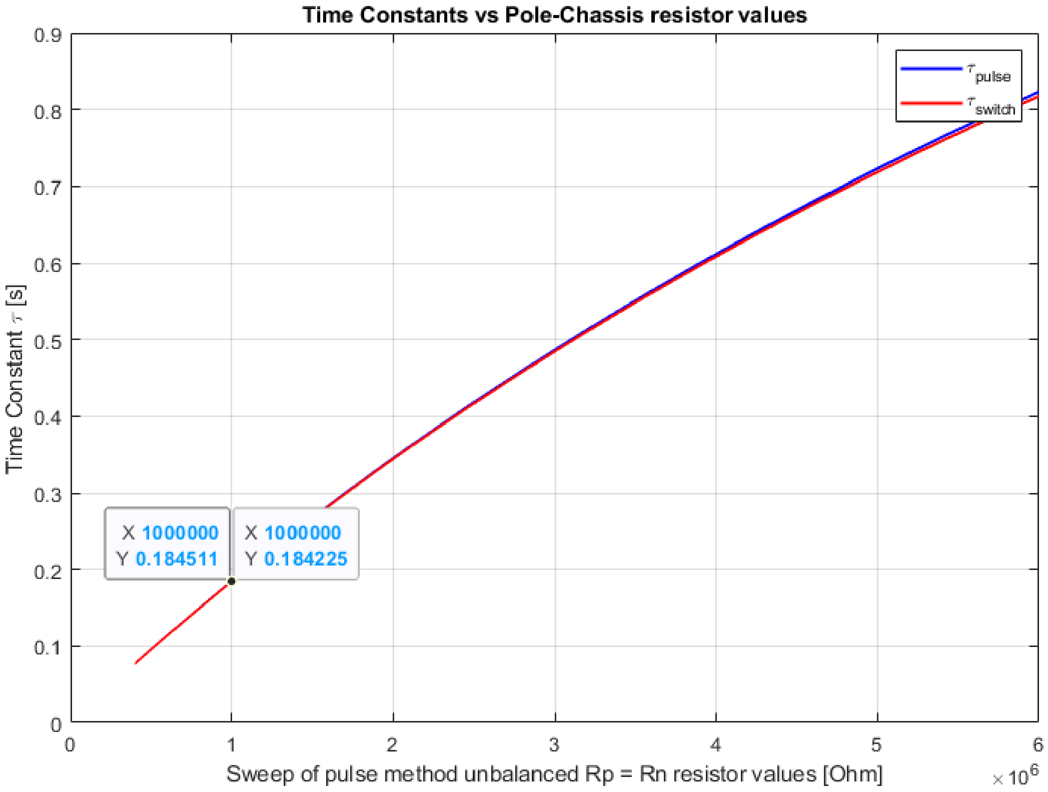

Figure 4.10: RC time constants as a function of a sweep of equivalent resistances. Unbalanced by $R_p = 0.1 \cdot R_n$, $R_n = 1M\Omega$. Blue line = pulse method, red line = Switching resistor method.

4.1.3.2.1 Simulated time constants with lab parameter values at balanced and unbalanced case:

Method	**Condition**	$\boldsymbol{\tau}$ [s]
Switching	Balanced ($R_p = 1\,\mathrm{M\Omega},\ R_n = 1\,\mathrm{M\Omega}$)	0.769
Switching	Unbalanced ($R_p = 0.1\,\mathrm{M\Omega},\ R_n = 1\,\mathrm{M\Omega}$)	0.184
Pulsed method	Balanced ($R_p = 1\,\mathrm{M\Omega},\ R_n = 1\,\mathrm{M\Omega}$)	0.774
Pulsed method	Unbalanced ($R_p = 0.1\,\mathrm{M\Omega},\ R_n = 1\,\mathrm{M\Omega}$)	0.184

Table 4.4: Time constants τ for balanced (both poles at $1\,\mathrm{M\Omega}$) and unbalanced ($R_p = 0.1\,\mathrm{M\Omega},\ R_n = 1\,\mathrm{M\Omega}$) cases.

4.1.3.3 Balanced case with fixed equivalent pole-to-chassis resistances and Internal IMD resistor value sweep

To be able to compare the systems equally, the isolation value is set to the same for the system ($R_c = R_{ref}$).

Parameter	Value	Description
R_n	$1\,\text{M}\Omega$	Positive pole-to-chassis resistance
R_p	$1\,\text{M}\Omega$	Negative pole-to-chassis resistance
R_C	Sweep$\big(400\,\text{k}\Omega$ to $2.4\,\text{M}\Omega\big)$	Current-limiting resistor in pulse method
R_{ref}	Sweep$\big(400\,\text{k}\Omega$ to $2.4\,\text{M}\Omega\big)$	Reference resistor on the switching resistor method
R_f	$27\,\text{k}\Omega$	Measuring resistor in pulse method
C_{eq}	$2.18\,\mu\text{F}$	Equivalent Y-capacitance

Table 4.5: Simulation parameters for unbalanced case time-constant analysis

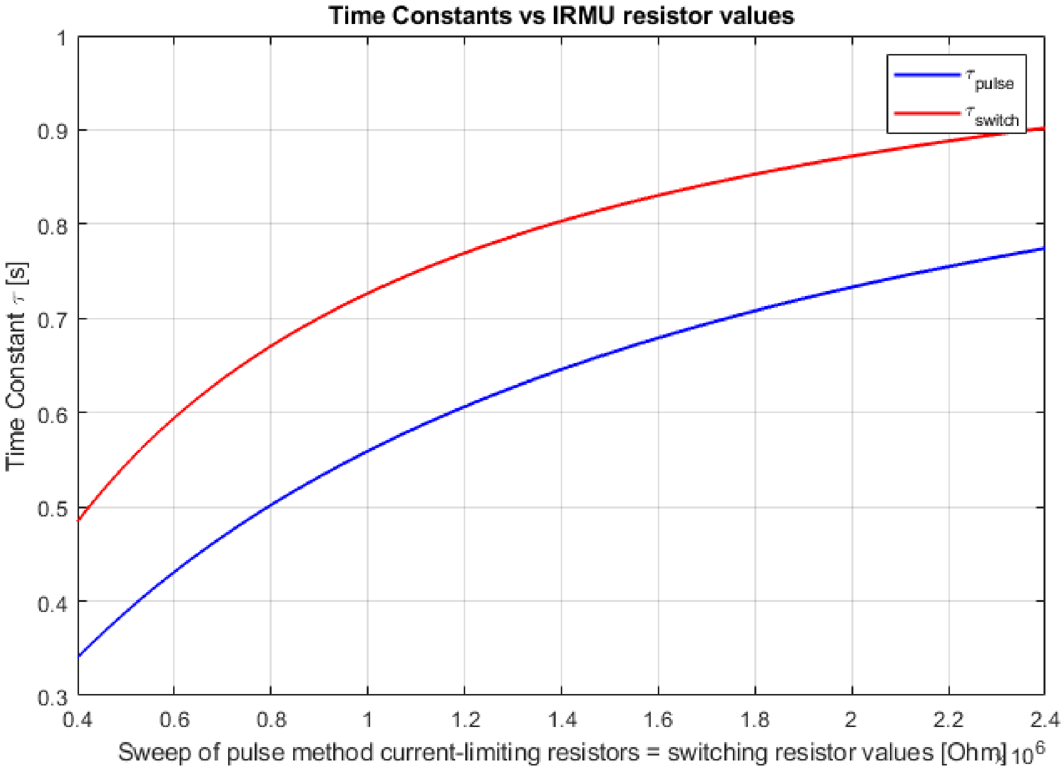

Figure 4.11: RC time constants as a function of a sweep of internal IMD resistances. Balanced by $R_p = 1M\Omega$ $R_n = 1M\Omega$ Blue line = pulse method, red line = Switching resistor method.

4.1.3.4 Unbalanced case with fixed equivalent pole-to-chassis resistances and Internal IMD resistor value sweep

To be able to compare the systems equally, the isolation value is set to the same for the system ($R_c = R_{ref}$).

Parameter	Value	Description
R_n	$1\,\mathrm{M\Omega}$	Positive pole-to-chassis resistance
R_p	$100\,\mathrm{k\Omega}$	Negative pole-to-chassis resistance
R_C	Sweep$\big(400\,\mathrm{k\Omega}$ to $2.4\,\mathrm{M\Omega}\big)$	Current-limiting resistor in pulse method
R_{ref}	Sweep$\big(400\,\mathrm{k\Omega}$ to $2.4\,\mathrm{M\Omega}\big)$	Reference resistor in the switching resistor method
R_f	$27\,\mathrm{k\Omega}$	Measuring resistor in pulse method
C_{eq}	$2.18\,\mu\mathrm{F}$	Equivalent Y-capacitance

Table 4.6: Simulation parameters for unbalanced case time-constant analysis

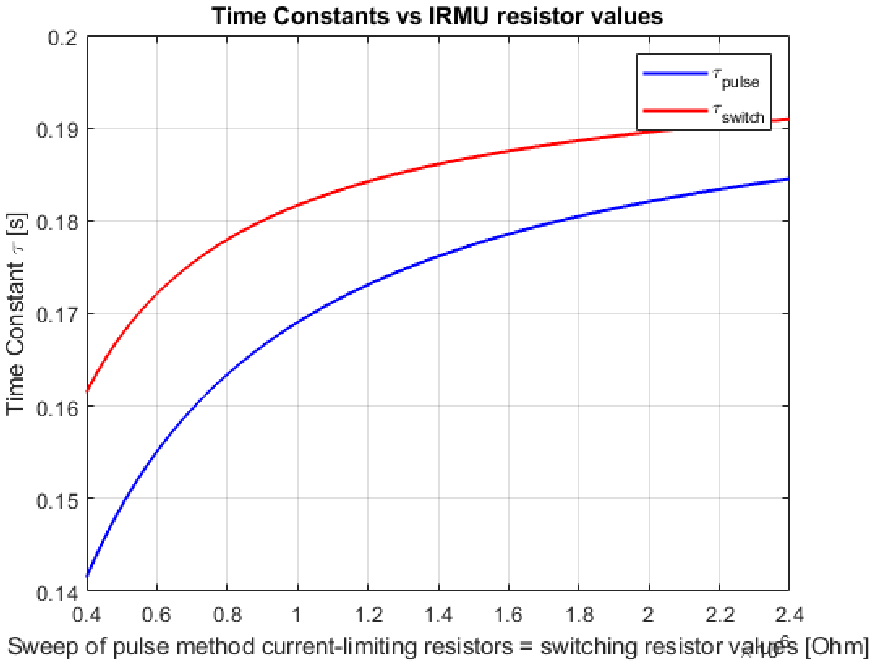

Figure 4.12: RC time constants as a function of a sweep of internal IMD resistances. Unbalanced by $R_p = 100k\Omega$ $R_n = 1M\Omega$ Blue line = pulse method, red line = Switching resistor method.

4.1.4 RC time constants by experiment

Time constants extracted from measured IRMU waveforms. For unbalanced, the conditions are set to $R_p = 1M\Omega$ & $R_n = 0.1M\Omega$, while during balanced both are set to $1M\Omega$. The capacitance is set to 2.18 μF for all the cases. Note that in some cases in figure(4.13 and 4.16), values are missing since it was not possible to read the values from the graphs, due to a bug in the TVPDCU.

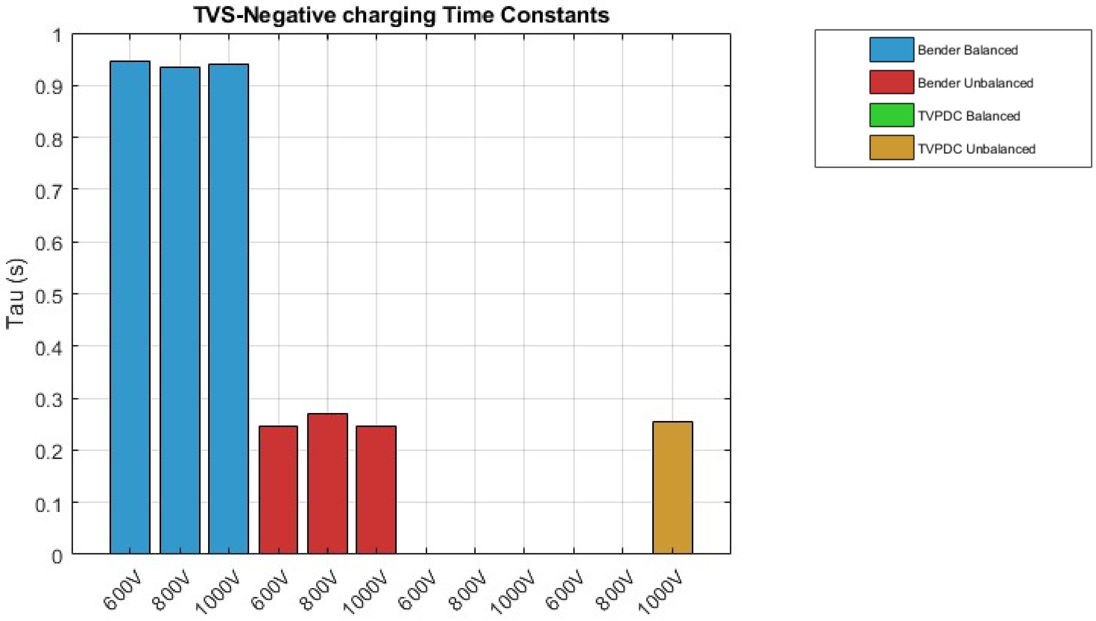

Figure 4.13: TVS Negative charging Time Constants.

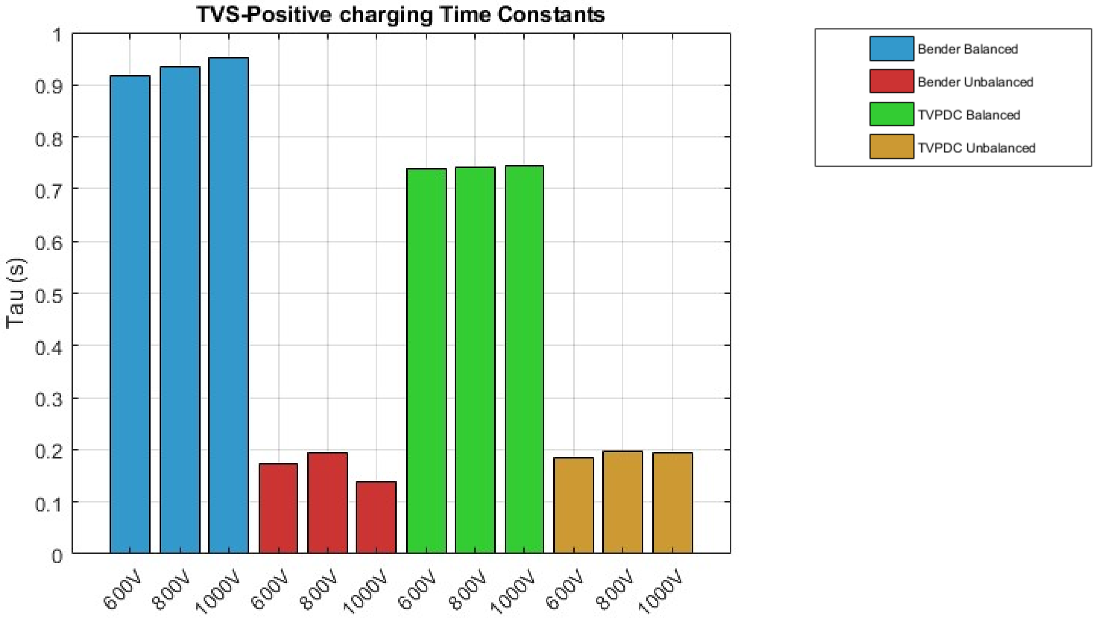

Figure 4.14: TVS Positive charging Time Constants.

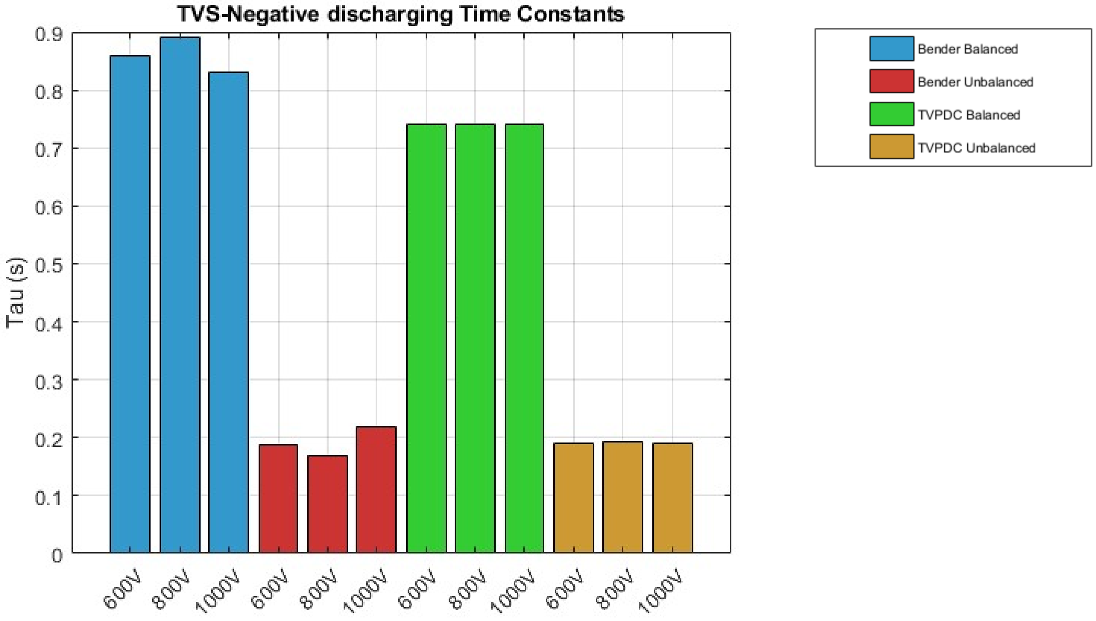

Figure 4.15: TVS Negative discharging Time Constants.

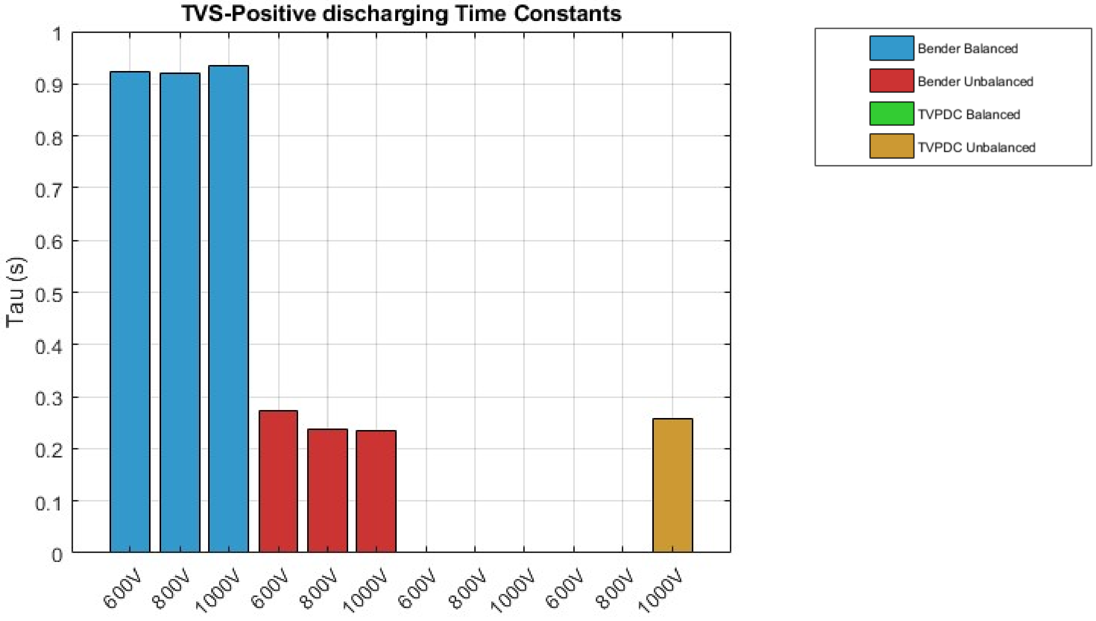

Figure 4.16: TVS Positive discharging Time Constants.

4.1.5 Switching resistor method measurement error sensitivity analysis

The nominal values for the analysis performed in MATLAB using equations 3.2 and 4.1 are seen in table 4.7.

Table 4.7: Nominal parameters for the switching-resistor method analyses

Parameter	**Value**	**Description**
R_m	$492\,\mathrm{k\Omega}$	Measurement resistor
$U_{dc,\mathrm{nom}}$	$800\,\mathrm{V}$	Nominal DC-bus voltage (battery pack)
$U_{pc,\mathrm{nom}}$	$721.027287\,\mathrm{V}$	Nominal negative pole-to-chassis voltage when $R_m \vert\vert R_p$
$U_{nc,\mathrm{nom}}$	$78.972713\,\mathrm{V}$	Nominal negative pole-to-chassis voltage when $R_m \vert\vert R_n$
err	$\pm 1\%$	Measurement error

4.1.5.1 Establishing worst case error bias combination

For each custom sweep of R_n and R_p, we computed the relative error (an 8×8 grid, 64 combinations) in R_n and R_p under each of the four $\pm 1\%$ bias scenarios (ΔU_{dc}, $\Delta U_{pc} = \Delta U_{nc}$). For each of the error sweeps, the bias combination yielding the largest error was identified. No relative error was produced for R_p. The "worst-case" counts for R_n are tallied in Table 4.8. It is clear that Case 2 ($\Delta U_{dc} = -1\%$, $\Delta U_{pc} = +1\%$) produces the highest relative error in all 64 instances for R_n. Thus, all further analysis adopts this bias pattern for R_n.
It should be noted that the non-existent relative error in R_p depends on the fact that the error cancels out when applied to equation 3.2.

Table 4.8: Occurrence counts of worst-case bias scenarios across the custom R_n sweep (64 combinations)

Case	ΔU_{dc}	$\Delta U_{pc} = \Delta U_{nc}$	**Count (of 64)**
1	-1.0%	-1.0%	0
2	-1.0%	$+1.0\%$	64
3	$+1.0\%$	-1.0%	0
4	$+1.0\%$	$+1.0\%$	0

Worst case custom resistor value sweep

The custom resistor value sweep analysis yielded the relative error in % seen in table 4.9.

Table 4.9: Relative error (%) in R_n (TVPDCU worst case: $\Delta U_{ESS} = -1\%$, $\Delta U_f = +1\%$)

$R_p \backslash R_n$ [Ω]	**300**	**20 000**	**50 000**	**75 000**	**375 000**	**1 000 000**	**2 000 000**	**3 000 000**
300	4.125	393.480	143.064	125.168	104.204	101.537	100.763	100.507
20 000	2.052	4.211	7.680	10.752	68.402	2094.061	192.550	147.374
50 000	2.034	2.937	4.342	5.544	22.460	83.854	829.170	404.262
75 000	2.030	2.658	3.629	4.452	15.461	47.946	169.071	1384.229
375 000	2.023	2.214	2.507	2.752	5.786	12.721	25.930	42.646
1 000 000	2.022	2.145	2.334	2.491	4.419	8.678	16.266	24.992
2 000 000	2.022	2.125	2.282	2.413	4.016	7.521	13.649	20.518
3 000 000	2.022	2.118	2.265	2.387	3.882	7.141	12.803	19.097

Note that for the specific resistor value combination of $R_p = 75\,k\Omega$ and $R_n = 3\,M\Omega$, an extreme relative error occurs.

The very large relative error at this single sweep point is not a MATLAB bug but an intrinsic ill-conditioning of the inverse-calculation formula. In particular:

1. **Nominal divider voltages coincide.**

$$U_{pc} = U_{dc} \frac{R_n}{R_n + (R_p \parallel R_m)}, \quad U_{nc} = U_{dc} \frac{(R_n \parallel R_m)}{R_p + (R_n \parallel R_m)}.$$

   At $(R_p, R_n) = (75\,\mathrm{k\Omega}, 3\,\mathrm{M\Omega})$, these two values become nearly equal, so their difference $U_{pc} - U_{nc}$ is extremely small.

2. **Numerator vanishes in the inverse formula.** The computation of $R_{n,\mathrm{calc}}$ uses a numerator containing terms proportional to $(U_{nc} - U_{pc})$:

$$R_{n,\mathrm{calc}} = \frac{-R_m^2\, U'_{dc}\, U'_{pc} + R_m^2\, U'_{dc}\, U'_{nc}}{R_m\, U'_{dc}\, U'_{pc} - R_m\, (U'_{dc})^2} = R_m \frac{U'_{nc} - U'_{pc}}{U'_{pc} - U'_{dc}}. \tag{4.1}$$

   As $U_{nc} - U_{pc} \to 0$, even a tiny ±1% voltage bias blows the relative error quotient up to thousands of percent.

3. **Well-conditioned elsewhere.** For most other (R_p, R_n) pairs the divider voltages differ sufficiently, keeping the denominator safely away from zero and yielding moderate relative errors. Only at this “sweet spot” does the inversion become ill-conditioned, producing the observed >1300% spike.

In practice, an IRMU would flag such an extreme resistance ratio as a fault or out-of-bounds condition long before relying on a numerical inversion in this regime.

Relative error of R_n as a function of a sweep of R_n & R_p values ranging from 100kΩ to 4MΩ.

In figures 4.17 and 4.18 it can be observed that the switching-method error surface is highly dependent on both the ratio and absolute magnitude of R_p and R_n:

- **Diagonal behaviour ($R_p = R_n$).** Along the main diagonal the relative error grows almost linearly from about 4.6% at 100kΩ up to 17% at 4MΩ.
- **Fixed R_p (varying R_n).** For a given source resistance, error increases monotonically with load:
  - At $R_p = 100\,\text{k}\Omega$, error rises from $\approx 4.56\%$ (when $R_n = 100\,\text{k}\Omega$) to $\approx 3586\%$ (when $R_n = 4\,\text{M}\Omega$).
  - At $R_p = 1\,\text{M}\Omega$, it climbs from $\approx 2.65\%$ to $\approx 35.1\%$ over the same R_n range.
- **Fixed R_n (varying R_p).** For a given load resistance, error decreases as source resistance increases:
  - At $R_n = 4\,\text{M}\Omega$, error falls from $\approx 3586\%$ (when $R_p = 100\,\text{k}\Omega$) to $\approx 17\%$ (when $R_p = 4\,\text{M}\Omega$).
  - At $R_n = 100\,\text{k}\Omega$, it decreases from $\approx 4.56\%$ down to $\approx 2.49\%$ as R_p increases.
- **Global extremes.** The absolute minimum relative error is about 2.42% (at $R_p = 4\text{M}\Omega$, $R_n = 100\text{k}\Omega$); the maximum is roughly 3586% (at $R_p = 100\text{k}\Omega$, $R_n = 4\text{M}\Omega$).
- **Design implication.** To ensure low R_n-error in the switching method, keep R_p and R_n matched within a factor of 2 and, if targeting $< 10\%$ uncertainty, operate with nominal R_n resistances below $\sim 1\text{M}\Omega$.

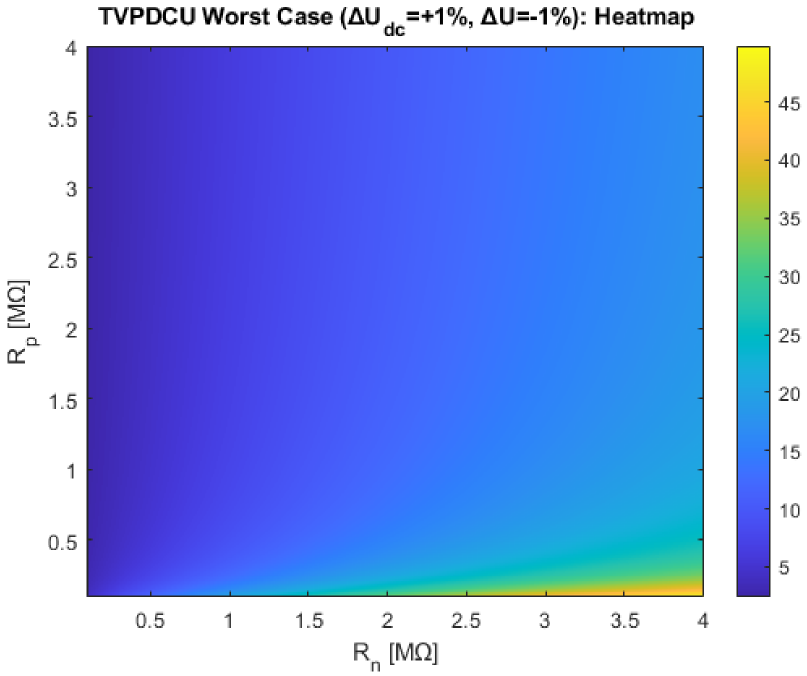

Figure 4.17: TVPDCU heatmap plot. Relative error of R_n as a function of a sweep of R_n & R_p values ranging from 100kΩ to 4MΩ.

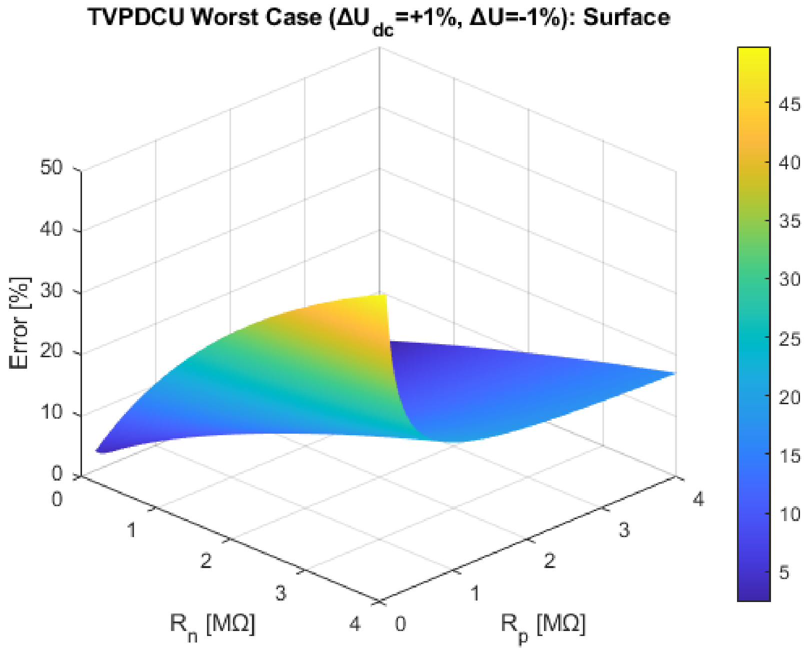

Figure 4.18: TVPDCU 3D surface plot. Relative error of R_n as a function of a sweep of R_n & R_p values ranging from 100kΩ to 4MΩ.

4.1.6 Pulse method measurement error sensitivity analysis

For nominal values for the analysis done in MATLAB for the pulse method, see table 4.10:

Table 4.10: Nominal parameters for the pulse-method analyses

Parameter	**Value**	**Description**
R_f	$27\,\mathrm{k\Omega}$	Sampling resistor
R	$2.4\,\mathrm{M\Omega}$	Current-limiting resistor
U_s^+	$50\,\mathrm{V}$	Pulse amplitude, positive half-cycle
U_s^-	$-50\,\mathrm{V}$	Pulse amplitude, negative half-cycle
U_{ESS}	$800\,\mathrm{V}$	Battery pack voltage
err	$\pm 1\%$	Measurement error

4.1.6.1 Establishing worst case bias analysis

For each (R_p, R_n) pair in the custom sweep (an 8×8 grid yielding 64 total combinations, as shown in Table 4.12), the relative error in R_n is computed under all four $\pm 1\%$ bias combinations $(\Delta U_{\mathrm{ESS}}, \Delta U_f)$. For each resistor pair, the bias scenario producing the largest error is identified, and the frequency with which each bias combination is worst is tallied across all 64 resistor combinations. These frequencies, organized by case (1–4) in Table 4.11, demonstrate that Case 3 constitutes the most frequently worst-performing bias scenario. Thus, all subsequent analyses adopted the case 3 error combination.

Table 4.11: Occurrence counts of worst-case bias scenarios across the R_n grid (64 combinations)

Case	ΔU_{ESS}	ΔU_f	**Count (of 64)**
1	-1.0%	-1.0%	9
2	-1.0%	$+1.0\%$	0
3	$+1.0\%$	-1.0%	55
4	$+1.0\%$	$+1.0\%$	0

Worst case custom resistor value sweep

The custom resistor value sweep analysis yielded the realative error in % seen in table 4.12.

Table 4.12: Relative error (%) in R_n (Case 3: $\Delta U_{ESS} = +1\%$, $\Delta U_f = -1\%$)

$R_p \backslash R_n$ [Ω]	**300**	**20 000**	**50 000**	**75 000**	**375 000**	**1 000 000**	**2 000 000**	**3 000 000**
300	8263.636	3140.774	2238.902	1803.032	489.660	141.963	24.504	16.183
20 000	4215.336	124.949	86.384	77.094	52.853	32.160	9.791	5.968
50 000	4178.163	88.327	50.586	41.972	25.078	16.116	5.960	2.319
75 000	4169.902	80.159	42.558	34.061	18.494	11.940	4.834	1.139
375 000	4156.684	67.068	29.659	21.321	7.620	4.691	2.731	1.221
1 000 000	4154.619	65.020	27.638	19.321	5.882	3.489	2.362	1.656
2 000 000	4153.999	64.405	27.031	18.721	5.359	3.124	2.249	1.791
3 000 000	4153.793	64.200	26.829	18.521	5.184	3.003	2.212	1.836

Relative error of R_n as a function of a sweep of R_n & R_p values ranging from 100 kΩ to 4 MΩ.

In figures 4.19 and 4.20 it can be observed that the Bender (pulse) method's relative error is dominated by the match between R_p and R_n, and falls off rapidly as the two differ or as their absolute size increases:

- **Diagonal behaviour ($R_p = R_n$).** When R_p and R_n are equal, the relative error is highest at the smallest resistance pair and decays monotonically with increasing magnitude:

$$R_p = R_n = 100\,\mathrm{k\Omega} \longrightarrow 25.29\% \quad \longrightarrow \quad R_p = R_n = 4\,\mathrm{M\Omega} \longrightarrow 1.60\%.$$

- **Fixed R_p, varying R_n.** For any given R_p, increasing R_n always reduces the error:
  - At $R_p = 100\,\mathrm{k\Omega}$, error falls from $\approx 25.29\%$ at $R_n = 100\,\mathrm{k\Omega}$ to $\approx 7.79\%$ at $R_n = 4\,\mathrm{M\Omega}$.
  - At $R_p = 1\,\mathrm{M\Omega}$, it drops from $\approx 14.74\%$ at $R_n = 100\,\mathrm{k\Omega}$ to $\approx 1.01\%$ at $R_n = 4\,\mathrm{M\Omega}$.
- **Fixed R_n, varying R_p.** Conversely, for any given R_n, increasing R_p also reduces the error:
  - At $R_n = 100\,\mathrm{k\Omega}$, error goes from $\approx 25.29\%$ at $R_p = 100\,\mathrm{k\Omega}$ to $\approx 14.26\%$ at $R_p = 4\,\mathrm{M\Omega}$.
  - At $R_n = 1\,\mathrm{M\Omega}$, it decreases from $\approx 10.27\%$ at $R_p = 100\,\mathrm{k\Omega}$ to $\approx 2.94\%$ at $R_p = 4\,\mathrm{M\Omega}$.
- **Global extremes.**
  - *Maximum error:* $\approx 25.29\%$ at $(R_p, R_n) = (100\,\mathrm{k\Omega}, 100\,\mathrm{k\Omega})$.
  - *Minimum error:* $\approx 0.00017\%$ at roughly $(R_p, R_n) \approx (400\,\mathrm{k\Omega}, 3.84\,\mathrm{M\Omega})$, where $R_n/R_p \approx 9.6$.
- **Design implication.** To achieve less than 5% uncertainty with the pulse method, avoid operating around low-value, well-matched resistances: choose both R_p and R_n above $\sim 610\,\mathrm{k\Omega}$.

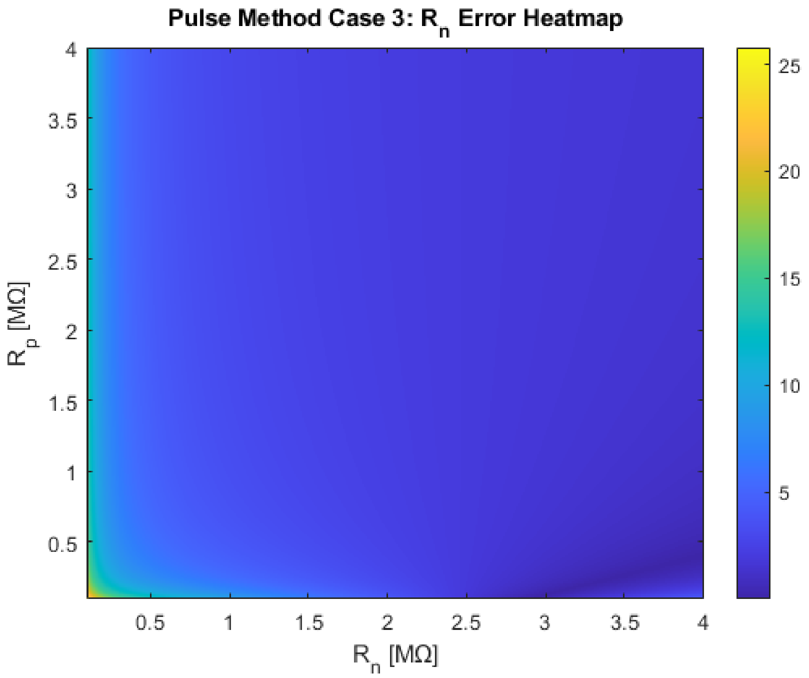

Figure 4.19: Bender method heatmap plot. Relative error of R_n as a function of a sweep of R_n & R_p values ranging from 100 kΩ to 4 MΩ.

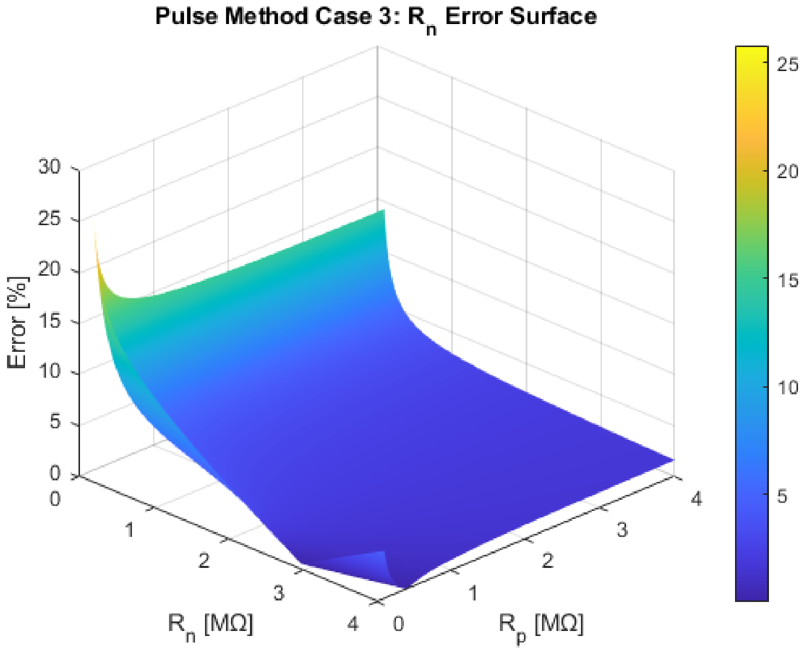

Figure 4.20: Bender method 3D surface plot. Relative error of R_n as a function of a sweep of R_n & R_p values ranging from 100 kΩ to 4 MΩ.

4.2 Analysis of Results - comparing methods

Measurements were taken under *balanced* (no internal fault) and *unbalanced* (simulated single-pole fault to chassis). The test conditions were at the nominal voltages of 600V, 800V and 1000V.

4.2.1 Balanced Network

When considering maximum pole-to-chassis voltages, the difference in how much the system is floating bus towards the negative pole, is for Bender $\approx 7\%$, whereas the TVPDCU stays within $\approx 15\%$. The delta of the pole-to-chassis voltages do never exceed 11.3V for Bender, while for the TVPDCU it lays between ≈ 127 to $\approx 263V$. When measuring from battery pole to the common chassis/ground (common-mode), this indicates a higher variation from chassis ground towards the battery pole.

The values are given by initially calculating the mean bias using equation:

$$\bar{V} = \tfrac{1}{2}\Big(V_{+} + V_{-}\Big),$$

where V_{+} and V_{-} are positive and negative pole-to-chassis voltages respectively.

Then, the answer is recalculated to give it as percentage:

$$\%\text{bias} = 100\,\frac{|\bar{V}|}{V_{\text{pack}}}.$$

One example is for Bender at 800V:

$$\bar{V} = -\tfrac{1}{2}(344-456) = -56V \quad \Rightarrow \quad 100\,\frac{56}{800} = 7\%.$$

4.2.2 Unbalanced Network

The HV bus floats due to a single fault from a single pole-to-chassis, this makes the opposite equivalent pole-to-chassis resistance have a fraction of the ESS voltage drop with respect to chassis ground, while the faulty equivalent pole-to-chassis resistance voltage drop collapses toward a significantly lower value.

Positive-pole offset for maximum voltage levels For the Bender system, it holds the positive pole at $\approx 10\%$ of the battery pack for the three test points (59V, 78V, 98V, at 600V, 800V and 1000V), whereas TVPDCU lets it rise to 16.9% (101V, 135V, 169V). Larger percentage means that the pole is further away from the chassis.

4.2.3 Maximum voltage analysis

In the case of a faulty insulation condition the risk of electric shock and body current arises. The magnitude of the body current is, according to Ohm's law, proportional to the voltage, thus it is desirable to keep the maximum and worst-case pole-to-chassis voltage at a minimum.

It is important to note that the touch current resulting from discharging capacitance only occurs under two sequential fault conditions: first, one pole develops a short to chassis, and second, the opposite pole becomes exposed and is touched, allowing current to flow from chassis through body to the exposed pole. IRM exists precisely to detect the first fault (pole-to-chassis short) and disconnect the battery pack as quickly as possible, thereby preventing the second fault (human contact with the healthy pole) from ever occurring.

From table 4.1 and figure 4.5 to figure 4.8 it can be observed that the switching method results in higher maximum voltage levels for each voltage level.

According to ISO 6469-3:2018, the permissible energy discharge is explicitly limited to 0.2 J. This guideline ensures that protective measures adequately mitigate the risk of hazardous electric shocks. Figures 4.21, 4.22 and 4.23 illustrate this limit in relation to the calculated discharge energy levels.

The capacitance values for this analysis was based on equation 4.2

$$C_y = \frac{1.6mV}{U}\ [F], \tag{4.2}$$

which yielded values in table 4.13.

Table 4.13: Calculated C_y from Eq. (4.2) for various pack voltages

U [**V**]	C_y [**F**]
600	2.67×10^{-6}
800	2.00×10^{-6}
1000	1.60×10^{-6}

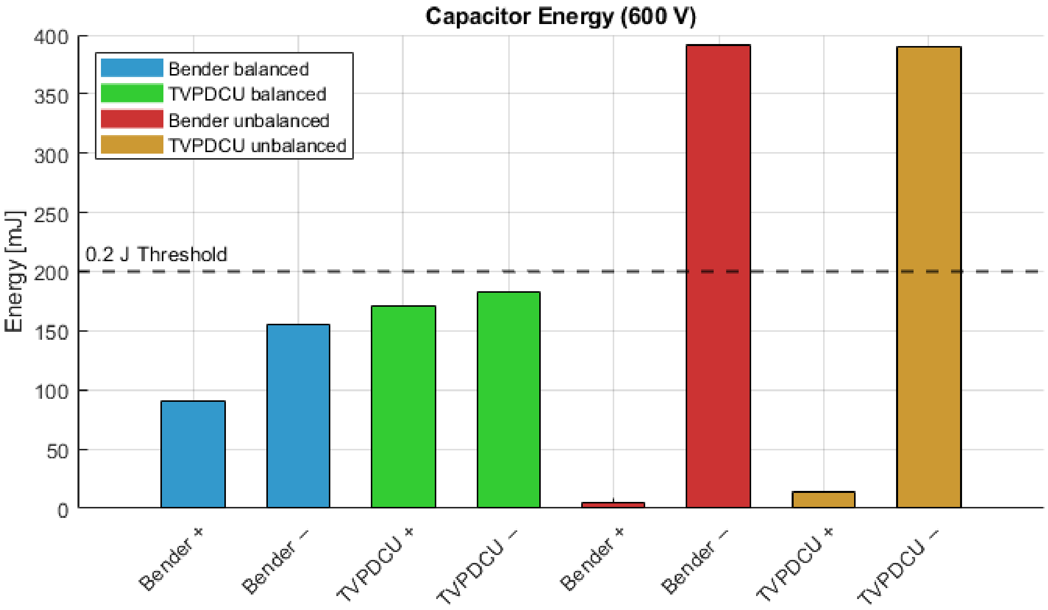

Figure 4.21: Capacitor Energy Discharge Comparison at 600 V (ISO 6469-3:2018).

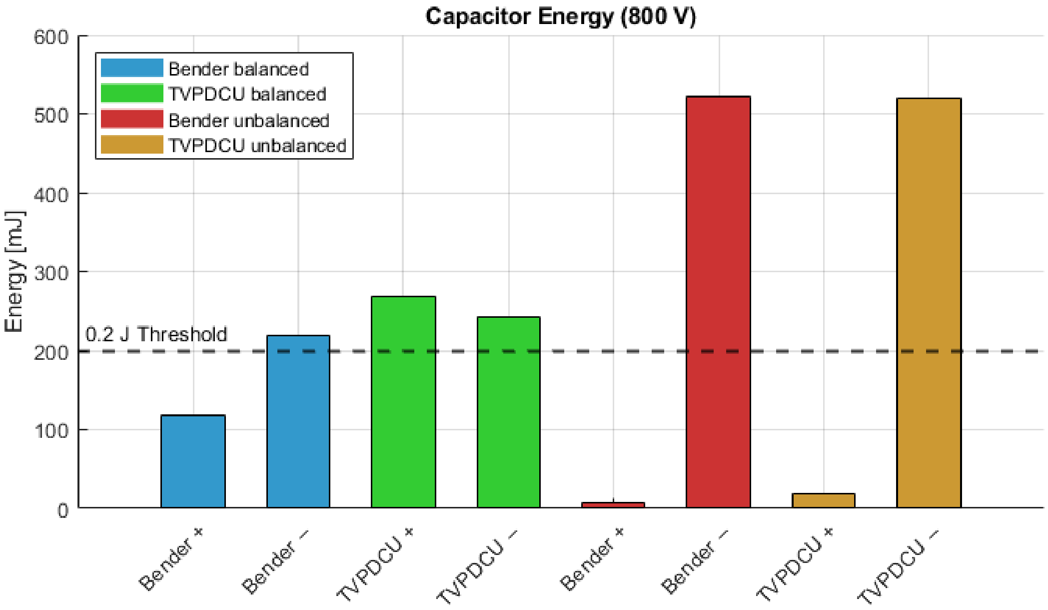

Figure 4.22: Capacitor Energy Discharge Comparison at 800 V (ISO 6469-3:2018).

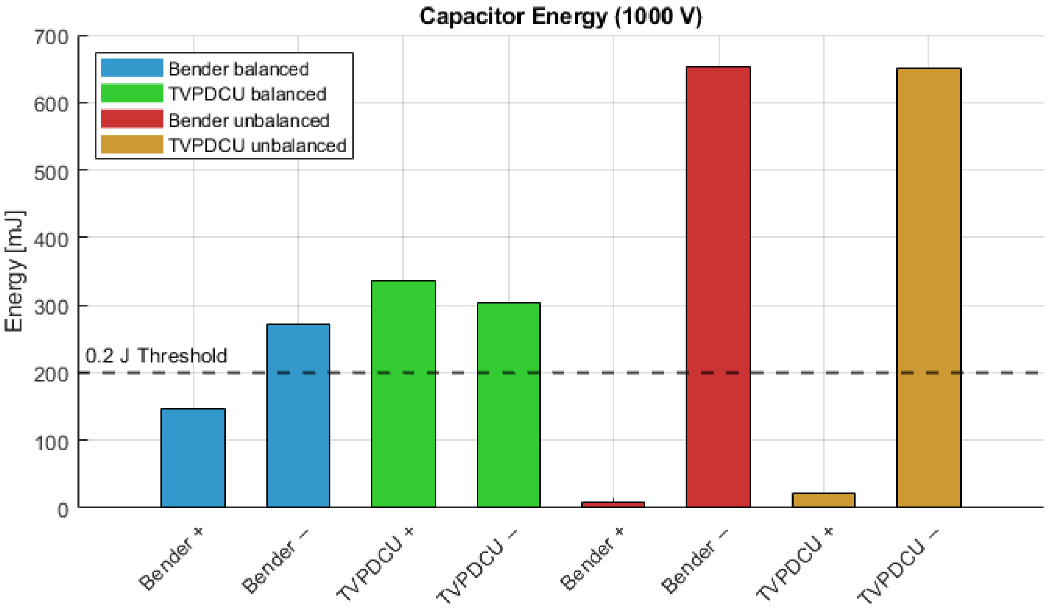

Figure 4.23: Capacitor Energy Discharge Comparison at 1000 V (ISO 6469-3:2018).

The analysis show that HVDC systems with voltages above 600 V fail to stay withing discharge energy limit of 0.2J. In addition, it can be observed that an unbalanced system with a single pole-to-chassis insulation fault will result in extreme values, with energy levels of ≈0.4 to ≈0.6 on healthy pole Y-cap and insignificant energy levels on the faulty pole Y-cap.

4.2.3.1 Simulated body currents

To clearly visualize potential body currents, we simulated the body current as a function of the maximum voltage magnitudes as a step response simulating a fault including a hand-to-hand body impedance of $R_b = 575\Omega$ as per the circuit configuration seen in figure 4.24.

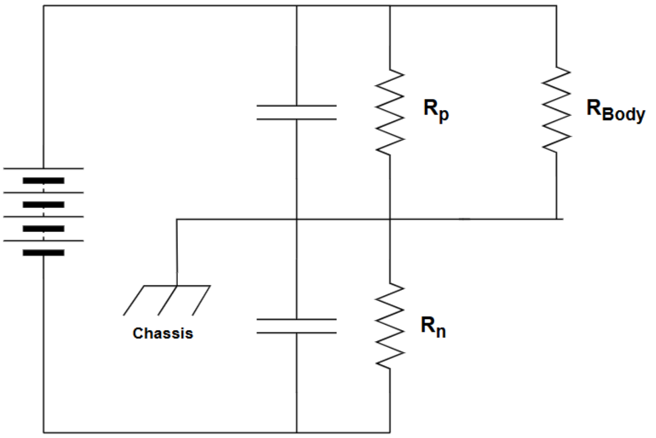

Figure 4.24: Body impedance between HVDC pole and chassis.

Note that since R_b is much smaller than other resistors it will determine the discharging of the capacitance and thus the time constants for both IRM methods will be the same. To see all the body current graphs from E.1 to E.12 (see appendix E.1).

Table 4.14: Peak touch–current magnitudes (step start values) and capacitor energy discharged ($E = \frac{1}{2} C V_{\max}^2$; $C = 2.67\,\mu$F at 600 V, $2.0\,\mu$F at 800 V, $1.6\,\mu$F at 1000 V).

Condition	System	Polarity	Peak [A]	Max [V]	Energy (600 V) [J]	Energy (800 V) [J]	Energy (1000 V) [J]
Balanced 600 V	Bender	pos	0.45108	259.371	0.0898		
		neg	0.61284	341.087	0.1553		
	TVPDCU	pos	0.62293	358.187	0.1713		
		neg	0.64336	369.933	0.1827		
Balanced 800 V	Bender	pos	0.59829	344.017		0.1183	
		neg	0.81377	467.918		0.2189	
	TVPDCU	pos	0.90014	517.582		0.2679	
		neg	0.85789	493.284		0.2433	
Balanced 1000 V	Bender	pos	0.74555	428.694			0.1470
		neg	1.01470	583.455			0.2723
	TVPDCU	pos	1.12540	647.100			0.3350
		neg	1.07240	616.606			0.3042
Unbalanced 600 V	Bender	pos	0.10272	59.066	0.0047		
		neg	0.94654	541.422	0.3913		
	TVPDCU	pos	0.17604	101.221	0.0137		
		neg	0.94044	540.751	0.3904		
Unbalanced 800 V	Bender	pos	0.13627	78.358		0.0061	
		neg	1.26120	722.344		0.5218	
	TVPDCU	pos	0.23470	134.951		0.0182	
		neg	1.25380	720.940		0.5198	
Unbalanced 1000 V	Bender	pos	0.16983	97.650			0.0076
		neg	1.57580	903.236			0.6527
	TVPDCU	pos	0.29341	168.712			0.0228
		neg	1.56710	901.099			0.6496

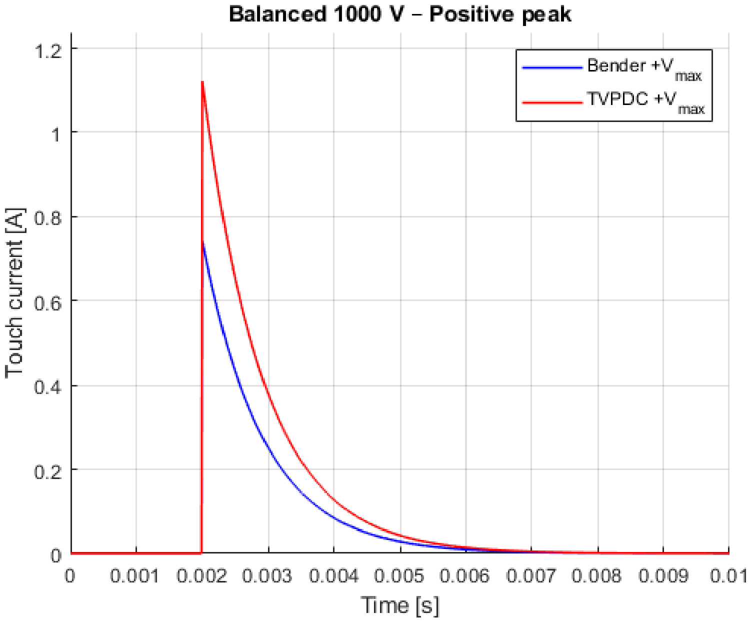

Figure 4.25: Balanced 1000V positive-peak touch current. The TVPDCU produces a larger peak current than the pulse-based Bender because it charges the Y-capacitance to chassis with a higher V_{max}. This difference can be explained by the lower mean bias for Bender of ≈ 7%, versus the ≈ 15% for the TVPDCU.

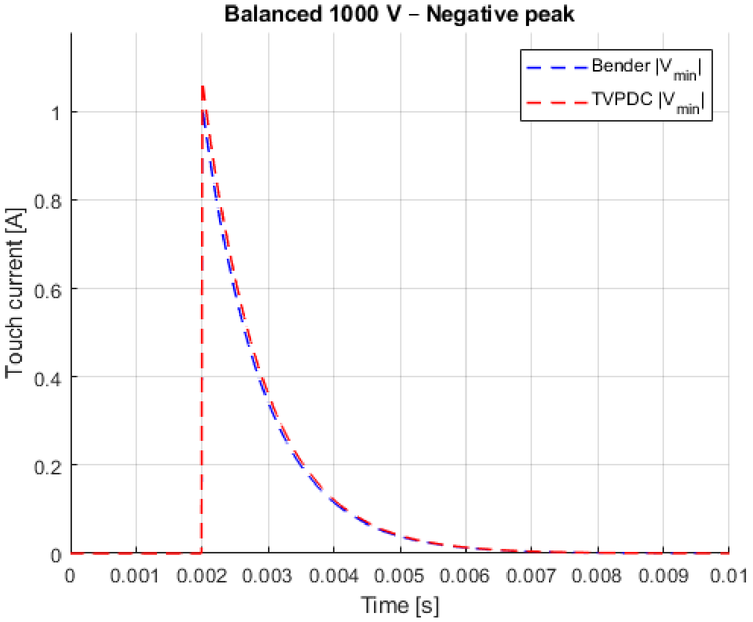

Figure 4.26: Balanced 1000V negative-peak touch current. Both IRM methods clamp the negative excursion similarly and discharge through the same body impedance, so their peak currents and decay rates nearly coincide.

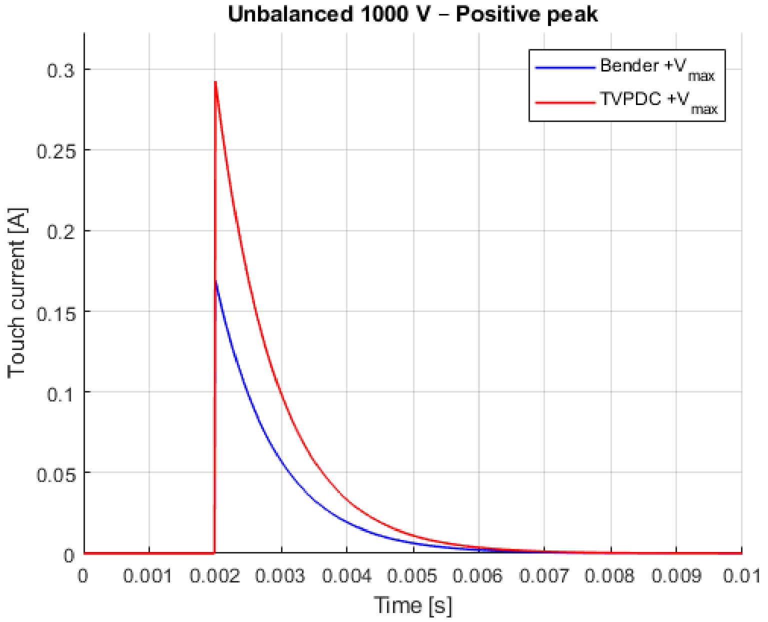

Figure 4.27: Unbalanced 1000V positive-peak touch current. The overall lower magnitudes is a result of the single-pole fault resistance ratio. In addition, the TVPDCU drives the healthy pole to a higher positive voltage than the Bender (16.9% vs 10%), hence its larger initial current, before both decay with the same time constant set by the body impedance.

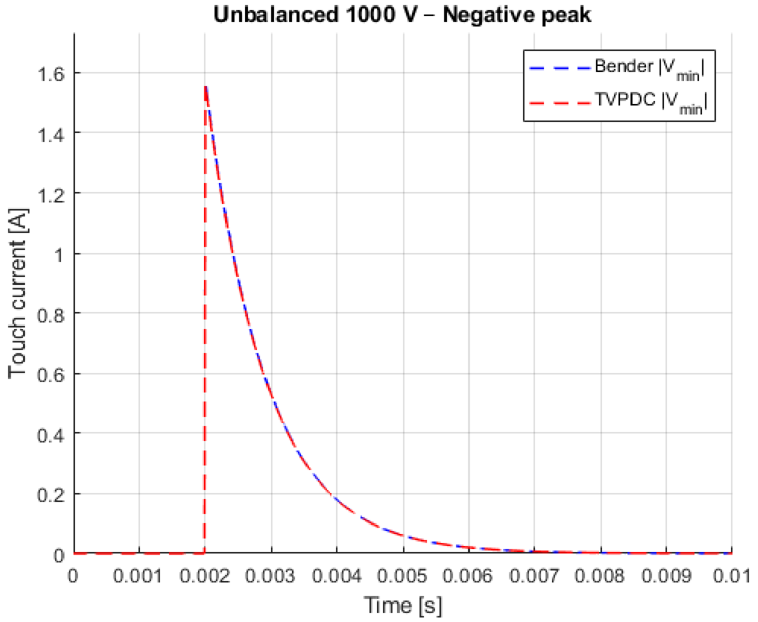

Figure 4.28: Unbalanced 1000V negative-peak touch current. Both IRM methods clamp the negative excursion similarly and discharge through the same body impedance, so their peak currents and decay rates nearly coincide. The unbalanced resistance ratio $R_n >> R_p$ results in $V_n \rightarrow U_{ESS}$ for both methods.

4.2.4 Delta voltage analysis

Looking at Table 4.1, the Bender system shows tight pole-to-chassis delta voltage which stays around 11V under all balanced conditions and about 2.8V under unbalanced conditions. In contrast, the TVPDCU (switching) system produces delta values that are an order of magnitude larger: for example, in the balanced 600V case it is 127–158V, rising to about 263V at 1000V, and even under unbalanced conditions delta ranges from roughly 41V up to nearly 69V. The resulting larger variations in IRM circuit currents could have a negative impact on stability and EMC. In addition, component and insulation stresses can affect aging.

4.2.5 Time constants analysis

The pulse method has a smaller time constant according to circuit theory when the internal IMD resistor values are kept the same, as can be seen in figure 4.11.

When the internal IMD resistors are modified to compare methods fairly, the time constants were found to be approximately the same in theory.

The measured charging time constants for balanced condition were approximately 0.9s for Bender pulse method and 0.7s for the TVPDCU switching method. Thus, the result for the pulse method shows a conflict with the expected theoretical values seen in 4.4.

For unbalanced conditions the time constants of approximately 0.2s for both methods were found to correspond with theoretical values.

4.2.6 Measurement-error sensitivity analysis

Based on the computed relative-error surfaces (figures 4.17–4.18 and 4.19–4.20), the following observations apply:

Switching-resistor method (R_n error vs. R_p, R_n)

- **Diagonal behaviour ($R_p = R_n$).** Along the main diagonal, relative error increases nearly linearly from about 4.6% at 100 kΩ to 17% at 4 MΩ (see figure 4.18).
- **Fixed R_p, varying R_n.** For a constant source resistance R_p, error grows monotonically with R_n:
  - At $R_p = 100\,\mathrm{k\Omega}$, error rises from $\approx 4.6\%$ (when $R_n = 100\,\mathrm{k\Omega}$) up to $\approx 3586\%$ (when $R_n = 4\,\mathrm{M\Omega}$) — see the vertical profile in figure 4.17.
  - At $R_p = 1\,\mathrm{M\Omega}$, it climbs from $\approx 2.7\%$ to $\approx 35.1\%$ over the same R_n span (also evident in figure 4.17).
- **Fixed R_n, varying R_p.** For constant R_n, raising R_p reduces error:
  - At $R_n = 4\,\mathrm{M\Omega}$, error falls from $\approx 3586\%$ (when $R_p = 100\,\mathrm{k\Omega}$) down to $\approx 17\%$ (when $R_p = 4\,\mathrm{M\Omega}$) — see the horizontal profile in figure 4.17.

  - At $R_n = 100\,\text{k}\Omega$, it decreases from $\approx 4.6\%$ to $\approx 2.5\%$ as R_p increases (also clear in figure 4.17).
- **Global extremes.** The minimum relative error is $\approx 2.42\%$ (at $R_p = 4$ MΩ, $R_n = 100$ kΩ), and the maximum is $\approx 3586\%$ (at $R_p = 100$ kΩ, $R_n = 4$ MΩ).
- **Design implication.** To keep switching-method error below 10%, match R_p and R_n within a factor of two and use nominal $R_n \lesssim 1$ MΩ.

Pulse method (R_n error vs. R_p, R_n)

- **Diagonal behaviour ($R_p = R_n$).** When R_p and R_n are equal, error is highest at low values and decays with magnitude:

$$R_p = R_n = 100\,\text{k}\Omega \;\longrightarrow\; 25.29\% \quad\longrightarrow\quad R_p = R_n = 4\,\text{M}\Omega \;\longrightarrow\; 1.60\%$$

  (figure 4.20).
- **Fixed R_p, varying R_n.** For any fixed R_p, increasing R_n reduces error:
  - At $R_p = 100\,\text{k}\Omega$, error falls from $\approx 25.3\%$ at $R_n = 100\,\text{k}\Omega$ to $\approx 7.8\%$ at $R_n = 4\,\text{M}\Omega$.
  - At $R_p = 1\,\text{M}\Omega$, it drops from $\approx 14.7\%$ to $\approx 1.0\%$.

  (See vertical slices in figure 4.19.)
- **Fixed R_n, varying R_p.** Likewise, for fixed R_n, raising R_p decreases error:
  - At $R_n = 100\,\text{k}\Omega$, error goes from $\approx 25.3\%$ (when $R_p = 100\,\text{k}\Omega$) to $\approx 14.3\%$ (when $R_p = 4\,\text{M}\Omega$).
  - At $R_n = 1\,\text{M}\Omega$, it decreases from $\approx 10.3\%$ to $\approx 2.9\%$.

  (Horizontal profiles in figure 4.19.)
- **Global extremes.**
  - *Maximum error:* $\approx 25.29\%$ at $(R_p, R_n) = (100\,\text{k}\Omega, 100\,\text{k}\Omega)$.
  - *Minimum error:* $\approx 0.00017\%$ near $(R_p, R_n) \approx (400\,\text{k}\Omega, 3.84\,\text{M}\Omega)$ and $(R_n/R_p \approx 9.6)$.
- **Design implication.** To achieve $< 5\%$ uncertainty with the pulse method, avoid low-value, matched resistances and choose both R_p and R_n above $\sim 610\,\text{k}\Omega$.

Overall comparison and recommendations

- Both methods show extreme (>100%) errors only for low ($\lesssim 100\,\text{k}\Omega$) or heavily unbalanced resistances, conditions that would be flagged as faults.
- In the typical mid to high $M\Omega$ range ($R_p, R_n \gtrsim 375\,\text{k}\Omega$):
  - Switching-method error remains under $\approx 17\%$.
  - Pulse-method error stays below $\approx 8\%$.
- For $< 5\%$ error in R_n:
  - **Switching:** Match R_p and R_n within a ratio of $\lesssim$1:2 and keep $R_n \lesssim 1\,\text{M}\Omega$.
  - **Pulse:** Use $R_p, R_n \gtrsim 610\,\text{k}\Omega$, or introduce sufficient mismatch to push one resistor into the multi $M\Omega$ range.

4.3 Comparison with Previous Research

Rather than focusing on a single technique or refining one specific method, this report adopts a broader perspective by evaluating several approaches both theoretically and experimentally. Our objective is not to introduce a new algorithm or accelerate measurement processes, but to enhance the existing knowledge base through systematic comparison. Although recent studies have emphasized improving IRM measurements with advanced software algorithms and faster data analysis, this report revisits fundamental circuit theory to identify the critical distinctions between methods and examine how those distinctions influence overall performance.

5

Conclusion

5.1 Summary of Findings

Our comparative study of the Bender iso175 (pulse method) and the Volvo TVPDCU board (switching resistor method) under balanced and unbalanced conditions at 600 V, 800 V, and 1000 V yields several key insights:

- **Common-mode bias:**
  - Under balanced conditions, Bender holds its floating bus mean bias within 7 % of pack voltage. TVPDCU's mean bias stays under 15 %.
  - In an unbalanced (single-pole fault) event, Bender keeps the healthy pole within ≈ 10 % of pack voltage and reduces pole separation slightly, whereas TVPDCU drives the healthy pole up to 16.9 %.
- **Extreme voltages and body-current risk:**
  - In the event of a fault, the switching method results in more hazardous energy levels and touch current magnitudes, this is because of:
    - TVPDCU exhibits higher maximum pole-to-chassis voltages.
    - Simulated hand-to-hand body currents (with 575 Ω impedance) confirm TVPDCU's larger current peaks (up to ≈ 1.57 A) versus Bender's (≈ 1.01 A) at 1000 V, underscoring elevated shock risk.
    - Using equation 5.1

      $$E = \tfrac{1}{2}\, C\, V_{\max}^2 \tag{5.1}$$

      with capacitance levels according to equation 5.2

      $$C_y = \frac{1.6mV}{U}\,\mu\mathrm{F}, \tag{5.2}$$

      balanced discharge energies for 800 V and 1000 V cases and for both methods exceed the 0.2 J limit in ISO 6469-3:2018 with energy levels ranging from ≈ 0.20 J to ≈ 0.46 J. On average the TVPDCU switching method reaches ≈ 0.02J higher levels. For unbalanced condition, both methods reach equally higher energy levels on healthy pole side of ≈ 0.32J to ≈ 0.89J, while the faulty pole energy levels remain an order of magnitude below the 0.2 J limit.

- **Delta-voltage implications:**
  - The switching method's one-order-of-magnitude larger ΔV (up to 263 V balanced, 69 V unbalanced) drives greater current ripple, potentially destabilizing the system and worsening EMC as well as causing stress on components and insulation materials.

  - Bender's tight ΔV (< 11.3 V balanced, < 3 V unbalanced) naturally contains current perturbations.

- **Time constants and time to measure**
  - Circuit theory (with identical IMD resistors) predicts a smaller τ for the pulse method.

  - When resistors are equalized, both methods share a theoretical value of $\tau \approx 0.77\,\mathrm{s}$.

  - Measured balanced condition data yields $\tau_{\text{pulse}} \approx 0.9\,\mathrm{s}$ and $\tau_{\text{switch}} \approx 0.7\,\mathrm{s}$, contradicting theoretical predictions.

  - Measured unbalanced condition data, both methods exhibit $\tau \approx 0.2\,\mathrm{s}$, closely matching theoretical values and implying similar measurement speeds in fault conditions.

- **Measurement-error sensitivity**
  Both the switching and pulse methods become less accurate when insulation resistance values are low or when the two measurement resistors are heavily unbalanced. The switching approach delivers very low error only when both resistors are high and closely matched, but error can spike dramatically if one leg dominates. By contrast, the pulse method tolerates a wider range of resistor values with only moderate error growth, only suffering large inaccuracies when both resistances fall into the lowest practical range. In practical terms, the pulse method offers more robust, predictable accuracy across normal operating conditions, while the switching method can achieve finer precision, but only under tightly controlled resistor tolerances.

Overall, while TVPDCU's switching method offers wider diagnostic headroom, it comes with higher pole-to-chassis voltages, higher touch current magnitudes, and more stringent EMC and accuracy requirements. The Bender pulse method, by contrast, delivers tighter voltage control and more predictable behavior, at the cost of reduced fault-diagnostic margin.

5.2 Implications

By describing and verifying the theory for state-of-the-art IRM, this report contributes by providing a well established knowledge base for further IRM development. Further, through identifying performance and evaluating the different parameters this report enables informed choices for future development. For practical applications and industry, the results allow stakeholders to make appropriate choices of IRM methods for their products.

5.3 Limitations

Ceramic capacitors, inherently voltage and temperature dependent, were utilized because of availability; however, electrolytic capacitors would likely provide superior performance due to their better electrical characteristics.

Recalculating measured time constants for the TVDPC is required for precise results because internal resistances inherent to the TVPDCU board still influence the circuit such that the methods are not compared on entirely equal terms. However, this was not performed for the time constants as the insignificant effect of such large resistor values in parallel configuration was deemed irrelevant for the sake of method comparison.

Time constant values were extracted from graphical data using Excel calculations and manual data cursors. This approach introduces human error into the analysis.

Minor measurement noise was present in laboratory tests, resulting in a consistent ripple in the recorded waveforms. This noise with a delta of approximately 400 mV complicated manual extraction of precise values.

CAN communication was not recorded during laboratory measurements. This means that we were limited in our knowledge of operating modes, calculated pole-to-chassis resistances, IRM warning signal thresholds and response time.

5.3.1 Validity

Resoldering of resistors on the TVPDCU improved the validity of the measurements by ensuring both systems were compared under similar conditions. Consequently, the measured results more accurately represent the intended parameters. In addition, the selected IRMUs are commonly employed in commercial applications and have a TRL (technical readiness level) of 9, making the comparison highly relevant and representative.

Corrected resistance test parameters measured with the TVPDCU were performed to compensate for the internal resistances inherent to the Volvo TVPDCU board, resulting in accurate pole-to-chassis resistance test parameters.

5.3.2 Reliability

All measurement equipment used throughout the study was calibrated, ensuring accurate and consistent results. The methods and measurements applied in this work are reproducible to a high degree, contributing to the overall reliability of the study. Furthermore, the procedure is clearly documented and transparent, facilitating replication.

The TVPDC-CU's SW had a bug in it, which caused a loss of data when measuring the TVDPC waveforms. It resulted in chopped corners towards the end of negative pole-to-chassis discharge and positive pole-to-chassis charge of the capacitance. This prohibited the acquisition of final steady-state values for these parts of the waveforms.

5.4 Future Research Directions

A future direction of research is to compare additional commercial IRMUs and widen the scope to include IRM technology from fields outside of automobile applications. This could include maritime or power systems area. To mitigate the high pole-to-chassis voltage in unbalanced conditions, research into IRM circuits with balancing capability may further improve safety by regulating voltage levels and minimizing resulting touch current magnitude.

5.5 Final Thoughts

This report bridges theoretical understanding and practical evaluation of insulation resistance monitoring (IRM) systems in high-voltage automotive applications. Through comparative analysis and empirical validation, the study contributes with a structured framework for assessing IRM performance under realistic conditions.

While limitations such as component selection and manual data processing affected some measurement precision, the methodology remains robust and the insights gained are valuable for both industry practitioners and academic researchers. The use of two widely adopted IRMUs ensures relevance and comparability, and the work provides a foundation that can be directly built upon in future investigations.

Ultimately, this study affirms the importance of detailed circuit understanding, methodical validation, and transparent documentation when evaluating safety-critical systems like IRM. It is hoped that these findings serve as a reliable reference point and motivate continued research on improving IRM technologies in automotive applications.

Bibliography

[1] Texas Instruments, *Automotive High-Voltage and Isolation Leakage Measurements Reference Design*, Texas Instruments, Feb. 2023, reference Design TIDA-01513, Rev. B. [Online]. Available: https://www.ti.com/lit/pdf/TIDUDJ6B

[2] J. Du, T. Q. Zheng, Y. Yan, H. Zhao, Y. Zeng, and H. Li, “Insulation monitoring method for dc systems with ground capacitance in electric vehicles,” *Applied Sciences*, vol. 9, no. 13, p. 2607, June 2019.

[3] Texas Instruments, *AFE for Insulation Monitoring in High-Voltage EV Charging and Solar Energy Reference Design*, Texas Instruments, Jun. 2023, reference Design TIDA-010232, Rev. C. [Online]. Available: https://www.ti.com/lit/pdf/TIDUEZ8C

[4] C. Song, Y. Shao, S. Song, S. Peng, F. Zhou, C. Chang, and D. Wang, “Insulation resistance monitoring algorithm for battery pack in electric vehicle based on extended kalman filtering,” *Energies*, vol. 10, no. 5, p. 714, May 2017.

[5] J. Li, Z. Wu, Y. Fan, Y. Wang, and J. Jiang, “Research on insulation resistance on-line monitoring for electric vehicle,” in *2007 International Conference on Electrical Machines and Systems (ICEMS)*. Beijing, China: IEEE, 2007, pp. 813–817.

[6] Z. Chen, W. Cui, X. Cui, H. Qiao, H. Lu, and N. Qiu, “A new method of insulation detection on electric vehicles based on a variable forgetting factor recursive least squares algorithm,” *IEEE Access*, vol. 9, pp. 73 590–73 607, 2021.

[7] CSM GmbH. (2024) Hv ad ecat measurement modules – high-voltage measurement up to 1000 v. CSM GmbH. Accessed: 2025-05-09. [Online]. Available: https://www.csm.de/en/products/high-voltage-measurement-modules/hv-ad-measurement-modules/hv-ad-ecat-1000-v

[8] ——. (2024) Hv breakout modules – 1-channel measurement modules for high-voltage applications. CSM GmbH. Accessed: 2025-05-09. [Online]. Available: https://www.csm.de/en/products/hv-breakout-modules/hv-breakout-modules-1-x

[9] Elektro-Automatik. (2024) Ea-ps 10000 4u programmable dc laboratory power supply – 0...1500 v / 0...60 a. Elektro-Automatik. Accessed: 2025-05-09. [Online]. Available: https://elektroautomatik.com/shop/en/products/programmable-dc-laboratory-power-supplies/dc-laboratory-power-supplies/series-ps-10000-4u-30-kw/1055/lab-power-supply-0...1500-v/0...60-a

A

Appendix 1

A.0.1 Pulse method derivation

KCL yields:

$$\begin{aligned} I_f^+ &= I_1 + I_2, \\ I_f^+ &= I_3 + I_4. \end{aligned} \tag{A.1}$$

$$U_f^+ = R_f \, I_f^+ \tag{A.2}$$

KVL in the $R_1 - R_2$ branch gives:

$$U = R\,(I_1 - I_2). \tag{A.3}$$

KVL in the battery branch (Loop 1) gives:

$$U = R_n I_4 - R_p I_3 \tag{A.4}$$

KVL in the signal branch gives:

$$U_s^+ = R_p I_3 + R_1 I_1 + R_f I_f^+ \tag{A.5}$$

Solves for I_1 and I_2:
from equation x and x (1 and 2?), we have:

$$\begin{cases} I_1 + I_2 = I_f^+, \\ I_1 - I_2 = \dfrac{U}{R}. \end{cases} \tag{A.6}$$

This gives us:

$$\begin{cases} I_1 &= \frac{I_f^+}{2} + \frac{U}{2R}, \\ I_2 &= \frac{I_f^+}{2} + \frac{U}{2R}. \end{cases} \tag{A.7}$$

Solve for I_3 and I_4:
Starting with (A.4):

$$U = R_n \, I_4 - R_p \, I_3 \quad \Longrightarrow \quad I_4 = \frac{U + R_p \, I_3}{R_n} \tag{A.8}$$

Using the KCL expression (B.1):

$$I_f^+ = I_3 + \frac{U + R_p\, I_3}{R_n} = I_3 \left(1 + \frac{R_p}{R_n}\right) + \frac{U}{R_n}. \tag{A.9}$$

Solving for I_3 yields:

$$I_3 = \frac{I_f^+ - \dfrac{U}{R_n}}{1 + \dfrac{R_p}{R_n}} = \frac{R_n\, I_f^+ - U}{R_n + R_p}. \tag{A.10}$$

Substitute I_1 and I_3 into the signal branch KVL.
Substitute (A.7) and (A.10) into (A.5):

$$\begin{aligned} U_s^+ &= R_p\, I_3 + R\, I_1 + R_f\, I_f^+ \\ &= R_p\, \frac{R_n\, I_f^+ - U}{R_n + R_p} + R\left(\frac{I_f^+}{2} + \frac{U}{2R}\right) + R_f\, I_f^+ \\ &= \frac{R_p R_n}{R_n + R_p}\, I_f^+ - \frac{R_p\, U}{R_n + R_p} + \frac{R\, I_f^+}{2} + \frac{U}{2} + R_f\, I_f^+. \end{aligned}$$

Regrouping the terms, factoring out I_f^+ yields :

$$U_s^+ = I_f^+ \left[\frac{R_p R_n}{R_n + R_p} + \frac{R}{2} + R_f\right] + \left[\frac{U}{2} - \frac{R_p\, U}{R_n + R_p}\right]. \tag{A.11}$$

To solve for I_f^+ and U_f^+, we first rearrange (A.11) to isolate I_f^+:

$$I_f^+ = \frac{U_s^+ - \left[\dfrac{U}{2} - \dfrac{R_p\, U}{R_n + R_p}\right]}{\dfrac{R_p R_n}{R_n + R_p} + \dfrac{R}{2} + R_f}. \tag{A.12}$$

It is convenient to eliminate the division by $R_n + R_p$ in the numerator:

$$U_s^+ - \left[\frac{U}{2} - \frac{R_p\, U}{R_n + R_p}\right] = \frac{(R_n + R_p)\left(U_s^+ - \frac{U}{2}\right) + R_p\, U}{R_n + R_p}, \tag{A.13}$$

we obtain:

$$I_f^+ = \frac{(R_n + R_p)\left(U_s^+ - \frac{U}{2}\right) + R_p\, U}{(R_n + R_p)\left(R_f + \frac{R}{2}\right) + R_p\, R_n}. \tag{A.14}$$

Since the sampling voltage is given by:

$$U_f^+ = R_f\, I_f^+, \tag{A.15}$$

We finally obtain the expression for the measured reflected voltage at the positive half-period:

$$U_f^+ = \frac{R_f\left[(R_n + R_p)\left(U_s^+ - \frac{U}{2}\right) + R_p\, U\right]}{(R_n + R_p)\left(R_f + \frac{R}{2}\right) + R_p\, R_n}. \tag{A.16}$$

To obtain the expression for computing R_p, we must derive expressions valid for the negative half-cycle period in a similar way. Now the injected signal is U_s^- and the corresponding measured sampling voltage is U_f^-.

$$U_f^- = \frac{R_f \left[(R_n + R_p)\left(U_s^- - \frac{U}{2}\right) + R_p\, U\right]}{((R_n + R_p)\left(R_f + \frac{R}{2}\right) + R_p\, R_n}. \tag{A.17}$$

Because the denominators in expressions for U_f^+ and U_f^- are identical, subtracting (A.17) from (A.16) yields:

$$U_f^+ - U_f^- = \frac{R_f\,(R_n + R_p)\,(U_s^+ - U_s^-)}{(R_n + R_p)\left(R_f + \frac{R}{2}\right) + R_p\, R_n}. \tag{A.18}$$

Rearranging,

$$(R_n + R_p)\left(R_f + \frac{R}{2}\right) + R_p\, R_n = \frac{R_f\,(R_n + R_p)\,(U_s^+ - U_s^-)}{U_f^+ - U_f^-}. \tag{A.19}$$

Dividing both sides by $R_n + R_p$ yields:

$$R_f + \frac{R}{2} + \frac{R_p\, R_n}{R_n + R_p} = \frac{R_f\,(U_s^+ - U_s^-)}{U_f^+ - U_f^-}. \tag{A.20}$$

Defining

$$X = \frac{R_f\,(U_s^+ - U_s^-)}{U_f^+ - U_f^-} - \left(R_f + \frac{R}{2}\right). \tag{A.21}$$

Then, based on equation A.20:

$$X = \frac{R_p\, R_n}{R_n + R_p}. \tag{A.22}$$

Solving for R_n yields:

$$R_n = \frac{X\, R_p}{R_p - X}. \tag{A.23}$$

Because that in many practical applications the resistance R_n is not known, we seek an expression for R_p in terms of only measured and known quantities. Based on the derived expression for the sampling voltage in the positive half-cycle:

$$U_f^+ = \frac{R_f \left[(R_n + R_p)\left(U_s^+ - \frac{U}{2}\right) + R_p\, U\right]}{(R_n + R_p)\left(R_f + \frac{R}{2}\right) + R_p\, R_n}. \tag{A.24}$$

After eliminating R_n by combining A.23 and A.24, solving for R_p yields:

$$R_p = \frac{U\left[\dfrac{R_f\,(U_s^+ - U_s^-)}{U_f^+ - U_f^-} - \left(R_f + \frac{R}{2}\right)\right]}{\left(U_s^+ + \frac{U}{2}\right) - \dfrac{U_f^+\,(U_s^+ - U_s^-)}{U_f^+ - U_f^-}}. \tag{A.25}$$

Finally, a similar approach but instead solving for R_n, yields:

$$R_n = \frac{U\left[\frac{R_f\left(U_s^+ - U_s^-\right)}{U_f^+ - U_f^-} - \left(R_f + \frac{R}{2}\right)\right]}{\frac{U_f^+\left(U_s^+ - U_s^-\right)}{U_f^+ - U_f^-} - \left(U_s^+ - \frac{U}{2}\right)}. \tag{A.26}$$

B

Appendix 3

B.0.1 Derivation of Y-capacitance, equivalent resistance and resistor capacitance time constant

To analyze the circuit, the equations previously used to derive the circuit are now applied again regarding the capacitance, but the formulas are set in the s-domain.

$$I_f^+(s) = I_1(s) + I_2(s), I_f^+(s) = I_3(s) + I_4(s).$$

$$U(s) = \frac{R_n\Big[I_4(s) + C_n U_{n0}\Big]}{1 + sC_n R_n} - \frac{R_p\Big[I_3(s) + C_p U_{p0}\Big]}{1 + sC_p R_p} \tag{B.1}$$

$$U(s) = R_1 I_1(s) - R_2 I_2(s) \tag{B.2}$$

$$U_s(s) = \frac{R_p\Big[I_3(s) + C_p U_{p0}\Big]}{1 + sC_p R_p} + R_1 I_1(s) + R_f I_f(s) \tag{B.3}$$

To make the circuit clearer, we assume $R_1 = R_2 = R$.

When the step pulse is sent with an amplitude U_s, the voltage of the sample resistor U_f is influenced by the elements in the circuit.
To analyze the step response of the circuit, Kirchoff is being used and by transforming the circuit into the Laplace domain. This ends up in the equation:

$$U_f(s) = \frac{a_1}{s} + \frac{a_2}{s + \dfrac{1}{a_3}} \tag{B.4}$$

where:

- a_1 is the steady-state component,
- a_2 is the transient gain, and
- a_3 is the effective time constant.

If we then take the inverse laplace tranform of the expression, it results in:

$$U_f(t) = a_1 + a_2 \exp\left(-\frac{t}{a_3}\right) \tag{B.5}$$

B.0.1.1 Laplace derivation for $U_f(s)$

$$\mathcal{L}^{-1}\left\{\frac{1}{s}\right\} = 1, \quad \mathcal{L}^{-1}\left\{\frac{1}{s+\frac{1}{a_3}}\right\} = e^{-\frac{t}{a_3}} \tag{B.6}$$

using inverse Laplace step by step gives:

$$\mathcal{L}^{-1}\{U_f(s)\} = a_1\,\mathcal{L}^{-1}\left\{\frac{1}{s}\right\} + a_2\,\mathcal{L}^{-1}\left\{\frac{1}{s+\frac{1}{a_3}}\right\} = a_1 + a_2\,e^{-\frac{t}{a_3}}$$

Thus, the time domain for the reflected wave voltage is:

$$U_f(t) = a_1 + a_2 \exp\left(-\frac{t}{a_3}\right) \tag{B.7}$$

Solving for a_1 and a_3 yields in the expressions:

$$a_1 = \frac{R_f\Big[U(R_p - R_n) + 2U_s(R_p + R_n)\Big]}{(R_p + R_n)(R + 2R_f) + 2R_pR_n} \tag{B.8}$$

$$a_3 = \frac{(C_p + C_n)\,R_pR_n(R + 2R_f)}{(R_p + R_n)(R + 2R_f) + R_pR_n} \tag{B.9}$$

B.0.1.2 Equivalent Y Capacitance

Since the equivalent Y capacitance is defined as the parallel combination of C_p and C_n, we have:

$$C_p \parallel C_n = C_p + C_n \tag{B.10}$$

Starting from equation B.9, we solve for $C_p + C_n$ as follows:
Multiply both sides of B.9 by the denominator:

$$a_3\Big[(R_p + R_n)(R + 2R_f) + 2R_pR_n\Big] = (C_p + C_n)\,R_pR_n(R + 2R_f) \tag{B.11}$$

Dividing both sides by $R_pR_n(R + 2R_f)$ yields:

$$C_p + C_n = \frac{a_3\Big[(R_p + R_n)(R + 2R_f) + 2R_pR_n\Big]}{R_pR_n(R + 2R_f)} \tag{B.12}$$

Thus, the equivalent Y capacitance is given by:

$$C_p \parallel C_n = \frac{a_3(R_p + R_n)(R + 2R_f) + 2R_pR_n}{R_pR_n(R + 2R_f)}. \tag{B.13}$$

The response time constant a_3 relates to the RC time constant of the equivalent network, where the effective capacitance is the parallel combination $C_p \parallel C_n$. In a standard RC circuit, the time constant is given by

$$\tau = R_{\text{eq}}\,C_{\text{eq}}.$$

Identifying $\tau = a_3$ and after appropriate network analysis (combining the effects of R_p, R_n, R, and R_f), we obtain

$$C_p \parallel C_n = \frac{a_3(R_p + R_n)(R + 2R_f) + 2R_pR_n}{R_pR_n(R + 2R_f)}. \tag{B.14}$$

B.0.1.2.1 Applying the superposition principle to determine system response and equivalent resistance

In order to further understand and the circuit theory and the derivation of the RC time constant, the superposition principle can be applied. This fundamental concept states that the response of a linear system in any circuit element is the sum of the responses resulting from each independent source. Thus, when considering one source, all other sources are turned off by short-circuiting voltage sources and replacing current sources with open circuits.

In the pulsed method circuit shown in figure B.1 we can identify two sources, namely the HVDC battery energy storage system U_{ESS} and the voltage square wave generator U_s.

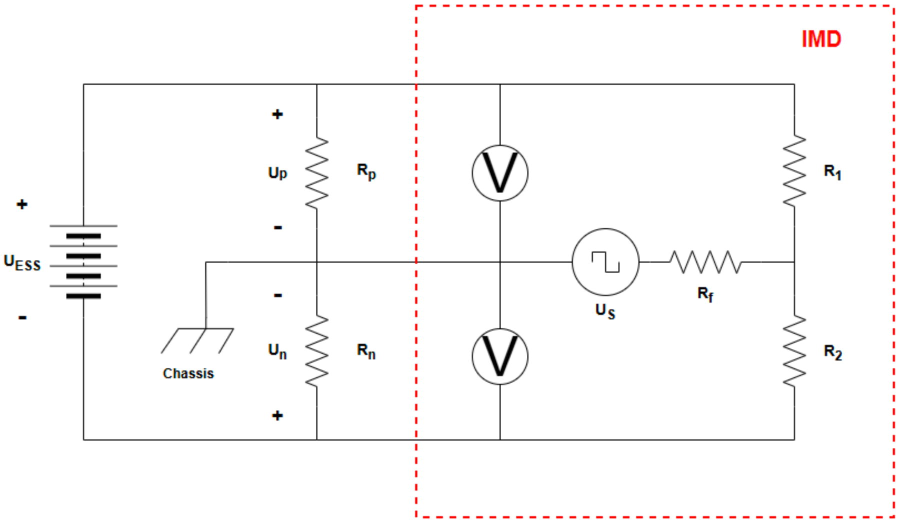

Figure B.1: Pulse IMD Circuit.

Applying the superposition principle will yield two circuits. With these circuits, we can derive the expressions for the steady-state voltage response and obtain the equivalent resistance needed to compute the RC time constant τ.

We begin by short-circuiting the square wave generator voltage source and obtain the circuit shown in figure B.2.

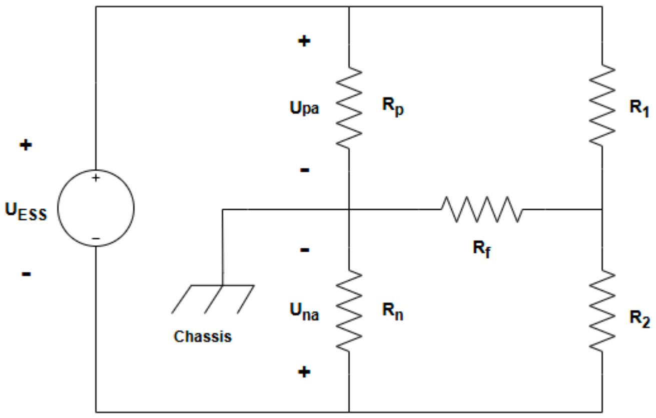

Figure B.2: Square wave generator short-circuited to analyze system response to battery source.

The voltage over the equivalent pole to chassis resistances are given by voltage division:

$$U_{pa} = U_{ESS}\frac{R_p}{R_pR_n} \tag{B.15}$$

$$U_{na} = -U_{ESS}\frac{R_n}{R_nR_p} \tag{B.16}$$

Which in a balanced system yields:

$$U_{pa} = \frac{U_{ESS}}{2} \tag{B.17}$$

$$U_{pn} = -\frac{U_{ESS}}{2} \tag{B.18}$$

Then, instead by short-circuiting the battery source U_{ESS} and obtain the circuit shown in figure B.3

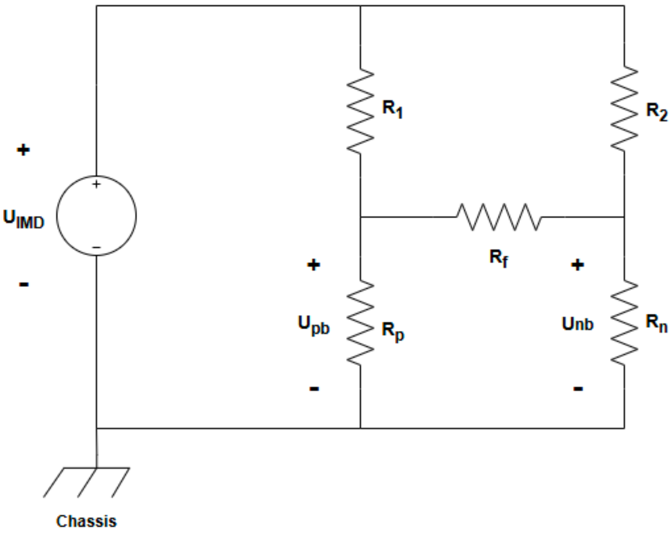

Figure B.3: Battery source short-circuited to analyze system response to square wave voltage source.

We establish $R = R_1 = R_2$ and recognize that the sampling resistor R_f is much smaller than other resistance values in the circuit. Thus, we assume $R_f \to 0$ to further simplify expressions. Circuit analysis yields expressions for U_{pb} and U_{nb}:

$$U_{pb} = U_{IMD} \frac{\frac{R_p R_n}{R_p + R_n}}{\frac{R_p R_n}{R_p + R_n} + \frac{R}{2}}. \tag{B.19}$$

which for a balanced system yields:

$$U_{pb} = U_{nb} = U_{IMD} \frac{\frac{R_p R_n}{R_p + R_n}}{\frac{R_p R_n}{R_p + R_n} + \frac{R}{2}}. \tag{B.20}$$

Thus, when considering the square wave half-cycle sign change, the total response of the system at R_p is:

$$U_p^{max} = U_{pb} + U_{pa} = U_{IMD} \frac{\frac{R_p R_n}{R_p + R_n}}{\frac{R_p R_n}{R_p + R_n} + \frac{R}{2}} + U_{ESS} \frac{R_p}{R_p R_n}. \tag{B.21}$$

$$U_p^{min} = -U_{pb} + U_{pa} = -U_{IMD} \frac{\frac{R_p R_n}{R_p + R_n}}{\frac{R_p R_n}{R_p + R_n} + \frac{R}{2}} + U_{ESS} \frac{R_p}{R_p R_n}. \tag{B.22}$$

and at R_n:

$$U_n^{max} = U_{nb} + U_{na} = U_{IMD} \frac{\frac{R_p R_n}{R_p + R_n}}{\frac{R_p R_n}{R_p + R_n} + \frac{R}{2}} - U_{ESS} \frac{R_p}{R_p R_n}. \tag{B.23}$$

$$U_n^{min} = U_{nb} + U_{na} = -U_{IMD} \frac{\frac{R_p R_n}{R_p + R_n}}{\frac{R_p R_n}{R_p + R_n} + \frac{R}{2}} - U_{ESS} \frac{R_p}{R_p R_n}. \tag{B.24}$$

B.0.1.2.2 Equivalent resistance The equivalent resistance of the RC circuit is needed to determine the RC time constant of the circuit. By short circuiting both sources, as shown in figure B.4, we can determine the equivalent resistance between the common node of connection and the chassis ground reference.

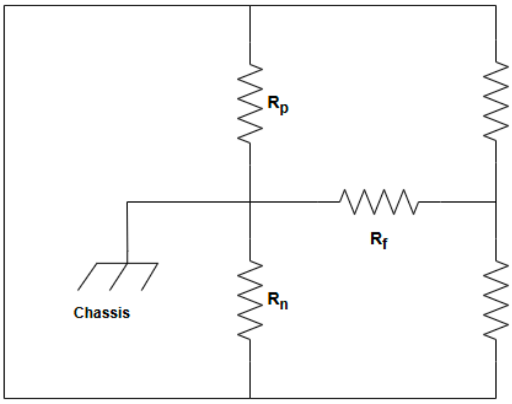

Figure B.4: Both voltage sources short-circuited to analyze equivalent resistance between common node and chassis.

Once again, we establish $R = R_1 = R_2$ and observe that the circuit simplifies to three parallel branches from a common node to chassis:

1. A direct resistor R_p.
2. Another direct resistor R_n.
3. A path through R_1 in parallel with R_2 and then through R_f to the chassis.

Combining these branches yields the following:

$$R_{eqv} = R_p \parallel \frac{R}{2} + R_f \parallel R_n = \frac{\left(\frac{R_p \left(\frac{R}{2} + R_f \right)}{R_p + \left(\frac{R}{2} + R_f \right)} \right) R_n}{\frac{R_p \left(\frac{R}{2} + R_f \right)}{R_p + \left(\frac{R}{2} + R_f \right)} + R_n}. \tag{B.25}$$

which simplifies to:

$$R_{\text{eqv}} = \frac{R_p R_n (R + 2R_f)}{(R_p + R_n)(R + 2R_f) + 2R_p R_n}. \tag{B.26}$$

B.0.1.2.3 Determining stray capacitance and RC time constant All physical elements of the HVDC system contribute with an inherent stray capacitance between positive and negative poles and the chassis, respectively. This stray capacitance of the system is represented by two equivalent Y-capacitors C_p and C_n between the positive and negative poles and the chassis. The equivalent capacitance of the system is thus:

$$C_{eqv} = C_p \parallel C_n = C_p + C_n \tag{B.27}$$

The time constant τ, of a first-order RC circuit is given by

$$\tau = R_{eqv}\, C_{eqv} = \frac{R_p R_n (R + 2R_f)}{(R_p + R_n)(R + 2R_f) + 2R_p R_n}(C_p + C_n) \tag{B.28}$$

The step-response follows an exponential behavior when the capacitor charges and discharges. The step response when charging will follow:

$$U(t) = U_p^{max} + (U(o) - U_p^{max})e^{-\frac{t}{\tau}} \tag{B.29}$$

where $U(0)$ is the initial voltage and U_p^{max} is the final steady state voltage. After one time constant, that is when $t = \tau$, the voltage will have changed by 63.2% of the difference between initial and final value, and thus dictates how fast the voltage can change and the time to measure of the system.

Conversely, when discharging the expression will be:

$$U(t) = U(0)e^{-\frac{t}{\tau}} \tag{B.30}$$

When discharging the capacitance, at $t = \tau$ the voltage will have dropped to about 36.8% of the initial value.

C

Appendix 4

To analyze the circuit, KCL, KVL and Ohm's law are applied:

$$I_N = I_P \rightarrow \frac{V_N}{R_N} = \frac{V_P}{R_P} \tag{C.1}$$

C.0.0.1 Determining equivalent negative pole-to-chassis insulation resistance: R_N

A known reference resistor R_{Ref} is connected in series with a switch between the HVDC positive pole and chassis ground (figure C.1). The isolation is broken as a result, but by choosing a large R_{Ref} resistor value the current magnitude is limited. When the switch is closed R_{Ref} will connect in parallel to the equivalent resistance between positive pole and chassis, R_P. The voltage across this, V_P' is measured and used to analyze by applying KCL.

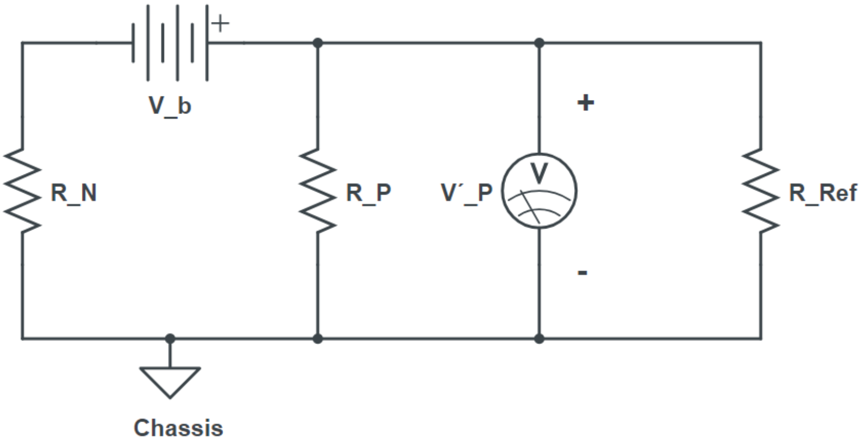

Figure C.1: Circuit for determining insulation resistance of negative pole-to-chassis: R_N.

KCL yields:

$$\frac{V_b - V_P'}{R_N} = \frac{V_P'}{R_P} + \frac{V_P'}{R_{Ref}} \tag{C.2}$$

substitute $V_b = V_N + V_P$ and $R_P = R_N \left(\frac{V_P}{V_N}\right)$:

$$\frac{(V_N + V_P) - V_P'}{R_N} = \frac{V_P'}{R_P} + \frac{V_P'}{R_{Ref}} \tag{C.3}$$

expanding R_P,

$$\frac{(V_N + V_P) - V'_P}{R_N} = \frac{V'_P}{R_P} + \frac{V'_P}{R_{Ref}} \tag{C.4}$$

$$= \frac{V'_P(V_N/V_P)}{R_N} + \frac{V'_P}{R_{Ref}} \tag{C.5}$$

From the previous equation:

$$\frac{(V_N + V_P) - V'_P}{R_N} = \frac{V'_P(V_N/V_P)}{R_N} + \frac{V'_P}{R_{Ref}} \tag{C.6}$$

Grouping terms that include R_N:

$$\frac{(V_N + V_P) - V'_P - V'_P(V_N/V_P)}{R_N} = \frac{V'_P}{R_{Ref}} \tag{C.7}$$

rearranging,

$$R_N = \frac{R_{Ref}}{V'_P}((V_N + V_P) - V'_P - V'_P(\frac{V_N}{V_P})). \tag{C.8}$$

This simplifies to:

$$R_N = \frac{R_{Ref}}{V'_P}\left(1 + \frac{V_N}{V_P}\right)(V_P - V'_P) \tag{C.9}$$

C.0.0.2 Determining equivalent positive pole-to-chassis insulation resistance: R_P

For determining the equivalent resistance between positive pole and chassis, the procedure remains similar. But in this case we aim to determine R_P. To achieve this a known large resistance R_{Ref} is connected between the battery and the chassis ground, in parallel with R_N (see figure C.2). Then the circuit analysis is initiated by applying KCL based on the measured voltages.

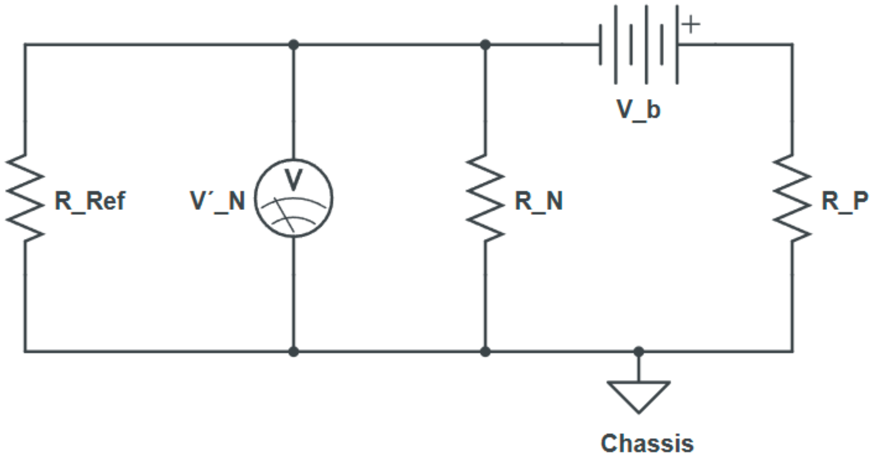

Figure C.2: Circuit for determining insulation resistance of positive pole-to-chassis: R_P.

KCL:

$$\frac{V_b + V_N'}{R_P} = \frac{V_N'}{R_N} + \frac{V_N'}{R_{Ref}} \tag{C.10}$$

Substitute $V_b = V_N + V_P$ and $R_N = R_P\left(\frac{V_N}{V_P}\right)$:

$$\frac{V_N + V_P - V_N'}{R_P} = \frac{V_N'(V_P/V_N)}{R_P} + \frac{V_N'}{R_{Ref}} \tag{C.11}$$

From the previous equation:

$$\frac{V_N + V_P - V_N'}{R_P} = \frac{V_N'(V_P/V_N)}{R_P} + \frac{V_N'}{R_{Ref}} \tag{C.12}$$

Grouping terms that include R_P:

$$\frac{V_N + V_P - V_N' - V_N'(V_P/V_N)}{R_P} = \frac{V_N'}{R_{Ref}} \tag{C.13}$$

Rearranging,

$$R_P = \frac{R_{Ref}}{V_N'}(V_N + V_P - V_N' - V_N'(V_P/V_N)). \tag{C.14}$$

This simplifies to:

$$R_P = \frac{R_{Ref}}{V_N'}\left(1 + \frac{V_P}{V_N}\right)(V_N - V_N') \tag{C.15}$$

D

Appendix 5

D.1 All recorded voltage waveforms

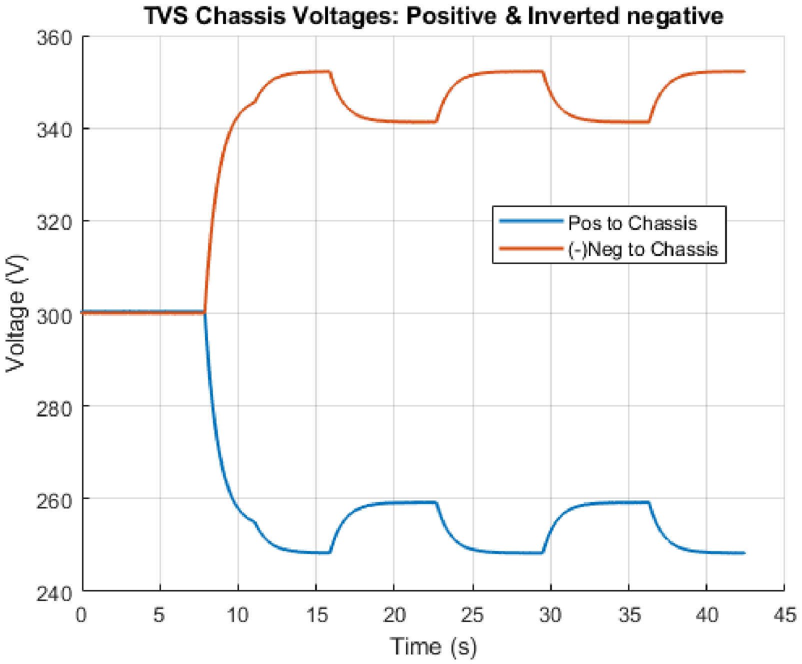

Figure D.1: Bender Balanced 600V

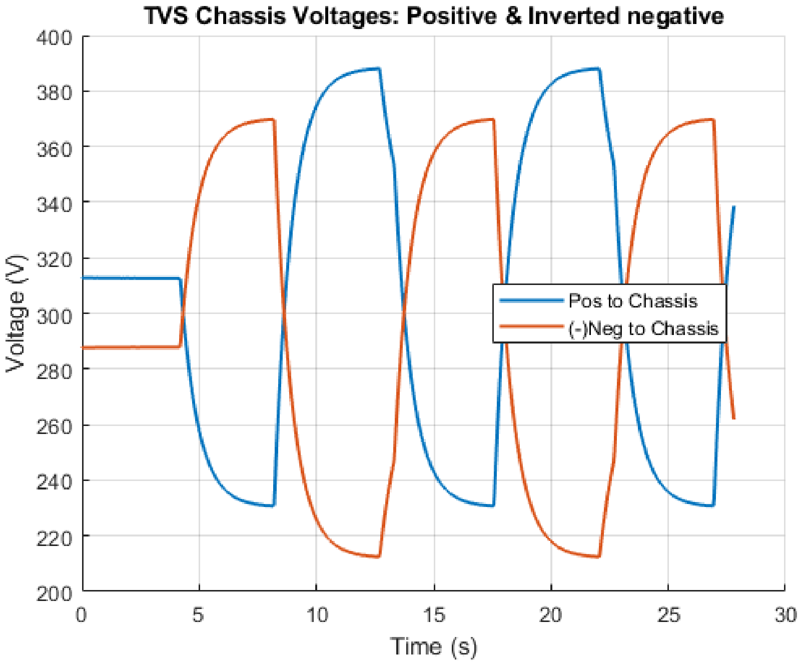

Figure D.2: TVPDC Balanced 600V

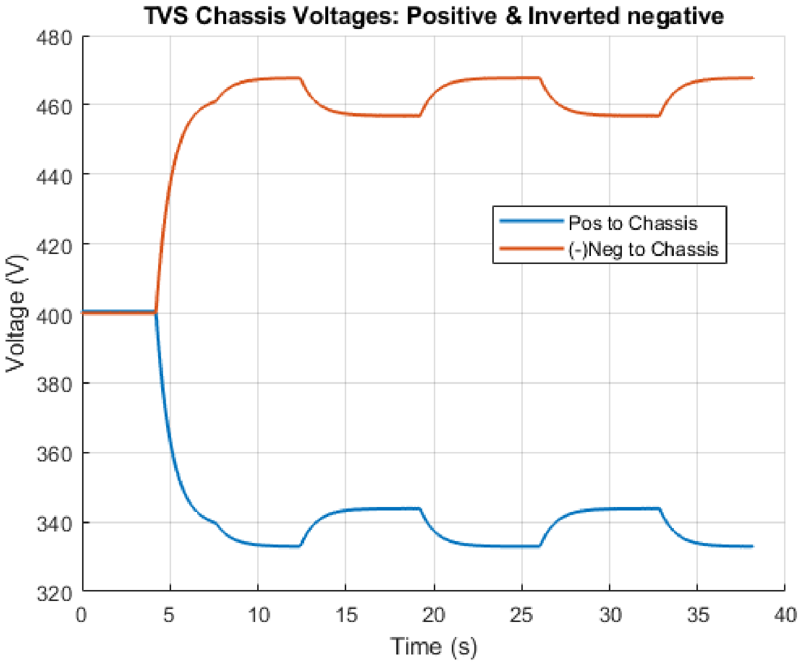

Figure D.3: Bender Balanced 800V

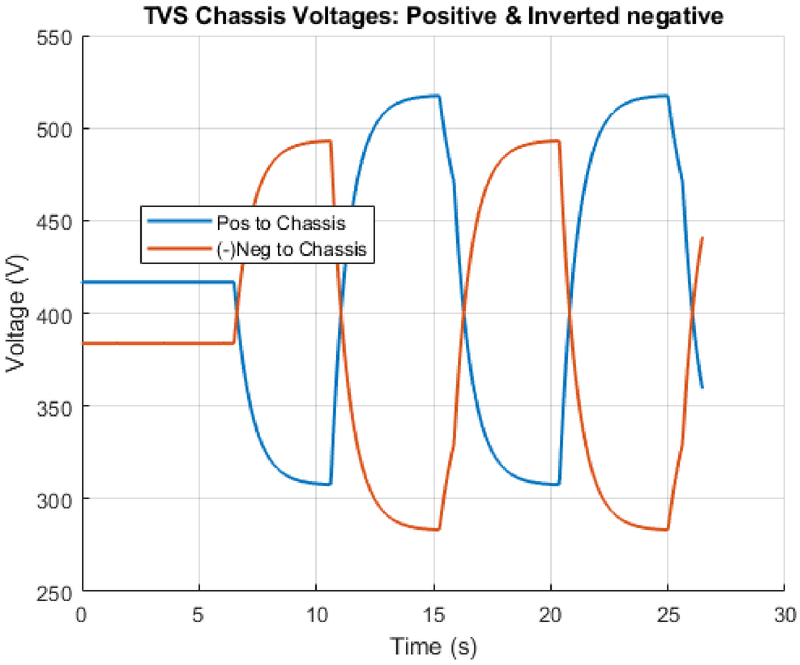

Figure D.4: TVPDC Balanced 800V

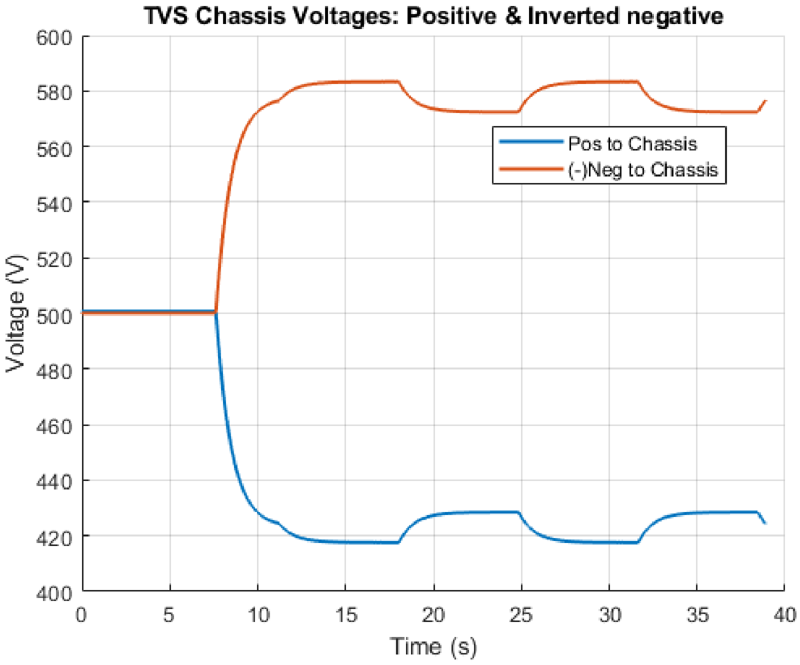

Figure D.5: Bender Balanced 1000V

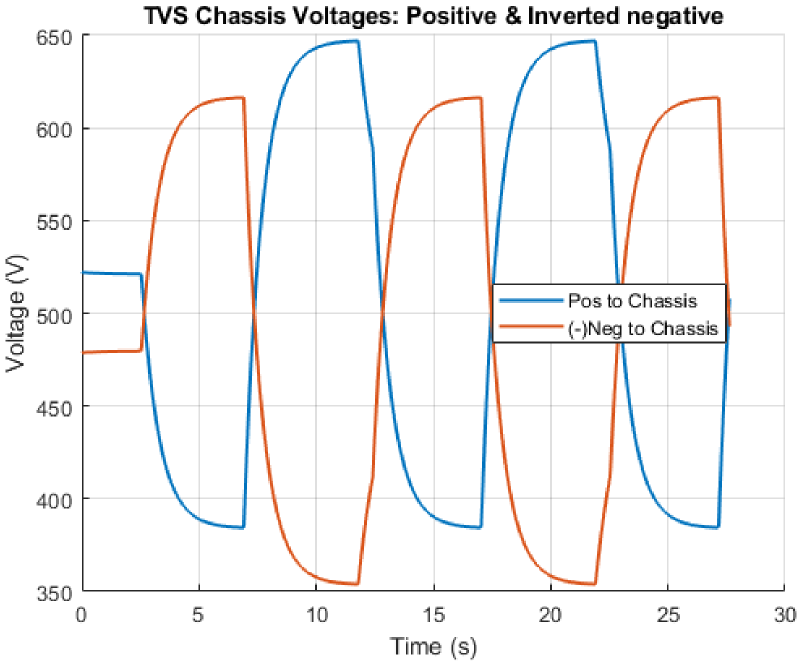

Figure D.6: TVPDC Balanced 1000V

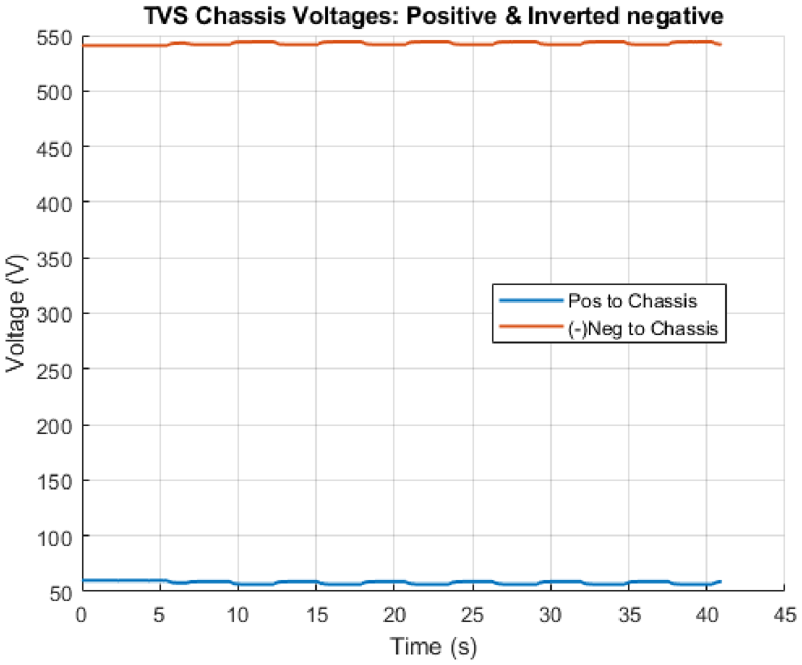

Figure D.7: Bender Unbalanced: R_n=1MΩ, R_p=100kΩ, 600V

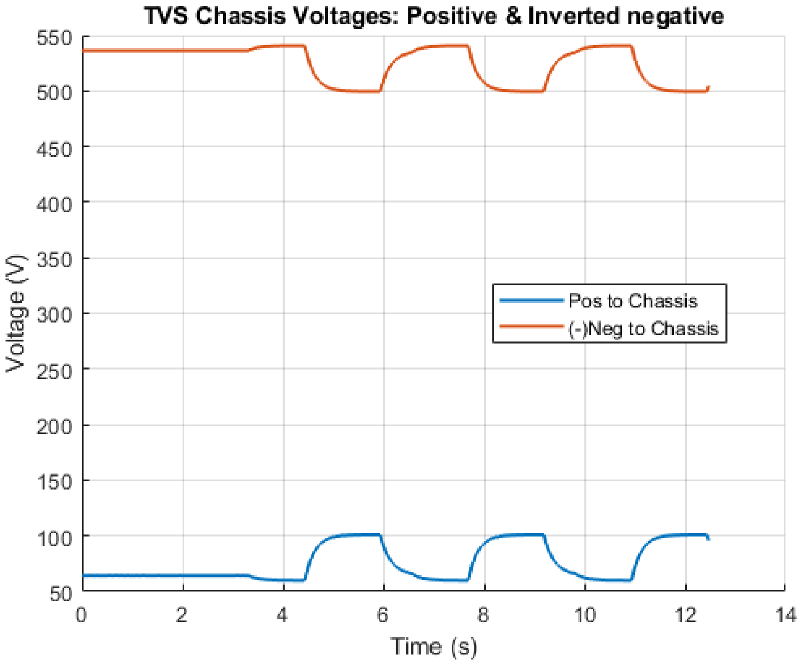

Figure D.8: TVPDC Unbalanced: R_n=1MΩ, R_p=100kΩ, 600V

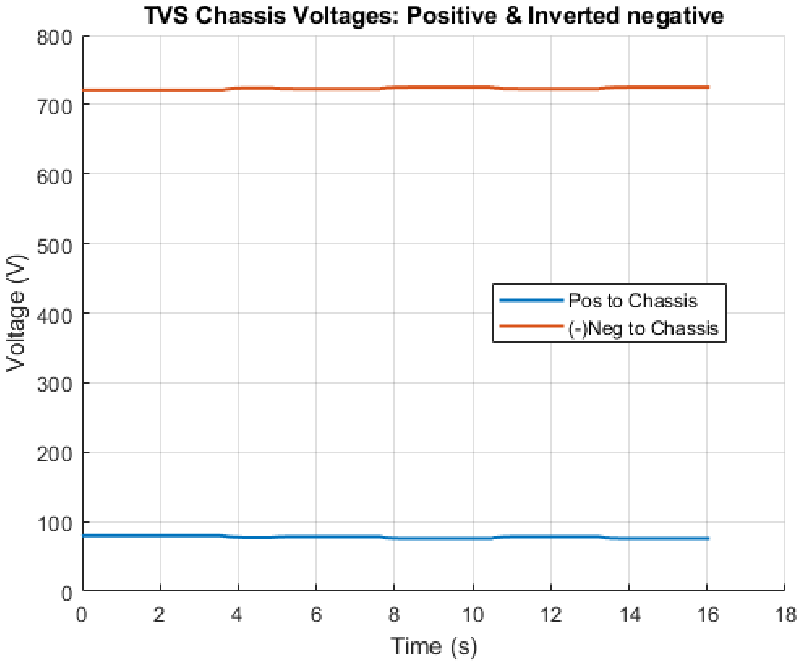

Figure D.9: Bender Unbalanced: R_n=1MΩ, R_p=100kΩ, 800V

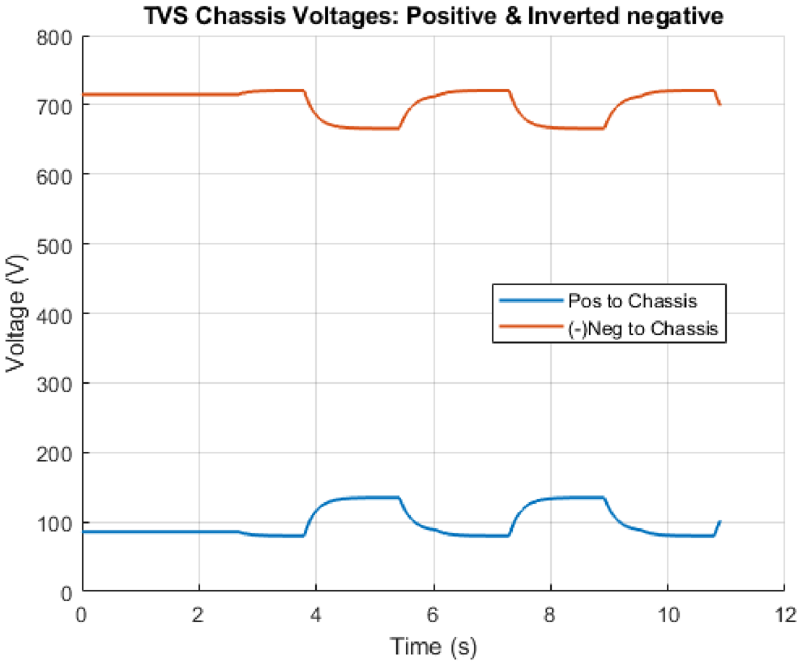

Figure D.10: TVPDC Unbalanced: R_n=1MΩ, R_p=100kΩ, 800V

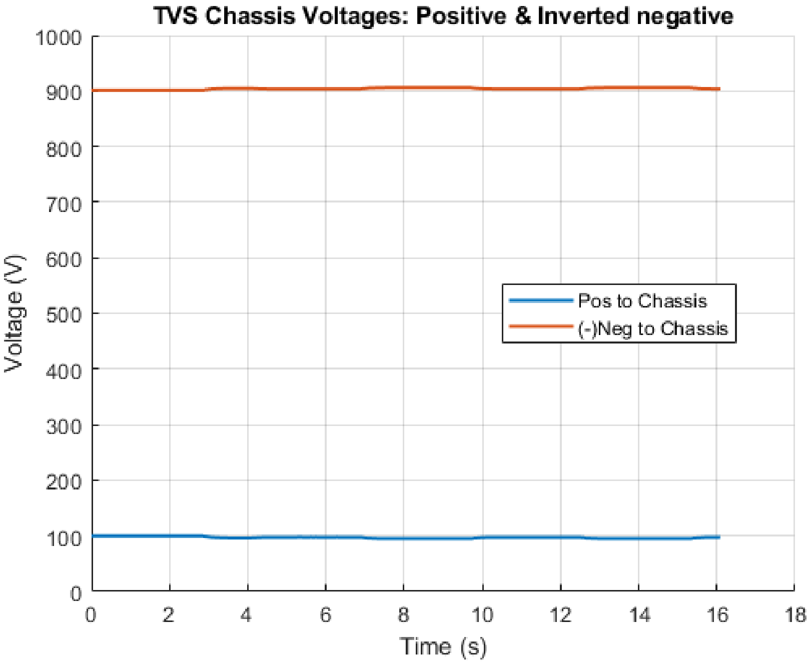

Figure D.11: Bender Unbalanced: R_n=1MΩ, R_p=100kΩ, 1000V

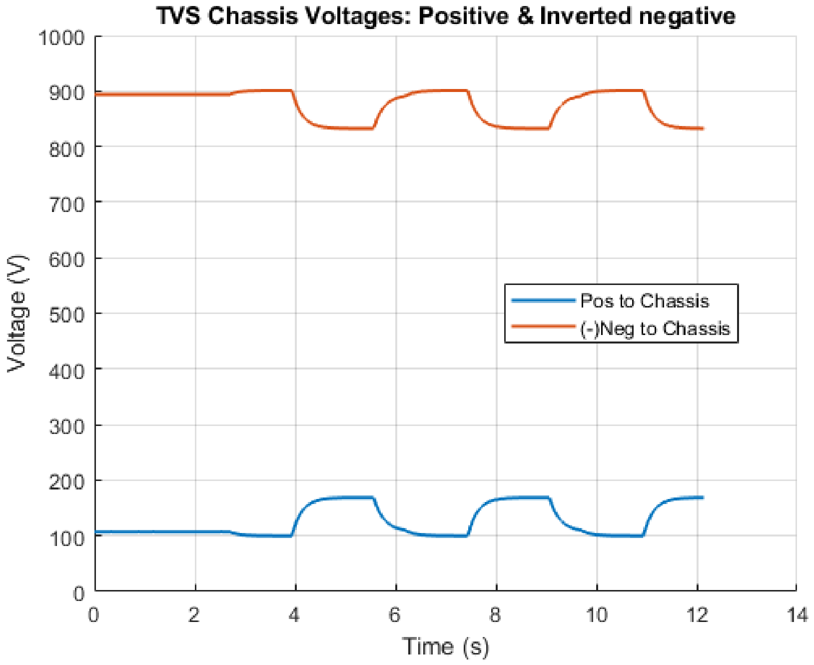

Figure D.12: TVPDC Unbalanced: R_n=1MΩ, R_p=100kΩ, 1000V

E

Appendix 6

E.1 All simulated body current graphs

Balanced cases :

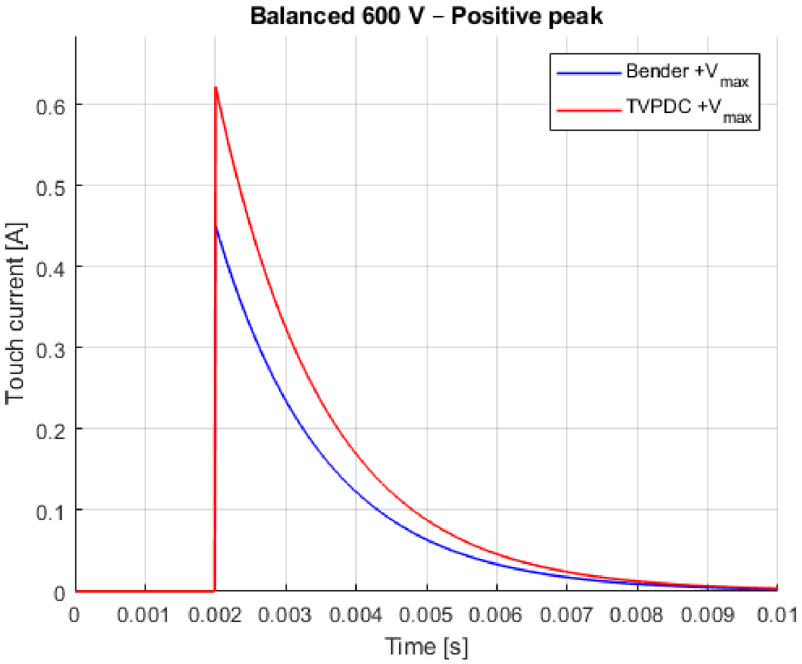

Figure E.1: Balanced 600V positive peak

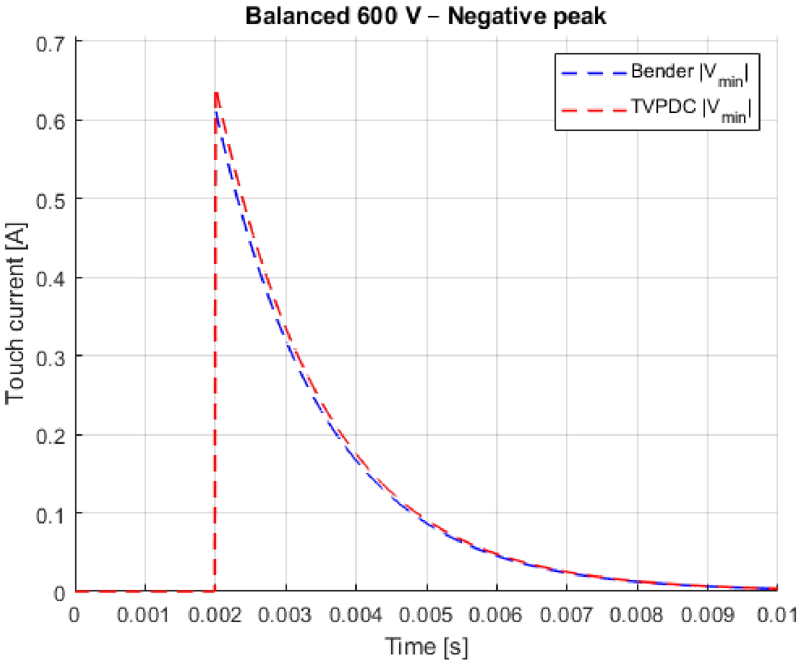

Figure E.2: Balanced 600V negative peak

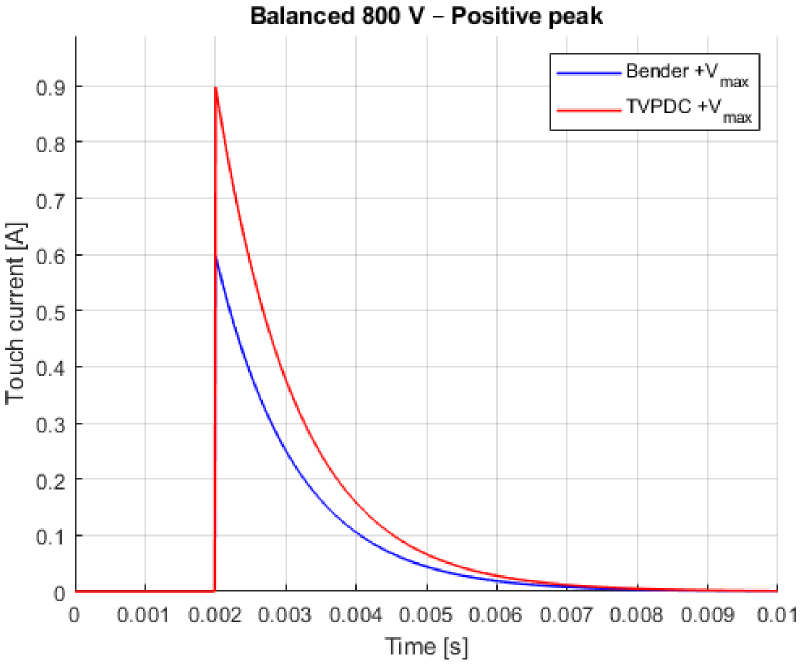

Figure E.3: Balanced 800V positive peak

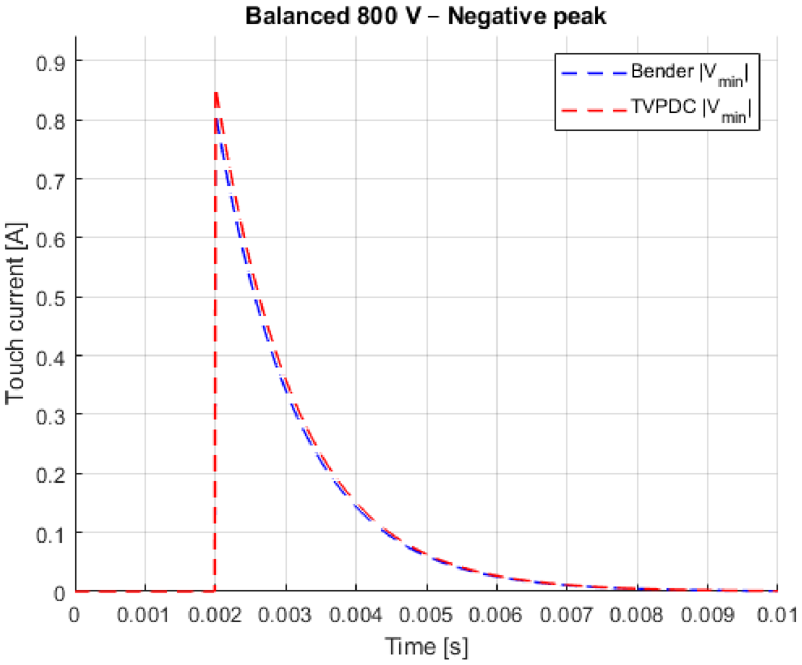

Figure E.4: Balanced 800V negative peak

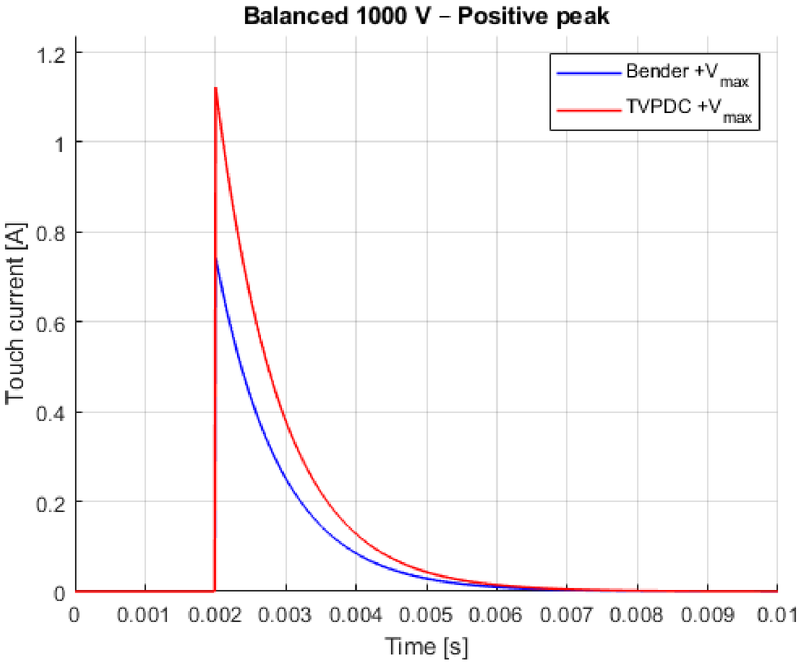

Figure E.5: Balanced 1000V positive peak

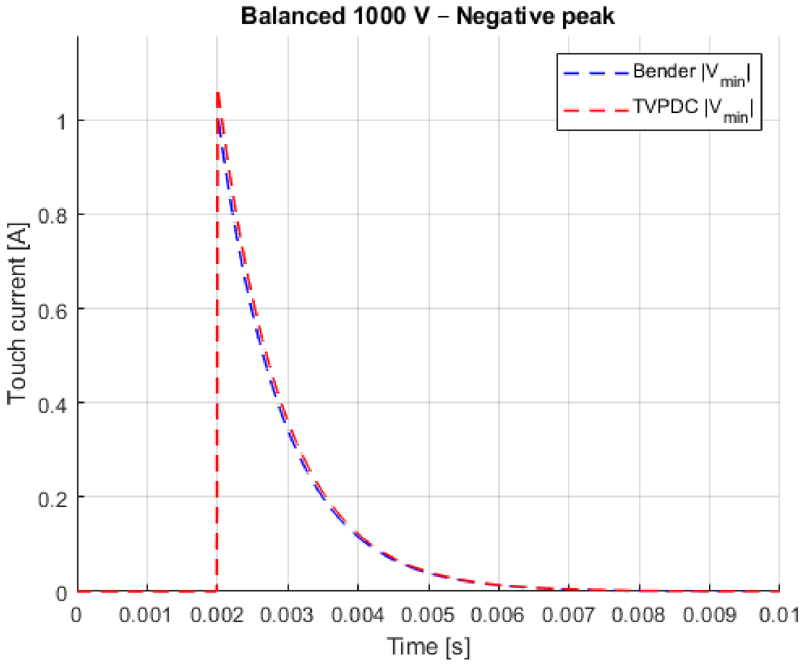

Figure E.6: Balanced 1000V negative peak

Unbalanced cases :

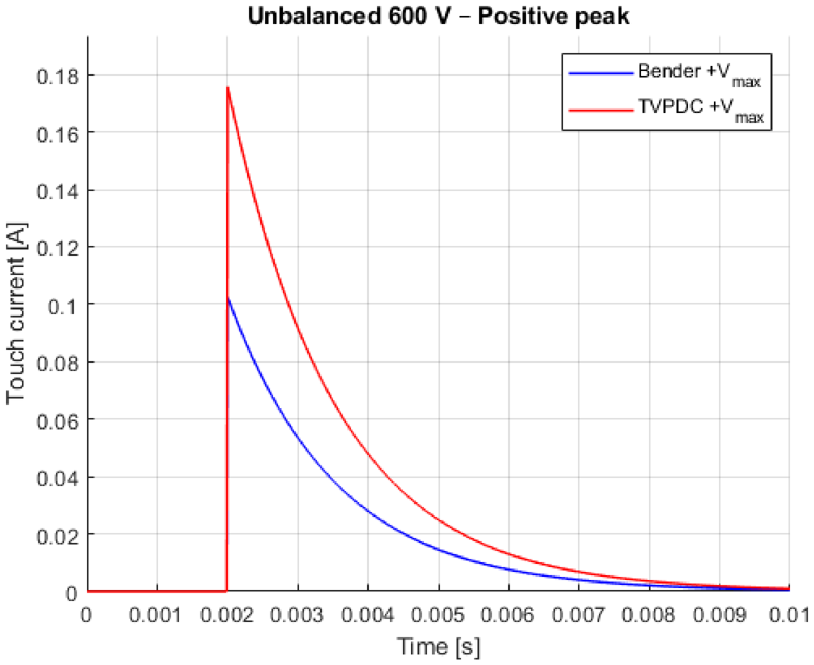

Figure E.7: Unbalanced 600V positive peak

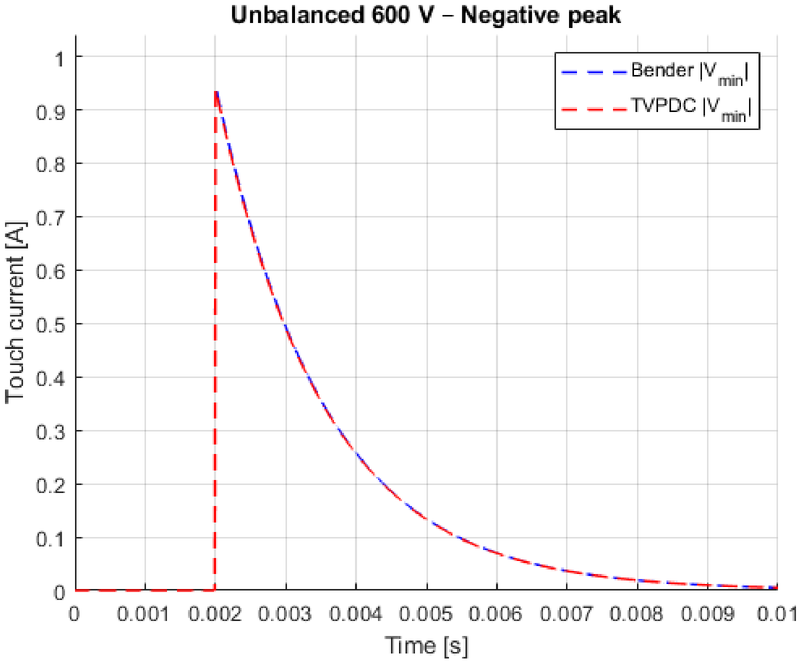

Figure E.8: Unbalanced 600V negative peak

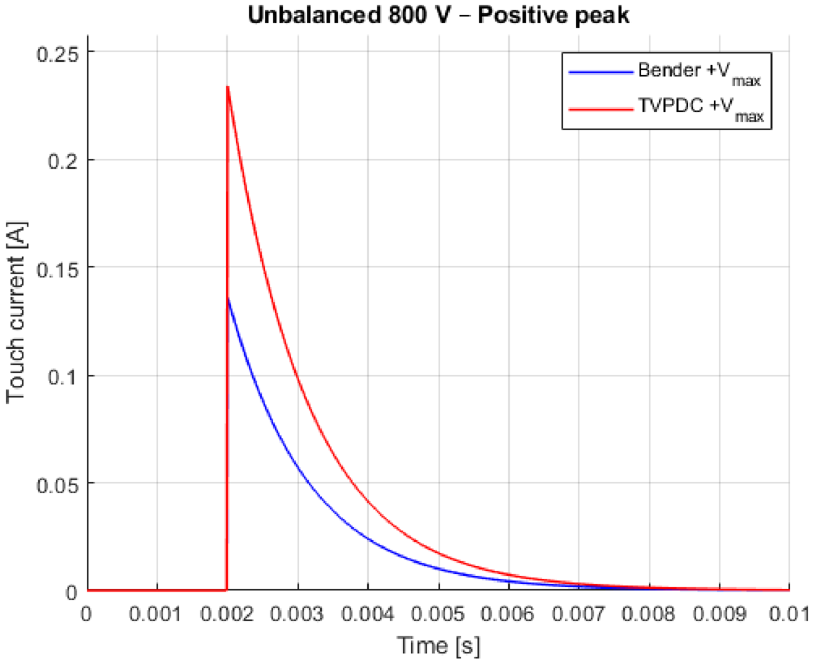

Figure E.9: Unbalanced 800V positive peak

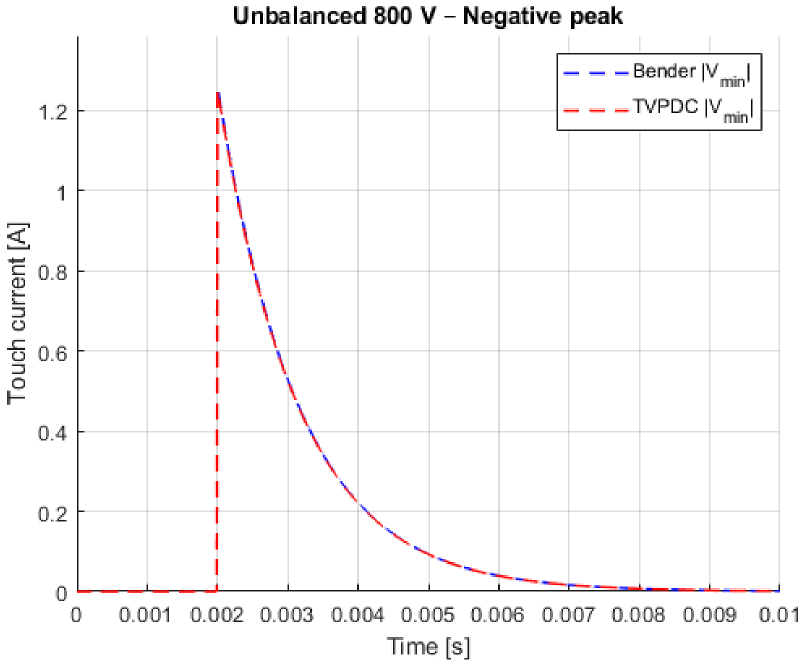

Figure E.10: Unbalanced 800V negative peak

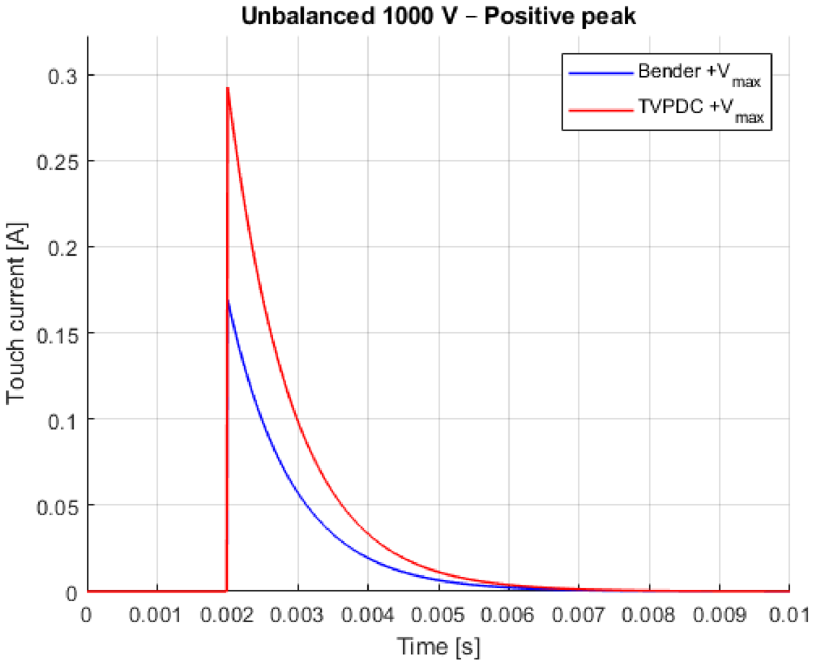

Figure E.11: Unbalanced 1000V positive peak

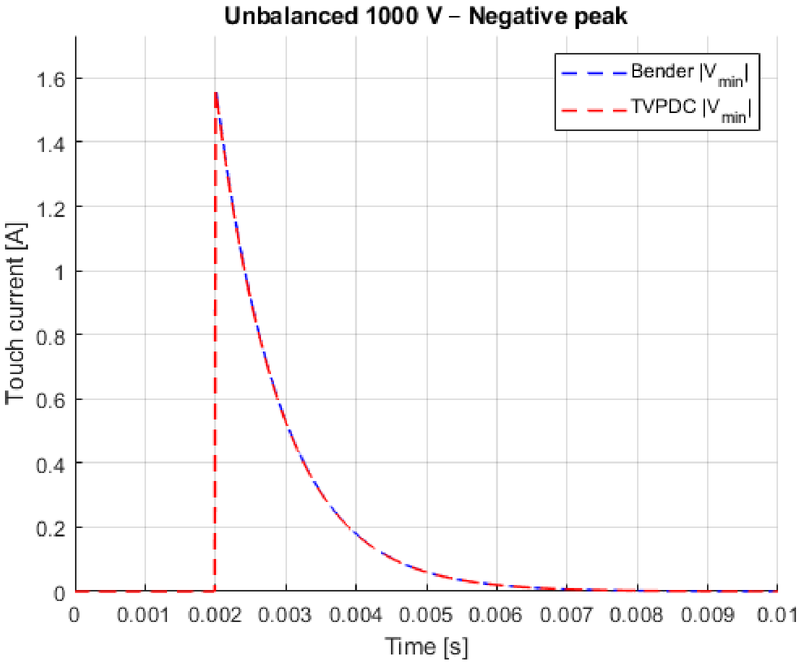

Figure E.12: Unbalanced 1000V negative peak

DEPARTMENT OF SOME SUBJECT OR TECHNOLOGY
CHALMERS UNIVERSITY OF TECHNOLOGY
Gothenburg, Sweden
www.chalmers.se

CHALMERS